Quasi-Phase Matching of Soft X-ray Light from High-Order Harmonic Generation using Waveguide Structures

by

Emily Abbott Gibson

B.S. Engineering Physics, Colorado School of Mines, 1997

A thesis submitted to the

Faculty of the Graduate School of the

University of Colorado in partial fulfillment

of the requirements for the degree of

Doctor of Philosophy

Department of Physics

2004

This thesis entitled:
Quasi-Phase Matching of Soft X-ray Light from High-Order Harmonic Generation using Waveguide Structures
written by Emily Abbott Gibson
has been approved for the Department of Physics

Henry C. Kapteyn

Margaret M. Murnane

Date ____________________

The final copy of this thesis has been examined by the signatories, and we find that both the content and the form meet acceptable presentation standards of scholarly work in the above mentioned discipline.

Gibson, Emily Abbott (Ph.D., Physics)

Quasi-Phase Matching of Soft X-ray Light from High-Order Harmonic Generation using Waveguide Structures

Thesis directed by Profs. Henry C. Kapteyn and Margaret M. Murnane

Ultrafast laser technology has made it possible to achieve extremely high field intensities, above 10^{18} W/cm^2, or alternatively, light pulses with extremely short time durations corresponding to only a few femtoseconds (10^{-15} s). In this high intensity regime, the laser field energy is comparable to the binding energy of an electron to an atom. One result of this highly non-perturbative atom-light interaction is the process of high-order harmonic generation (HHG). In HHG, the strong laser field first ionizes the atom. The subsequent motion of the free electron is controlled by the oscillating laser field, and the electron can reach kinetic energies many times that of the original binding energy to the atom. The high energy electron can then recollide with its parent ion, releasing a high energy photon. This process occurs for many atoms driven coherently by the same laser field, resulting in a coherent, laser-like beam of ultrafast light spanning the ultraviolet to soft X-ray regions of the spectrum.

In this thesis, I will present two major breakthroughs in the field of high harmonic generation. First, I will discuss work on quasi-phase matching of high harmonic generation, which has allowed increased conversion efficiency of high harmonic light up to the water window region of the soft X-ray spectrum ($\sim$ 300 eV) for the first time.[31] This spectral region is significant because at these photon energies, water is transparent while carbon strongly absorbs, making it a useful light source for very high resolution contrast microscopy on biological samples. Since the resolution is on order of the wavelength of the light ($\sim$ 4 nm for 300 eV), detailed structures of cells and DNA can be viewed. A table-top source of light in the water window soft X-ray region would greatly benefit biological and medical research. Second, I will present work on the generation of very high harmonic orders from ions. This work is the first to show that harmonic emission from ions is of comparable efficiency to emission from neutral atoms thereby

showing that high harmonic emission is not limited by the saturation intensity, or the intensity at which the medium is fully ionized, but can extend to much higher photon energies.[30] Both results were obtained by using a waveguide geometry for HHG, allowing manipulation of the phase matching conditions and reducing the detrimental effects of ionization. The ideas from this work are expected to increase the number of applications of high harmonic generation as a light source by increasing the efficiency of the process and opening up the possibility of generating multi-keV photon energies.

Dedication

To my parents.

Acknowledgements

I was fortunate to have had the opportunity do my graduate work in Margaret Murnane and Henry Kapteyn's group which provided a stimulating and supportive environment for doing interesting research. I am very grateful to both Margaret and Henry for their enormous generosity, advice, and for believing I could succeed. I would like to thank the people who contributed to my education and made my graduate experience a good one; in particular, Thomas Weinacht, who taught me about experimental methods and whose enthusiasm was contagious, and Sterling Backus, who taught me a great deal about lasers and ultrafast optics. The work presented here on quasi-phase matching was done with Ariel Paul, who had the ingenuity to make the modulated waveguides. The work on pulse compression was done with Nick Wagner, who always comes up with new physical insights and ideas in the lab. It was a great experience working with both. Also, many others in the group, past and current: Lino Mitsoguti, Erez Gershgoren, Chi-Fong Lei, Randy Bartels, Ra'anan Tobey, David Gaudiosi, Tenio Popmintchev, David Samuels, Xiaoshi Zhang, Etienne Gagnon, and Daisy Raymondson were always happy to lend a hand or give scientific advice. Ivan Christov from Sofia University, Bulgaria did much of the theory for the experiments described here and my discussions with him provided a lot of useful insight.

I am also indebted to the many people on the JILA and Physics Instrument shops staff who freely gave their knowledge and help with these experiments. I would like to thank the professors who not only taught me but also believed in my abilities, especially John Cooper, whose encouragement meant a great deal, and Stephen Leone, who continued to support me long

after I stopped working as an undergraduate in his group. Paul Corkum also showed me great generosity and, even in the brief time I visited his group, influenced my understanding of the field. I would not have made it through the tough times without the support and understanding of my family and without the help of some very good friends in graduate school who were responsible for many of the good times as well, in particular, Tara Fortier and Martin Griebel.

Contents

Chapter

Appendix

Tables

Table

Figures

Figure

Chapter 1

Introduction

Ultrafast laser technology makes it possible to generate extremely high field intensities above 10^{18} W/cm^2, or alternatively, to generate pulses with extremely short time durations corresponding to only a few femtoseconds (10^{-15} s).[8, 14] One of the most prominent applications of very high-power, ultrashort-pulse lasers has been the study of non-perturbative light-matter interactions. At intensities above 10^{14} W/cm^2, the magnitude of the electric field of the laser radiation is comparable to the field binding an electron to an atom. In this regime, the laser field can easily ionize atoms. Once the atom is ionized, the subsequent motion of the free electron is controlled by the oscillating laser field, and the electron can easily reach kinetic energies many times that of the original electron binding energy. One significant consequence of this intense light-matter interaction is the process of high-order harmonic generation (HHG).[51, 28] In HHG, the free electron recollides with its parent ion and recombines with it, releasing a high energy photon. Since all atoms experience the same coherent laser field, the harmonic radiation is also highly coherent. Temporally, high harmonic radiation is a series of attosecond-duration bursts occurring every half-cycle of the driving laser. This unique property has allowed measurements of electronic processes in atoms occurring on timescales previously inaccessible.[40, 24] The emission from HHG can extend from the ultraviolet up to the soft x-ray region of the spectrum (to $\sim$ 950 eV). This spectral region is interesting for studies of chemical and material processes because these photon energies can access valence and inner shell electrons of atoms and molecules.[11, 33, 55] Also, HHG is an extremely useful light source for applications such as plasma interferometry[23, 60] or extreme-ultraviolet (EUV) lithography, a technology that will be needed to implement the next generation of integrated circuits. Thus, high harmonic generation has both fundamental and practical applications. However, one major problem is that the efficiency of HHG is extremely low, typically on order of 10^{-5} to 10^{-10} conversion of laser energy into each harmonic order. As with any harmonic generation process, the efficiency can be greatly enhanced by phase matching. Traditional optical phase matching techniques have been applied successfully to high harmonic generation for low harmonic orders ($<$ 90 eV).[62, 26] However, before now there were no techniques for enhancement of HHG at higher photon energies.

In this thesis, I will present two major breakthroughs in the field of high harmonic generation. First, I will discuss work on quasi-phase matching of high harmonic generation, which has allowed increased conversion efficiency of high harmonic light up to the water window region of the soft X-ray spectrum ($\sim$ 300 eV) for the first time.[31] This spectral region is significant because at these photon energies, water is transparent while carbon strongly absorbs, making it a useful light source for very high resolution contrast microscopy on biological samples. Since the resolution is on order of the wavelength of the light ($\sim$ 4 nm for 300 eV), detailed structures of cells and DNA can be viewed. A table-top source of light in the water window soft X-ray region would greatly benefit biological and medical research. Second, I will present work on the generation of very high harmonic orders from ions. This work is the first to show that harmonic emission from ions is of comparable efficiency to emission from neutral atoms thereby showing that high harmonic emission is not limited by the saturation intensity, or the intensity at which the medium is fully ionized, but can extend to much higher photon energies.[30] Both results were obtained by using a waveguide geometry for HHG, allowing manipulation of the phase matching conditions and reducing the detrimental effects of ionization. The ideas from this work are expected to increase the number of applications of high harmonic generation as a light source by increasing the efficiency of the process and opening up the possibility of generating multi-keV photon energies.

1.1 High-order Harmonic Generation

High-order harmonic generation occurs when an intense linearly polarized laser field interacts with a gas or material. An intuitive model of HHG at the atomic level was developed by Corkum, Kulander, and others,[22, 44] and is sometimes referred to as the three-step model. In the first step, the strong electric field of the laser suppresses the Coulomb barrier binding an electron to an atom, freeing the valence electron either by tunnelling or by over-the-barrier ionization. The freed electron is then accelerated by the field. Since the laser field is oscillating, the electron can with some probability return to its parent ion and recombine, emitting a high-energy photon. This process occurs for many atoms driven coherently over several laser cycles, resulting in emission of higher-order odd harmonics of the fundamental in a coherent, low-divergence beam. The three-step model accurately predicts that the highest photon energy that can result from HHG occurs when an electron is ionized at a phase corresponding to 18 degrees after the peak of the laser cycle. This cutoff photon energy is predicted to be:

$$E_{max} = I_p + 3.2U_p, \tag{1.1}$$

where I_p is the ionization potential of the atom and U_p is the ponderomotive energy given by:

$$U_p = e^2E^2/4m\omega^2 = 9.33 \times 10^{-14} I\lambda^2 eV, \tag{1.2}$$

where e, E, m, ω, I, and λ are the electron charge, field amplitude, electron mass, fundamental laser frequency, intensity in W/cm^2, and wavelength in microns respectively. The highest photon energy therefore scales linearly with the laser intensity.

The recollision energies associated with the intensities required to field-ionize atoms can be as high as hundreds of electron volts.[15, 70, 67] Thus, the emitted high-harmonic photons can correspond to the combined energy of several hundred incident photons. The linear relationship between the cutoff and the incident intensity presents a very attractive scaling as compared to, for example, EUV laser schemes where the power requirements scale as the photon energy to the 3rd-5th power.[39] However, to take advantage of this favorable scaling, several challenges must be overcome. The HHG process necessarily ionizes the medium, generating a free-electron plasma. The dispersion of the plasma creates a mismatch in the phase velocities of the fundamental and harmonic light, significantly reducing the amount of harmonic signal produced. Also, the generated plasma can defocus the laser beam, decreasing the peak intensity and thereby limiting the maximum harmonic energy.[48] To date, the highest energy HHG emission has been achieved using short-duration laser pulses and noble gases with high ionization potentials such as helium, which can reduce the amount of ionization for a given peak intensity. However, helium has a small cross-section giving it a lower efficiency for HHG than larger, multi-electron atoms. In Ch. 3, I will discuss a method of generating high harmonics even in a fully ionized gas medium, allowing HHG in argon up to photon energies of 250 eV, previously achieved only with He gas, and demonstrating that HHG from ions is feasible. In combination with quasi-phase matching techniques, this method should extend the efficient energy range of HHG even further.

The simple semi-classical picture of HHG as given by the three-step model accurately predicts the range of photon energies that can be obtained for a given incident laser intensity. However, a quantum mechanical treatment is needed for a more complete picture of the HHG process. In the quantum picture, as the laser field strength increases, portions of the electron wave function tunnel through the suppressed atomic barrier and then propagate large distances - relative to the atomic radius - away from the atom. When the laser field reverses, this extended electron wavefunction re-encounters the part of the wavefunction still in the ground state of the atom, leading to quantum interferences. As a result, rapid oscillations in the electronic probability distribution and therefore the transient dipole moment of the atom lead to the emission of very high-order harmonics of the fundamental laser.

A fully quantum, analytical theory of HHG, derived by Lewenstein et al.[46], has been extremely successful in describing both the general characteristics of HHG such as the photon energy cutoff, as well as more specific characteristics such as the divergence properties of the generated beam[9] and the specific spectral characteristics of the emission. Qualitatively, the spectral characteristics of HHG emission are a result of the fact that the freed electron has an associated deBroglie wavelength corresponding to the kinetic energy acquired in the laser field, $\lambda = h/p$, where h is Planck's constant and p is the electron momentum. The emission also has a phase related to the total phase the electron accumulates during its free trajectory, given by:[9]

$$\Phi = q\omega t_f - S(p_{st}, t_i, t_f)/\hbar, \tag{1.3}$$

where q is the harmonic order, ω is the laser frequency, t_i is the time the electron is released in the laser field, t_f is the recollision time, and $S(p_{st}, t_i, t_f)$ is the semi-classical action over the electron's trajectory. The phase of the emitted harmonic light is therefore not simply related to the phase of the driving laser, but also includes an intrinsic phase component that can vary rapidly with laser intensity. The intrinsic phase has consequences for both the spatial and spectral emission characteristics. Spatially, the intrinsic phase can result in a complex spatial profile of the harmonic emission when generated using a beam that is converging toward a focus. This is in contrast to the gaussian spatial profile for HHG generated by a beam diverging from a focus[9, 63, 58] or the full spatial coherence of light generated using a waveguide configuration.[49] In the spectral domain, this time-varying intrinsic phase results in large frequency shifts and spectral broadening or narrowing of the harmonic emission.[16] The intrinsic phase also plays a role in quasi-phase matching of HHG as will be discussed in the next chapter.

Chapter 2

Quasi-Phase Matching

Applications of HHG radiation as a table-top, coherent soft X-ray source depend upon optimizing the total flux generated. In nonlinear optical processes, the conversion efficiency from the fundamental to the harmonic field is enhanced by phase matching. In its simplest manifestation, phase matching will occur when the driving laser and the harmonic signal travel with the same phase velocity, so that signal generated throughout the conversion region adds constructively. In HHG, since the ionization level is changing throughout the pulse, and the increasing density of free electrons has a large effect on the phase velocity of the driving laser, phase matching can only be obtained in limited time windows in the pulse. Experimentally, dramatic enhancement of the flux from HHG can be achieved by pressure-tuned phase matching using hollow-core gas-filled waveguides.[62, 26] The laser light is guided by glancing-incidence reflection off the waveguide walls, allowing propagation over an extended interaction length with a well defined intensity and phase profile. The fundamental and harmonic light propagate through the waveguide with phase velocities determined by the dispersion of the neutral gas, the plasma, and the waveguide at the two different frequencies. The phase mismatch is given by $\Delta k = qk_f - k_q$, where k_f is the wavevector of the fundamental and k_q is the wavevector of harmonic order q. The full expression is given by:

$$\Delta k = \Delta k_{Waveguide} + \Delta k_{Plasma} + \Delta k_{Neutrals} \tag{2.1}$$

or

$$\Delta k = \frac{q u_{11}^2 \lambda}{4\pi a^2} + P\eta N_{atm} r_e (q\lambda - \lambda/q) - \frac{2\pi(1-\eta)Pq\Delta\delta}{\lambda}, \tag{2.2}$$

where λ, q, a, u_{11}, η, P, N_{atm}, and r_e are the fundamental wavelength, harmonic order, waveguide radius, the first zero of the Bessel function J_0, ionization fraction, gas pressure in atmospheres, number density at 1 atm, and classical electron radius respectively, and $\Delta\delta$ is the difference in the index of refraction at the fundamental and harmonic frequencies of the generation gas at 1 atm. Here, the small contribution from the nonlinear refractive index is neglected and it is assumed that the harmonic light does not interact with the waveguide. The waveguide allows control over the experimental parameters such as gas pressure and radius to optimize phase matching.

For low levels of ionization, the pressure can be adjusted so that the waveguide and plasma dispersion balance the dispersion due to the neutral atoms, which is of opposite sign, and phase matching can be achieved ($\Delta k = 0$). Since phase matching is accomplished by adjusting the phase velocity of the fundamental, and the harmonic radiation travels at a phase velocity of ~c, the bandwidth of phase matching is very broad, encompassing many harmonic orders. At higher laser intensities, the rapidly-changing ionization during the pulse means that there is a limited time-window for phase matching. However, the phase matching bandwidth is also broad since the phase matching condition for different harmonic orders will occur at some time during the pulse. When phase matched, the harmonic signal increases quadratically with interaction length until it is limited by absorption of the harmonic light by the gas medium.

Unfortunately, this method of phase matching is limited to low ionization levels. When a large enough fraction of the gas is ionized, the plasma dispersion is greater than the neutral dispersion for any pressure so that phase matching is no longer possible. The phase velocity of the fundamental light then exceeds that of the generated harmonic signal. The value of this critical ionization fraction is given by:[61]

$$\eta_{cr} = (1 + \frac{N_{atm} r_e \lambda^2}{2\pi\Delta\delta})^{-1}. \tag{2.3}$$

Figure 2.1 plots the pressure required to achieve phase matching as a function of the ionization fraction. For low laser intensities, and therefore lower harmonic orders, where the ionization fraction is small, phase matching is primarily achieved by balancing the waveguide dispersion with the neutral gas dispersion. At the higher laser intensities required to generate higher energy harmonics, however, the plasma term becomes significant, and higher neutral gas pressures are needed to compensate. Beyond the critical ionization, phase matching is not possible.[25, 21] For the case of plane wave propagation without a waveguide in a uniform-density gas, phase matching will occur when the fractional ionization equals the critical ionization.[61] However, this requires either very high pulse energies or high gas pressure and results in spatially varying phase matching which can create a complex spatial mode of the harmonic emission. In contrast, the use of the hollow waveguide allows for better phase matching, resulting in buildup of an EUV beam with a spatial mode of extremely high coherence.[10, 49] In fact, EUV light from HHG with full spatial coherence has currently only been generated using a hollow waveguide geometry.

Despite the many advantages of phase matching HHG in a straight waveguide, it is limited to relatively low levels of ionization, below the critical ionization fraction (0.5%, 1% and 5% in He, Ne and Ar). This limitation restricts the enhancement of HHG emission to photon energies < 100 eV for a 20 fs pulse since higher energy harmonics can only be generated at higher laser intensities and therefore greater ionization fractions. At higher ionization levels, the plasma contribution to the dispersion becomes much greater than the neutral gas contribution, making phase matching impossible. In the absence of phase matching, the harmonic emission builds up periodically over a coherence length and then interferes with out-of-phase light generated in the next section of the nonlinear medium, drastically reducing the total flux.

2.1 Introduction to Quasi-Phase Matching

In recent work, we showed that the inability to phase match for relatively small amounts of ionization can be overcome for the first time by applying quasi-phase matching (QPM) tech-

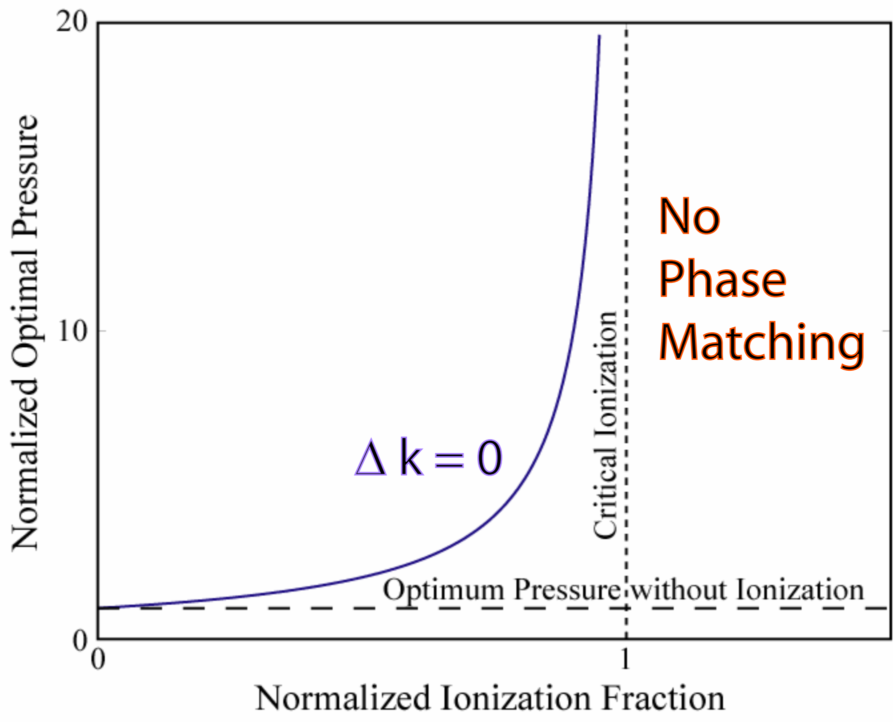

Figure 2.1: Plot of pressure for phase matching as a function of normalized ionization fraction (η/η_{cr}). Beyond critical ionization, phase matching is no longer possible.

niques to the HHG process. The ability to quasi-phase match HHG significantly extends the range of photon energies where it is possible to generate high-harmonic emission efficiently. Quasi-phase matching was first proposed in 1962, shortly after the birth of nonlinear optics. Armstrong et al.[4] proposed a phase corrective scheme whereby the phase mismatch in a nonlinear optical process is periodically corrected by introducing a periodicity to the nonlinearity of the medium corresponding to the coherence length. The coherence length is defined as the distance it takes for the fundamental and harmonic light to become 180 degrees out of phase. For example, quasi-phase matching of second harmonic light can be achieved by periodically reversing the crystal orientation and therefore the polarity of the nonlinear response so that a 180 degree phase shift is introduced every coherence length. This reverses the destructive interference, allowing continual buildup of the harmonic signal, shown in Fig. 2.2. Practical implementation of this concept was not achieved until the development of crystal-poling techniques in the mid-1990's.[27]

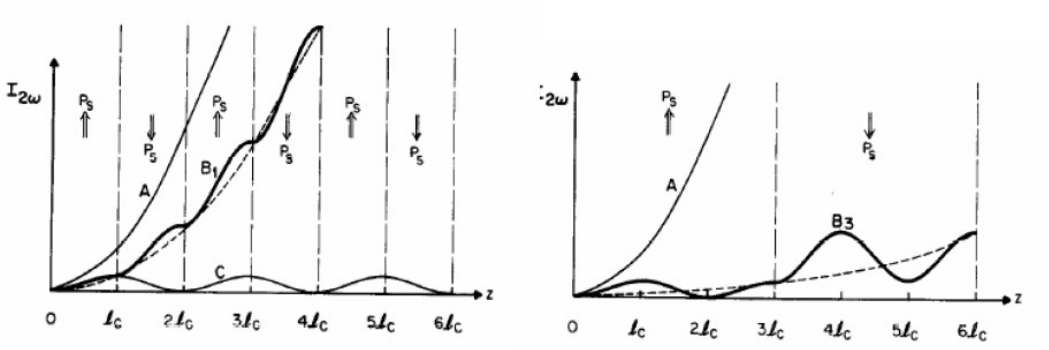

Figure 2.2: Diagram of quasi-phase matching plotting the second harmonic signal for the conditions of: A. Perfect phase matching, C. No phase matching, B1. First-order QPM, and B3. Third-order QPM. From [27].

Unfortunately, the generation of coherent light at EUV and soft X-ray wavelengths must take place in a gas or on a surface, making the use of standard QPM techniques impossible. However, the extreme nonlinear nature of HHG makes alternate approaches possible. For example, quasi-phase matching of the frequency conversion process can be achieved by restricting

HHG to regions where the signal will be in phase and add constructively. Previous theoretical ideas for quasi-phase matching of HHG include using a modulated density gas or plasma to periodically change the nonlinear susceptibility.[69] Another proposal suggested using counter-propagating light to modulate the intensity and phase of the driving laser.[77] Experimentally, quasi-phase matching of HHG was first implemented using a technique proposed by Christov et al.[19] In this technique, high harmonics are generated in a hollow-core waveguide which has a periodically changing inner diameter along the length of the guide to modulate the driving laser intensity. The modulation of the laser intensity effectively turns on and off the generation of harmonics near the cutoff. Figure 2.3.a shows a calculation of the signal of the 95^{th} harmonic, in the cutoff, as a function of propagation length in a straight waveguide using a 15 fs pulse with a peak intensity of 7 x 10^{14} W/cm^2 and 1 Torr of argon. The calculation uses a three-dimensional propagation model and the harmonic signal is calculated using a quasi-classical approximation for the dipole moment. The oscillations of the harmonic signal are a result of the phase mismatch as signal builds up over a coherence length and then interferes with out-of-phase light in the next coherence length. Figure 2.3.b shows the same calculation using a hollow-core waveguide with a 0.5 mm period sinusoidal corrugation that changes the laser intensity on-axis by 5%. The modulated waveguide causes a dramatic enhancement in the final signal (note the different scales of the two plots).

We can understand the basic physics behind the enhancement of the HHG signal using classical nonlinear optics theory. In a simplified model of harmonic generation, the field of harmonic order q, after propagating a distance L in a nonlinear medium, is related to the phase mismatch, Δk, by:

$$E_q \propto \int_0^L E_\omega^n d(z) e^{-i\Delta k z} dz, \tag{2.4}$$

where E_ω is the fundamental field, n is the effective order of the nonlinear process, d(z) is the nonlinear coefficient, and Δk is the phase mismatch calculated in equation 4. To model quasi-phase matching, the nonlinear coefficient is expressed as a general periodic function of z with

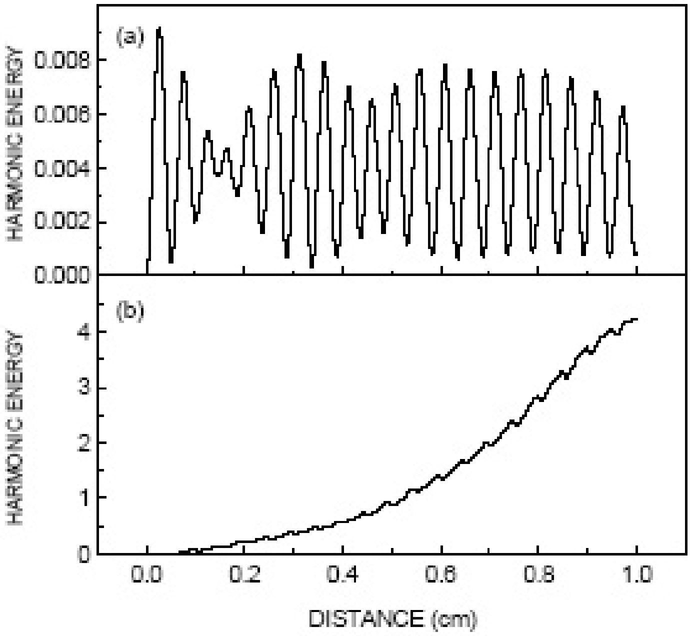

Figure 2.3: a. Calculation of the signal of the 95^{th} harmonic for a straight waveguide as a function of propagation distance. b. Calculation for a 0.5 mm period modulated waveguide. From [19].

period Λ:[27]

$$d(z) = d_{eff} \sum_{m=-\infty}^{\infty} G_m e^{iK_m z}, \tag{2.5}$$

where $K_m = 2\pi m/\Lambda$ is the effective wavevector of QPM and m is the order of the QPM process. Combining Eqns. 2.4 and 2.5 shows that the harmonic signal will be enhanced when $K_m \approx \Delta k$. The enhancement in signal will be greatest for m = 1, but the signal will also be enhanced for higher order QPM (i.e. m = 3,5,...). The new quasi-phase matching condition for HHG is therefore given by:

$$\Delta k = \Delta k_{Waveguide} + \Delta k_{Plasma} + \Delta k_{Neutrals} - K_m \tag{2.6}$$

or

$$\Delta k = \frac{q u_{11}^2 \lambda}{4\pi a^2} + P\eta N_{atm} r_e (q\lambda - \lambda/q) - \frac{2\pi(1-\eta)Pq\Delta\delta}{\lambda} - 2\pi m/\Lambda. \tag{2.7}$$

From Eqn. 2.7, it is evident that a larger value of K_m, i.e. a shorter modulation period, can compensate for a larger Δk, and therefore a higher level of ionization.

2.2 Experimental Results on Quasi-Phase Matching of High Harmonic Generation

The first set of experiments demonstrating quasi-phase matching of HHG showed a dramatic extension of the harmonic spectrum using modulated waveguides.[56] In this experiment, 25 fs duration pulses from a high repetition rate (2-5 kHz, 1 mJ/pulse) Ti:sapphire laser system operating at 760 nm[7] were focused into 150 μm diameter modulated hollow-core waveguides with different periodicities filled with helium gas. The modulated waveguides used in this experiment were produced using precision glass-blowing techniques starting with straight hollow-core glass fibers, 150 μm in diameter. The modulations were approximately sinusoidal, with a radial depth on the order of 10 microns, corresponding to a 13% modulation of the fiber radius. Figure 2.4 shows a picture taken with an optical microscope of a modulated waveguide with a 0.25 mm periodicity. The initial experiments used waveguides with modulation periods varying from 1-0.5 mm. Figure 2.5 shows the experimentally measured HHG spectra from He for three different modulated-waveguide periodicities. As the modulation period is reduced from 1 mm to 0.75 mm to 0.5 mm, the highest observable harmonic energy increases from 112 eV to 175 eV and the signal is enhanced at higher and higher photon energies. This behavior agrees well with the predictions from the simple QPM model that shorter modulation periods can compensate for more ionization and thus phase match higher photon energies.

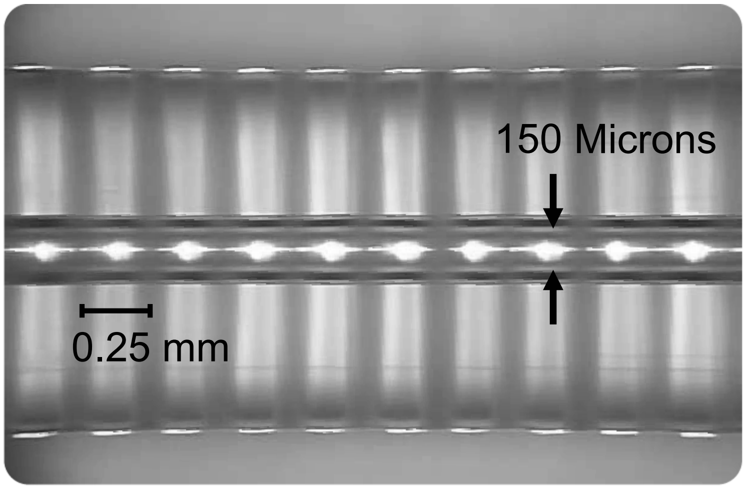

Figure 2.4: Optical microscope image of a 0.25 mm period modulated waveguide manufactured by glass-blowing techniques. From [31].

The significance of QPM is that it enhances the higher energy harmonics that are generated at greater ionization levels, closer to the peak of the pulse. This effect becomes apparent from a calculation of the coherence length that results from the mismatch in the phase velocity of the fundamental and harmonic due to ionization. At high ionization levels, the phase mismatch is predominantly due to the plasma dispersion and the waveguide dispersion and is given by:

$$\Delta k \approx P\eta N_{atm} r_e q\lambda + \frac{q u_{11}^2 \lambda}{4\pi a^2}, \tag{2.8}$$

where the assumption $q\lambda >> \lambda/q$ is made. For example, using the same conditions as in the

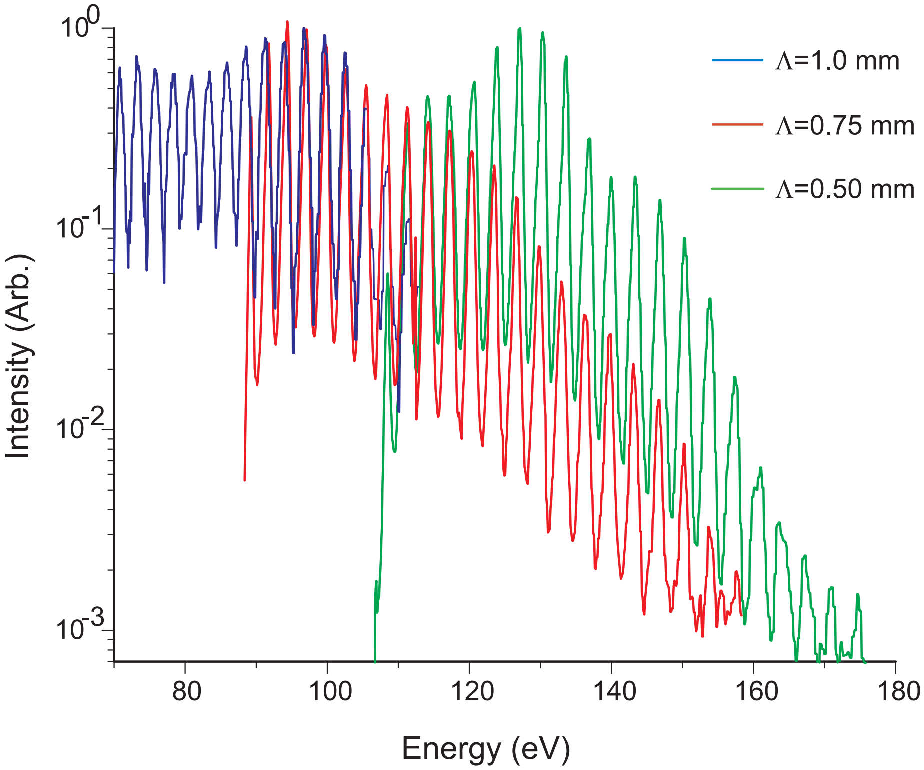

Figure 2.5: Experimental harmonic spectra from modulated waveguides filled with 111 Torr He with a driving pulse of 25 fs and peak intensity ~ 5 x 10^{14} W/cm^2, for different modulation periodicities. From [56].

theory paper of Christov et al.,[19] fully ionized argon at a pressure of 1 Torr gives an electron density of $n_e = 3.5$ x 10^{16} cm^{-3}. From equation 2.8, the phase mismatch of the 95th harmonic order (150 eV) is calculated to be $\Delta k_{plasma} \sim 7550$ m^{-1} and $\Delta k_{waveguide} \sim 6200$ m^{-1}, giving a total $\Delta k \sim$ 13,750 m^{-1}. The phase mismatch is close to the value of the effective QPM wavevector for a modulation period of 0.5 mm of $K_1 \sim$ 12,600 m^{-1}. Thus, very substantial levels of ionization can be compensated for by using waveguides with modulation periods in the range of 1 - 0.25 mm that can be readily manufactured with glass-blowing techniques.

In the initial experiments, the ionization levels in He were still relatively low. However, in more recent experiments, we have demonstrated QPM in much higher ionization levels of $>$ 100%. These experiments were performed using a two stage amplifier system (described in Ch.4) with an output pulse energy of 1.2 mJ and a 22 fs pulse duration. Due to loss from mirror reflections on the way to the waveguide setup, around 1.1 mJ pulse energy was focused into the waveguide. The coupling efficiency was $\sim$ 60% for the straight, 0.5 mm, and 0.25 mm modulated waveguides. The fundamental 800 nm light was blocked using a 0.4 μm-thick Zr filter with 25 nm of Ag coated on the front to prevent laser damage. Figure 2.6 shows harmonic spectra from straight and modulated waveguides filled with neon gas. The same gas pressure of 6 Torr was used in the different waveguides for comparison. The decrease in harmonic signal going to lower photon energies is due to the decreasing transmission of the zirconium filter. As expected, the modulated waveguides enhance the highest harmonic orders, and the signal from the 0.25 mm modulated waveguide is about 8 times greater than from the 0.5 mm waveguide, showing the ability of the shorter modulation periods to better compensate for the phase mismatch from ionization. The higher harmonics observed from the 0.5 mm modulated fiber could be due to a slightly better coupling efficiency. The estimated laser intensity in the waveguide is 9 x 10^{14} W/cm^2, producing $\sim$ 24% ionization in neon at the peak of the pulse. Figure 2.7 shows the harmonic spectra from straight and 0.25 mm modulated waveguides filled with 7 Torr Ar. Here, the laser intensity is above the saturation intensity of argon so that the gas is fully ionized with some double ionization, as verified using Ammosov-Delone-Krainov (ADK) tunnelling ionization rates.[3] Even with above 100% ionization, the modulated fiber does enhance the signal by a factor of 2-3 over the entire measured spectral region. For the 109th harmonic order (170 eV), we calculate a phase mismatch of $\Delta k \sim 80{,}000\ \mathrm{m}^{-1}$, therefore this signal could be enhanced by m = 3 QPM. Where the enhancement is greatest at 110 eV (71st harmonic), $\Delta k \sim 20{,}000\ \mathrm{m}^{-1}$, indicating a first order QPM process. Figure 2.8 shows harmonics from straight and modulated waveguides filled with Ar taken on a different day. Here, the enhancement from QPM is even more dramatic.

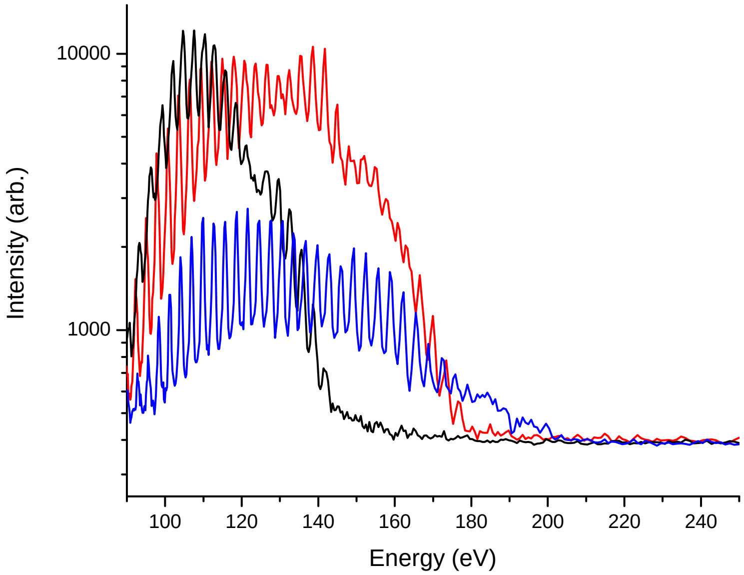

Figure 2.6: Harmonic spectra from straight (black), 0.5 mm (blue), and 0.25 mm (red) periodicity modulated waveguides filled with 6 Torr neon. The spectra were taken using the SC grating and a 10 second exposure time.

The gas pressure in the waveguide is an important parameter in these experiments. Figure 2.9 shows harmonic spectra from the three different waveguides at different neon pressures. Typically, lower gas pressures increase the highest observed harmonic orders. This effect could be a result of reduced plasma defocusing or absorption, both of which can reduce the intensity of the driving laser. Fig. 2.9 also plots the flux for three different photon energy ranges as a function of pressure for the different waveguides. From these plots, it is apparent that there

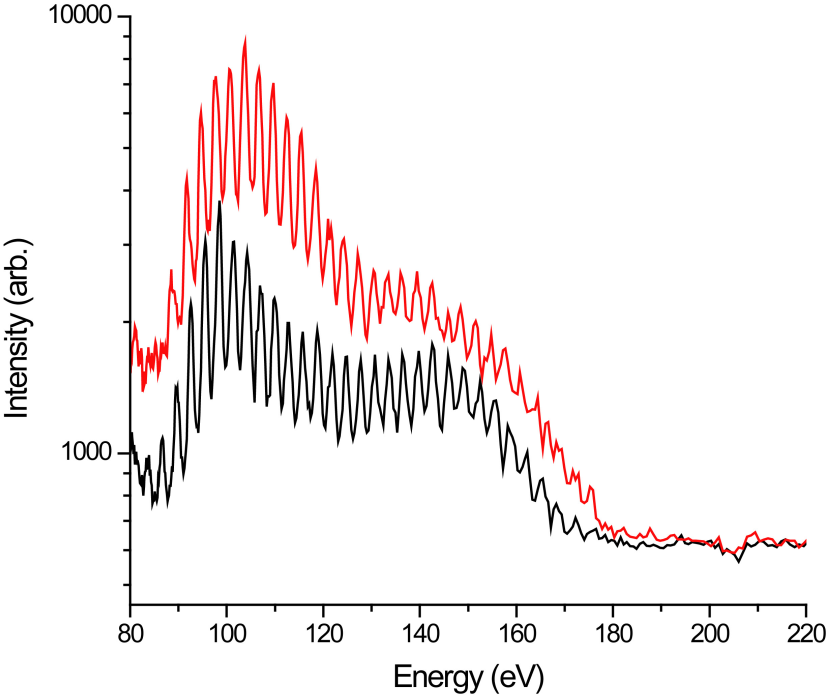

Figure 2.7: Harmonic emission from straight (black) and 0.25 mm (red) modulated waveguides filled with 7 Torr Ar. From [31]. The spectra were taken using the SC grating. The exposure time for the straight waveguide was 300 seconds while for the modulated it was 200 seconds. The spectrum for the modulated waveguide has been multiplied by 1.5 for comparison.

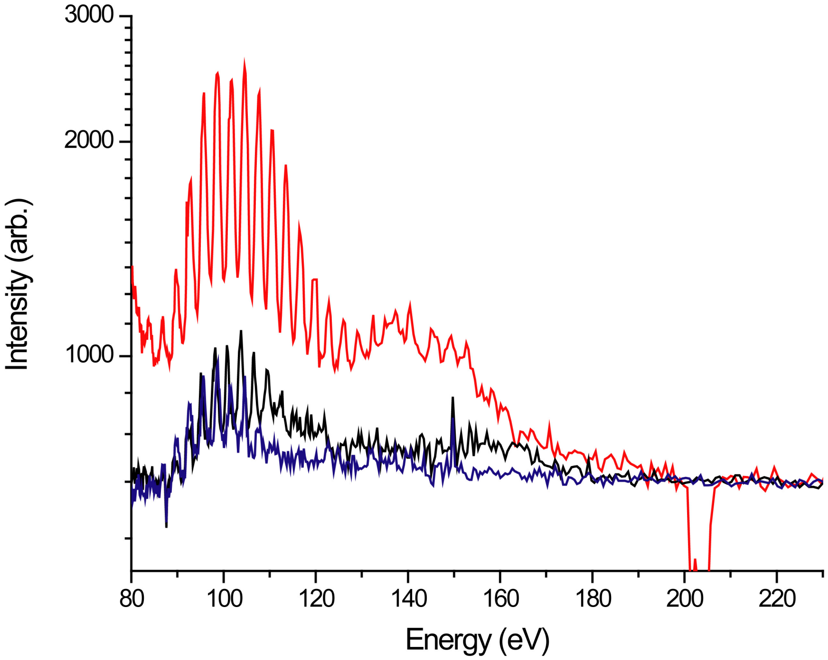

Figure 2.8: Harmonic spectra from a straight waveguide filled with 10 Torr Ar (blue) and 6 Torr Ar (black), and a 0.25 mm modulated waveguide with 5 Torr Ar(red). All spectra were taken with the SC grating. Both straight waveguide spectra have a 300 s exposure time while the modulated waveguide spectrum was taken with 600 s exposure and divided by 2 for comparison.

is phase matching of higher photon energies in the modulated waveguides while in the straight waveguide, phase matching is only achieved for the lower energies.

The next series of experiments were done at a higher laser intensity of 1.6 x 10^{15} W/cm^2, accomplished by using two pump lasers on the second stage of the amplifier giving ~3 mJ of pulse energy at the output. The fundamental light was blocked with Ag filters of 0.45 μm total thickness. Figure 2.10 shows the harmonic emission from 0.25 mm-modulated and straight waveguides filled with 9 Torr Ne. At these intensities, a simple calculation of the cutoff harmonic energy, using Eqn. 1.1, yields an expected cutoff of 330 eV. However, the observable harmonic emission from the straight waveguide (Fig. 2.10 (black curve)) only extends to around 225 eV. In contrast, the harmonic emission from the 0.25 mm modulated waveguide (red curve) is brighter and extends to significantly higher energies, where the carbon edge at 284 eV is clearly visible. Figure 2.11 shows the harmonic spectra when using helium gas. The modulated waveguide enhances the harmonic signal over the entire measured spectrum by at least an order of magnitude, and extends the observable harmonics to 284 eV.

To estimate the amount of phase mismatch in these experiments, the amount of ionization during the time-window in the pulse that a particular harmonic is generated is calculated using ADK (Ammosov-Delone-Krainov) tunnelling ionization rates.[3][See Appendix *A* for details on the calculations] Figure 2.12 shows the fractional ionization of neon and helium as a function of time during the driving pulse for our experimental conditions (pulse duration of 22 fs, peak intensity of 1.6 x 10^{15} W/cm^2). The amount of ionization at the threshold intensity necessary to generate 285 eV harmonics is $\sim$ 50% in neon and $\sim$ 10% in helium, while at the peak of the pulse it is $\sim$ 90% and $\sim$ 37%. The increasing amount of ionization leads to an increasing phase mismatch and therefore the dramatic decrease in the flux observed going to higher harmonic energies. Using the expression in Eq. 2.8, which is valid at high ionization levels, the phase mismatch for the 183^{rd} harmonic order at the C edge (284 eV) in Ne is calculated to be $\Delta k \sim$ 77,000 m^{-1}, assuming 50 % ionization. The effective wavevector for first-order QPM for a modulation period of 0.25 mm is $K_1 \sim$ 25,000 m^{-1}. Again, the harmonic signal will be enhanced

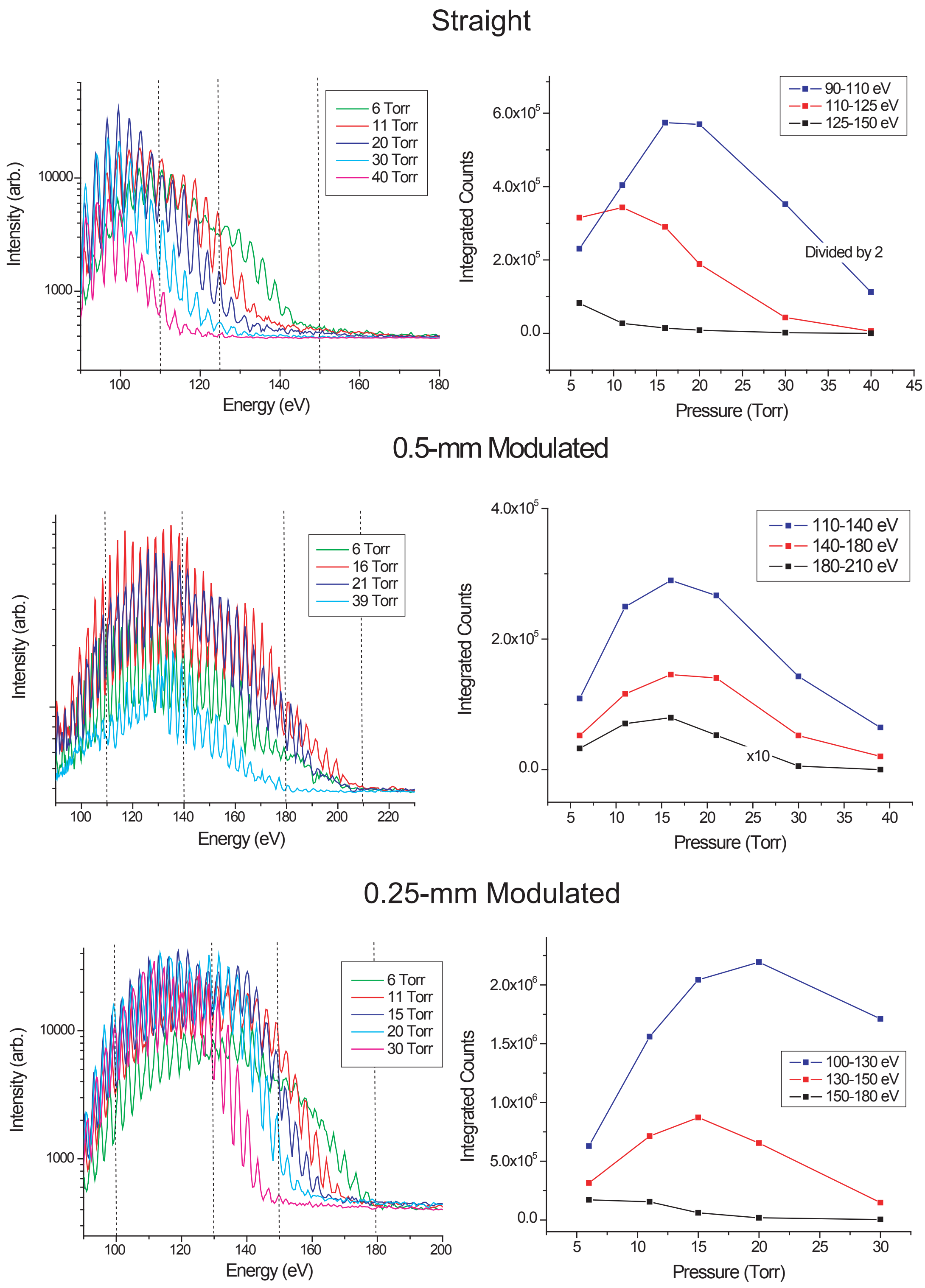

Figure 2.9: Harmonic spectra from straight, 0.5 mm, and 0.25 mm modulated waveguides, with different pressures of neon gas. All spectra were taken with a 10 s exposure time on the SC grating. Also plotted are the integrated counts for three different photon energy ranges as a function of pressure. The energy ranges are indicated with dashed lines.

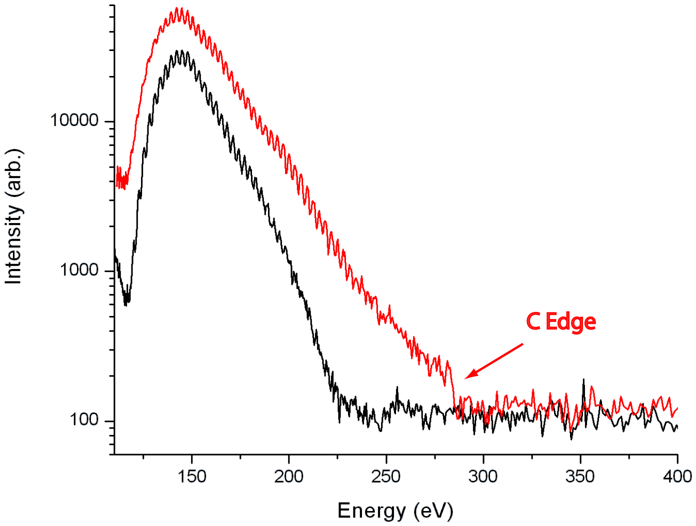

Figure 2.10: Experimental harmonic spectra generated in 9 Torr of neon gas for straight (black) and 0.25 mm modulated (red) waveguides. Both spectra taken with a 180 s exposure time on the SB grating. From [31].

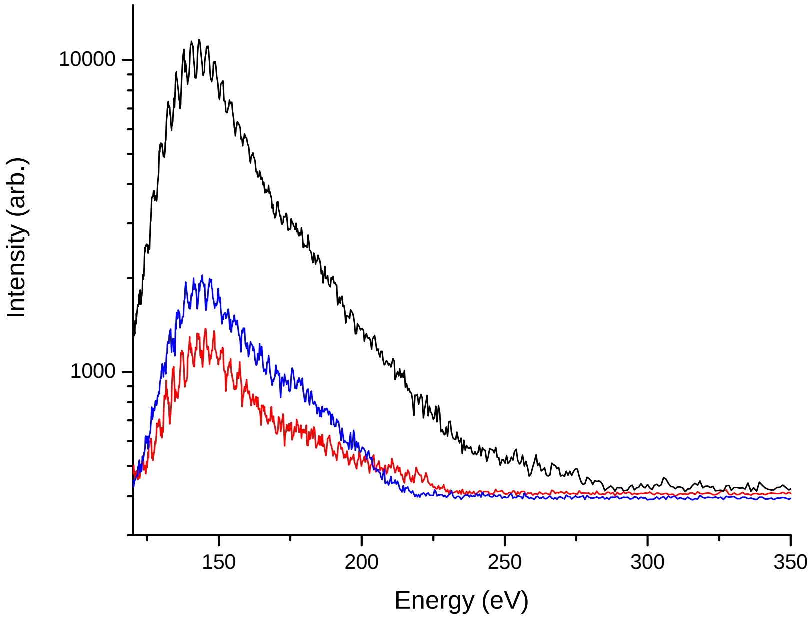

Figure 2.11: Experimental harmonic spectra generated in helium at 15 Torr using a 0.25 mm modulated waveguide (black), and at 16 Torr (blue) and 10 Torr (red) using a straight waveguide. All spectra taken with 120 s exposure on SB grating.

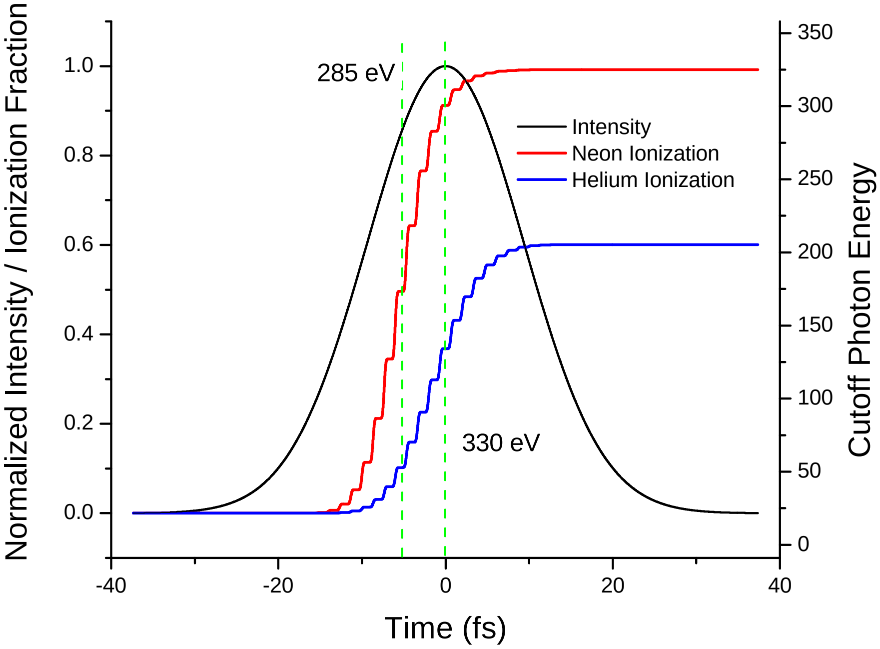

Figure 2.12: Calculation of the fractional ionization of neon and helium as a function of time during the laser pulse. The right axis plots the cutoff photon energy corresponding to the instantaneous pulse intensity.

by QPM when $K_m \approx \Delta k$. The greatest enhancement is for m=1 QPM, but there will still be enhancement of the HHG signal for higher values of m. Thus, for the harmonics in Ne near the C edge, it is possible to compensate for the large phase mismatch of $\sim$ 77,000 m^{-1} by third order (m=3) QPM. For the harmonics above 225 eV, the phase mismatch is large enough that the signal can only be observed using a modulated waveguide and is below the noise level for a straight waveguide. For helium, $\Delta k \sim$ 34,000 m^{-1} for the 183rd harmonic order at the C edge, closer to first order QPM. The spectra shown in figures 2.10 and 2.11 illustrate that the highest observed harmonic orders are not limited by the $I_p + 3.17U_p$ relation, but by ionization-induced phase mismatch. The modulated waveguide compensates for this phase mismatch, making it possible to observe higher harmonics. Although past work observed HHG from He in the water window, this process was not phase matched and produced significantly lower signal levels.[15, 70]

Figure 2.13 compares harmonic spectra at the carbon edge using helium and neon as the generation gas. All spectra were with the same experimental conditions (i.e. driving pulse parameters and exposure time). The signal at the C edge for 9 Torr Ne is about 75% of the intensity for 60 Torr He. For the case of helium, the phase mismatch is around Δk ~100,000 m^{-1}. However, even though the phase mismatch is greater, the atom density is higher by a factor of 7, which can explain the higher flux. Further comparison between helium and neon is shown by the spectra in Fig.2.14, showing both at similar pressure. The phase mismatch at the C edge for 15 Torr He is $\Delta k \sim$ 34,000 m^{-1} compared to $\Delta k \sim$ 70,000 m^{-1} for 8 Torr of Ne. Therefore the higher signal for He compared with Ne is due to the lower order of the QPM process.

Based on conservative estimates of detection efficiency and filter transmission, and measurements of grating efficiency, a minimum flux of between $10^6 - 10^8$ photons/sec in a 10% bandwidth at the C edge was calculated. Details of the calculation are given in Ch.4. This flux may be sufficient for biological imaging applications and a number of improvements, such as shorter modulation periods and longer waveguides, can lead to further enhancements.

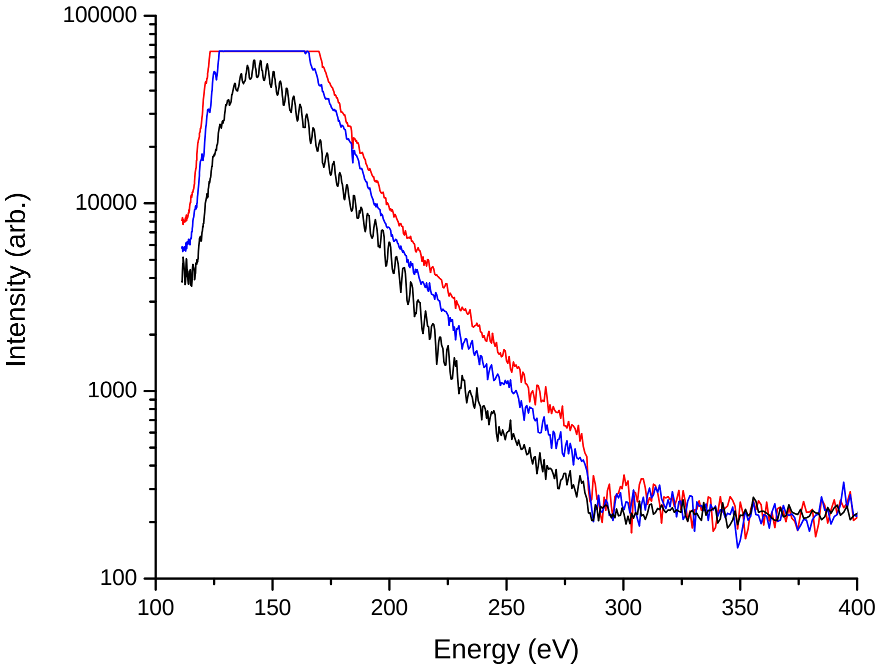

Figure 2.13: Comparison of harmonic spectra at the C edge using a 0.25 mm modulated waveguide filled with 9 Torr Ne (black), 42 Torr He (blue), and 60 Torr He (red). All spectra taken with 180 s exposure time using SB grating.

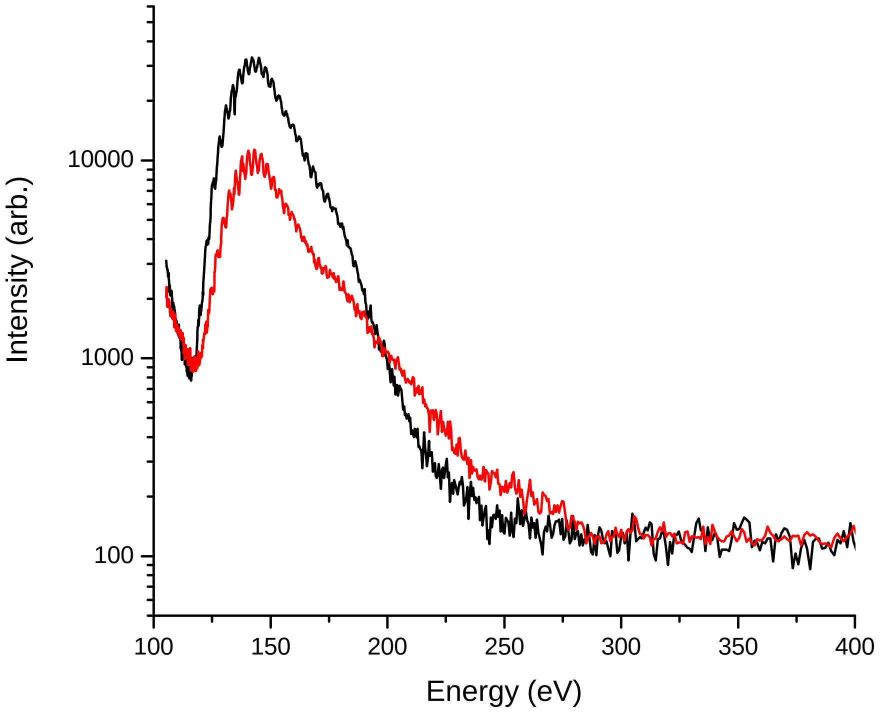

Figure 2.14: Comparison of harmonic spectra from 8 Torr Ne (black) and 15 Torr He (red) using a 0.25 mm modulated waveguide. Both spectra taken with 120 s exposure time using SB grating.

2.3 Mechanisms for Enhancement by Quasi-Phase Matching

In this section, I will discuss in more detail the physical processes that lead to enhancement of HHG in modulated waveguide structures. From propagation models,[19] we know that the effect of the diameter modulation is to change the on-axis intensity in a periodic way. The modulations of the waveguide radius occur over too short a distance for the laser mode to adiabatically follow the waveguide diameter. Instead, the change in diameter changes the boundary conditions, exciting a transverse wave that propagates to the center of the waveguide. When the transverse wave reaches the center of the waveguide, the interference causes oscillations in the intensity. Figure 2.15 shows calculations of the radial profile of the laser intensity and phase in the waveguide, showing the initial laser mode and the modes giving the maximum and minimum on-axis intensity. The calculations were performed for a 100 μm diameter waveguide with 6% modulations and a periodicity of 0.5 mm, filled with 2 Torr argon for a 15 fs pulse with a peak intensity of 5 x 10^{14} W/cm^2. The amount by which the intensity is modulated can be approximately estimated by assuming the adiabatic case where the peak intensity is proportional to the inverse of the waveguide radius squared.

2.3.1 Modulating the Amplitude of the Harmonics

The periodic modulation of the on-axis laser intensity has several different effects on the buildup of harmonic signal over the length of the waveguide. The most dominant effect occurs for the cutoff harmonics that are generated at the very peak of the laser pulse. These harmonics will only be generated in the higher intensity regions (i.e. the smaller diameter sections of the waveguide), effectively turning on and off the generation. For the lower energy harmonics, the effect of modulating the laser intensity is more complicated. In a certain time-window during the leading edge of the pulse, the intensity modulations will also turn on and off the generation of a particular harmonic. This effect is illustrated in Fig. 2.16 which shows the different times on the leading edge of the pulse where the intensity is great enough to generate a particular harmonic

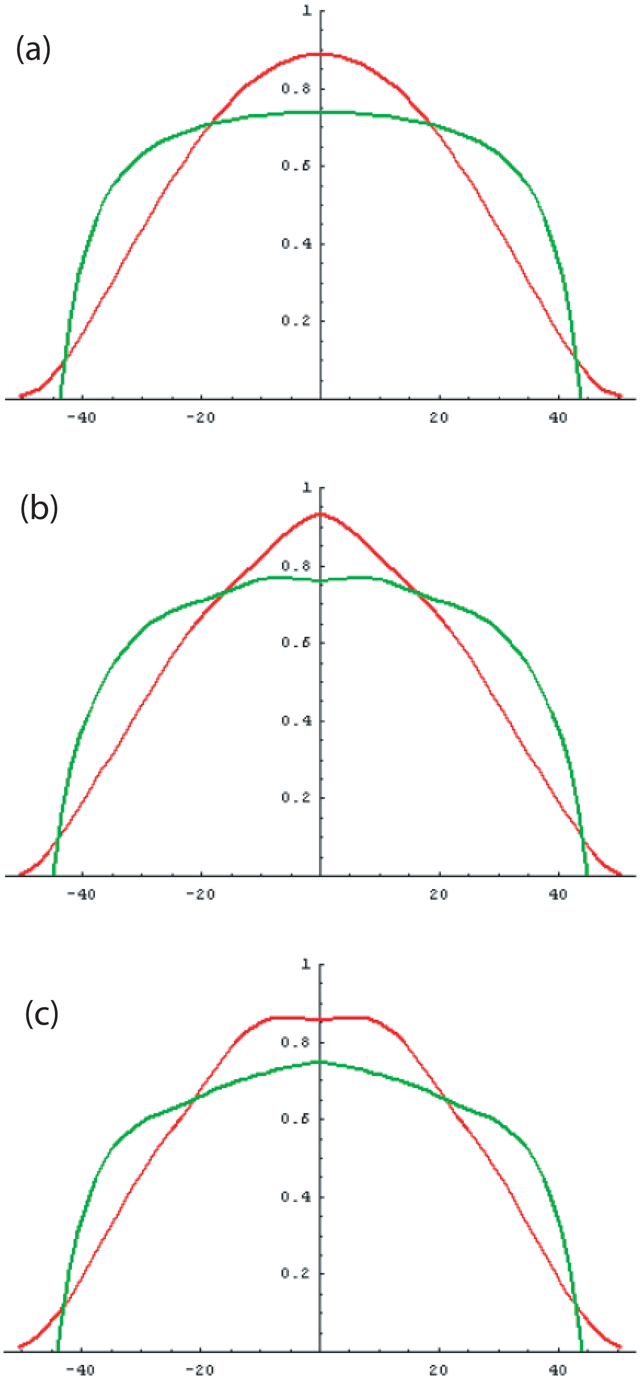

Figure 2.15: Calculations of the radial profile of the intensity (red curve) and phase (green curve) of the laser inside the modulated waveguide. The three frames correspond to: a. the initial mode, b. the mode giving the maximum on-axis intensity and c. the minimum on-axis intensity. From Ivan Christov.

when the pulse peak intensity changes by 10%. It is interesting to note that for increasing harmonic orders, i.e. higher threshold intensities, the duration of this time-window increases.

The expected enhancement due to modulating the harmonic amplitude can be modelled using the simple formalism described previously. Evaluating equations 2.4 and 2.5 gives an expression for the amplitude of the harmonic field as a function of propagation length, L:[27]

$$E_q \propto i d_{eff} E_\omega^n L e^{-i(\Delta k - K_m)L/2} G_m \frac{Sin[(\Delta k - K_m)L/2]}{(\Delta k - K_m)L/2}, \tag{2.9}$$

where the integral is dominated by the term in the sum for which $\Delta k \approx K_m$. The quasi-phase matching bandwidth is the same as the normal phase matching bandwidth shifted by the effective wavevector, K_m, so that using a longer medium with more modulated sections will narrow the bandwidth. In the case of periodically poled materials where the phase relation between the fundamental and harmonic is adjusted by 180 degrees every coherence length, the nonlinear coefficient can be expressed as a square wave function, oscillating between +1 and -1 every coherence length, with the coefficients given by:[13]

$$G_m = (2/m\pi) Sin(m\pi/2) \tag{2.10}$$

In our case, the enhancement in harmonic field is half that for the case described above since we only enhance the signal every other coherence length. For our case with perfect quasi-phase matching (i.e. $K_m = \Delta k$), the enhancement is:

$$I_q \propto (d_{eff} E_\omega^n)^2 (1/m\pi)^2 L^2 \tag{2.11}$$

The enhancement in harmonic intensity is reduced by a factor of $(1/m\pi)^2$ compared to the case of no phase mismatch. The greatest enhancement will be from m=1 quasi-phase matching and will decrease for higher values of m.

The maximum enhancement of HHG that can be achieved by quasi-phase matching depends upon how strongly the harmonic light is absorbed by the generation gas. Fortunately, going to higher photon energies, the amount of absorption by the gas decreases significantly. Figure 2.17 plots the absorption length, L_{abs}, as a function of photon energy for Ne and He

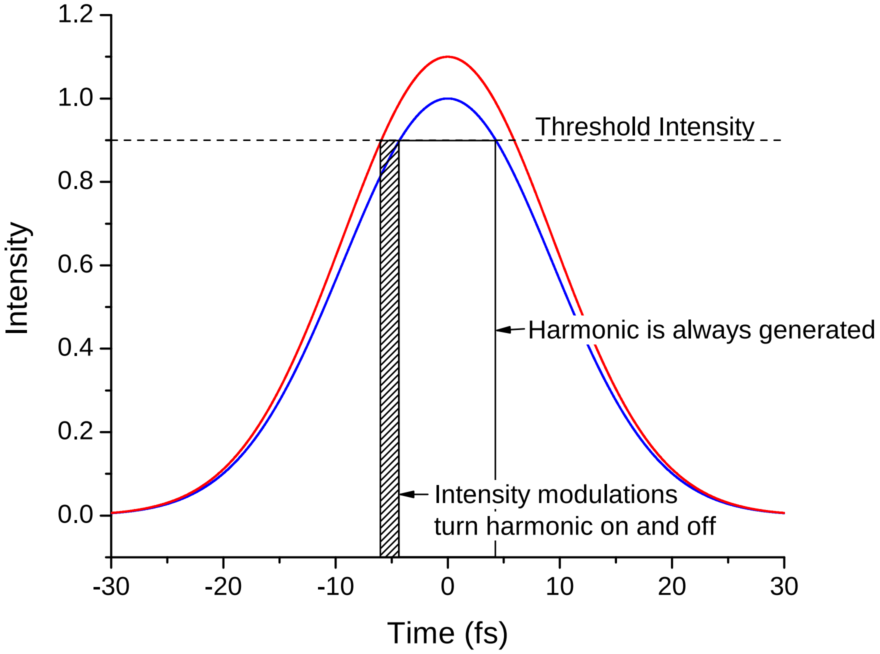

Figure 2.16: Diagram showing region in pulse where a given harmonic, only generated above the threshold intensity, is turned on and off by a 10% intensity modulation.

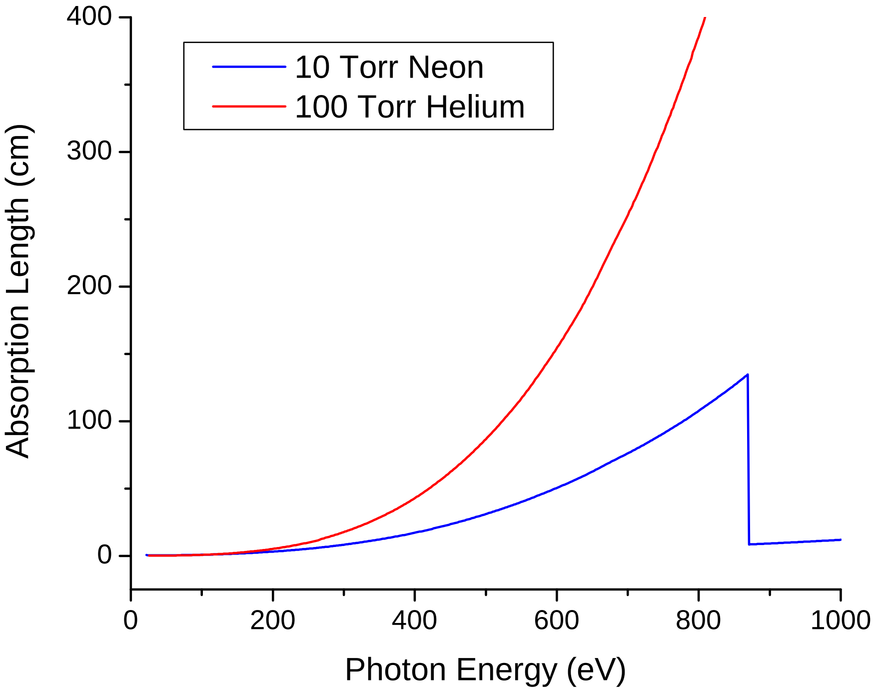

Figure 2.17: Plot of absorption length as a function of photon energy for 10 Torr Neon and 100 Torr Helium. Data from the Center for X-ray Optics, Berkeley Lab (www-cxro.lbl.gov).

gases. For higher photon energies, at and above the C-edge (284 eV), the absorption length dramatically increases reaching several meters in 100 Torr helium. For quasi-phase matching, the optimal signal is obtained at the gas pressure where the m=1 quasi-phase matching condition is met. Previous calculations have shown that the phase matched flux is optimized when the medium length is $> 3L_{abs}$ and it saturates at around $10L_{abs}$.[21] Under our typical experimental conditions, m=1 quasi-phase matching of the harmonics at the C-edge in helium gas is achieved at a pressure of 9 Torr (for a 0.25 mm modulated waveguide) and the absorption length at this pressure is $L_{abs} = 1.64$ m. Therefore, by simple estimates, the maximum signal enhancement possible would be $\sim (1/m\pi)^2(10L_{abs}/L_{coh})^2(1/e)^{10} \sim 80,000$. With shorter modulation periods, the same signal enhancement could be obtained at a higher pressure and a shorter waveguide. One issue with using such a long waveguide is the power loss associated with the fundamental mode propagation. The attenuation constant for the EH_{11} mode for 800 nm light and a waveguide radius of 75 μm is $\alpha = 0.323\ \mathrm{m}^{-1}$.[50] Also, the dispersion of the waveguide can stretch the pulse in time. The propagation length that would approximately double the pulse duration is $\sim$ 14 m.[Note: This calculation is detailed in Ch. 5] Both effects will reduce the peak intensity of the pulse as it is propagating down the waveguide, preventing quasi-phase matching over the entire length. One elegant solution to this problem, mentioned by Ivan Christov in Ref. [19], would be to use a tapered waveguide with a decreasing radius along its length, maintaining the same on-axis intensity throughout.

2.3.2 Grating-Assisted Phase Matching

Typically quasi-phase matching is implemented by a modulation of the nonlinear coefficient, however, it is also possible to achieve an enhancement from quasi-phase matching by modulating the linear optical properties. This process is termed grating-assisted phase matching.[27] Modulation of the laser intensity in the waveguide results in a modulation in the value of the phase mismatch, Δk, along the waveguide from the changing plasma dispersion. The modulation in intensity directly modulates the ionization fraction. For a sinusoidal modulation in the intensity, the plasma contribution to the phase mismatch can be expressed approximately as,

$$\Delta k_{plasma}(z) = PN_{atm}r_e q\lambda(\eta + \delta\eta\cos(2\pi z/\Lambda)), \tag{2.12}$$

where $\delta\eta$ is the change in ionization and Λ is the period of the waveguide modulations. To get an idea of the amount by which the ionization can change, Fig. 2.18 shows the ionization as a function of time for two different laser intensities calculated from ADK ionization rates. At the peak of the pulse, the ionization fraction is 0.35 for an intensity of 10^{15} W/cm^2 and 0.41 when the intensity is increased by 5%. The value of Δk_{plasma} therefore changes by 16%. Dramatic enhancement of the harmonic signal can be obtained if the phase mismatch varies sinusoidally with a period of twice the coherence length of the average value of Δk. Mathematically, the phase mismatch is expressed by:

$$\Delta k = \frac{\pi}{L_c}(1 + \alpha\sin(\frac{\pi z}{L_c})), \tag{2.13}$$

where α is the fractional change. Figure 2.19 shows the calculated harmonic intensity for a sinusoidally varying phase mismatch for variations of 1, 3, and 5 %. It is interesting that the smaller variation can give more signal enhancement, but only over a longer propagation distance. The largest enhancement for a 1 % modulation occurs for a propagation distance of $\sim$ 125 coherence lengths and gives a factor of 2000. Figure 2.20 shows the harmonic signal for the first 60 coherence lengths. At the beginning, the QPM process is working until a certain distance at which the signal buildup reverses and then oscillates.

These calculations only take into account the effect of ionization, as would be the case if one could artificially create a longitudinally varying ionization in a straight waveguide. In the modulated waveguide, however, there is also a spatial phase due to the periodic refocusing of the fundamental light. The combination of both effects must be taken into account to understand the amount of enhancement under real experimental conditions.

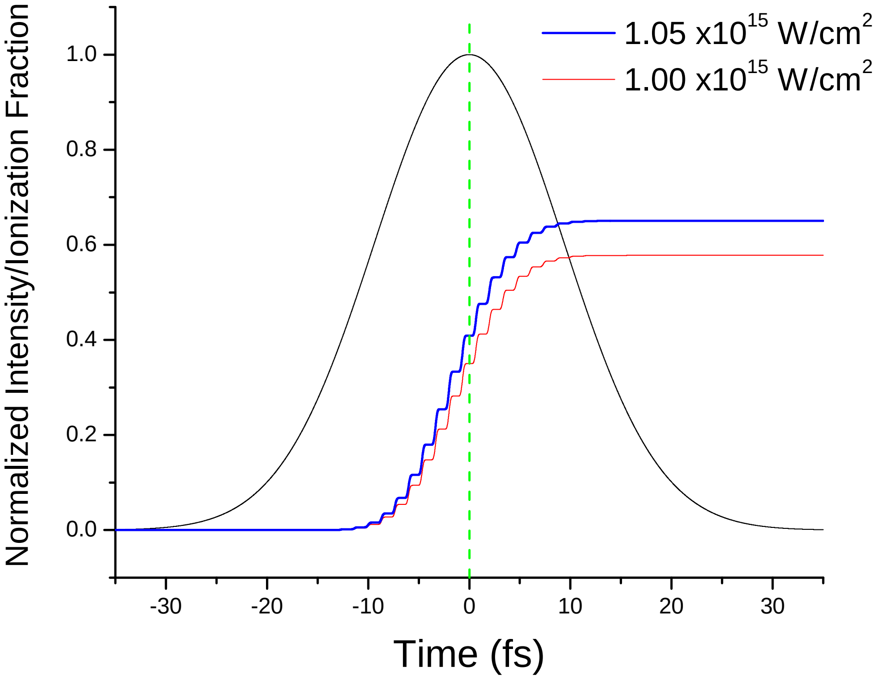

Figure 2.18: Comparison of ionization fraction of neon as a function of time for a 22 fs duration pulse at different peak intensities.

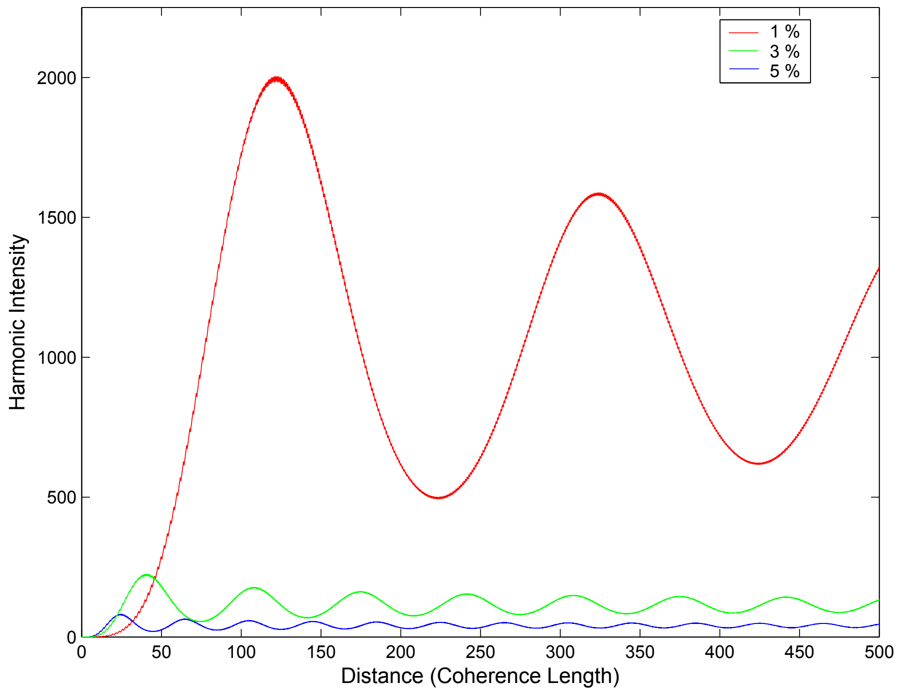

Figure 2.19: Harmonic intensity as a function of propagation distance for the case where the phase mismatch varies sinusoidally by 1, 3, and 5 % with a period of 2 coherence lengths.

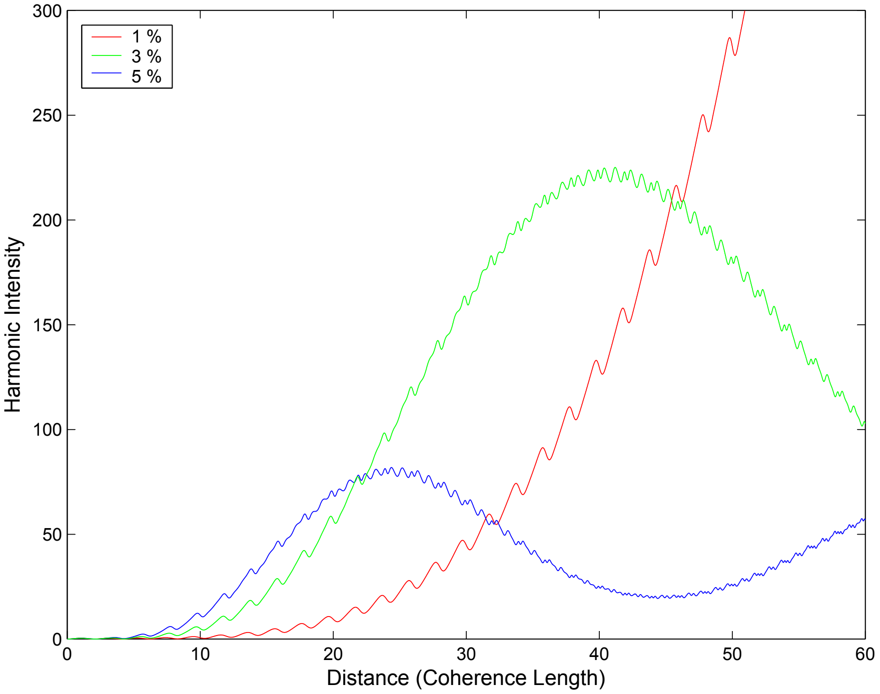

Figure 2.20: Plot of the harmonic intensity during the first 60 coherence lengths.

2.3.3 Intrinsic Phase Effects

Another mechanism for quasi-phase matching arises from the finite time response of the harmonic generation process, causing an intensity-dependent phase of the emitted harmonics. The Lewenstein model of HHG, discussed in Ch. 1, describes the phase of the emitted harmonics as the phase the electron wavefunction acquires from when the atom is ionized to the time it recombines. Due to this intrinsic phase, modulation of the intensity of the driving laser can periodically adjust the phase relationship between the harmonics and the fundamental laser.

The full expression for the harmonic phase relative to the fundamental is given by:[9]

$$\Phi = q\omega t_f - S(t_0, t_f)/\hbar, \tag{2.14}$$

where q is the harmonic order, ω is the fundamental laser frequency and $S(t_0, t_f)$ is the quasi-classical action of the electron from the time the atom is ionized, t_0, to when the electron recombines, t_f. The quasi-classical action is given by the expression:

$$S(t_0, t_f) = \int_{t_0}^{t_f} (\frac{p^2}{2m} + I_p)dt \tag{2.15}$$

where p is the electron momentum, m is the electron mass, and I_p is the ionization potential of the atom. Previous theoretical work has solved for the phase of the harmonics using the method of stationary action.[47, 29] Here, I will follow a slightly different approach, solving the integral in Eqn. 2.15 numerically over the classical trajectory of the free electron to determine the harmonic phase.

The classical trajectory of a free electron in the laser field is given by:

$$m\frac{dv}{dt} = -eE(t). \tag{2.16}$$

Making the assumption of a monochromatic laser field: $E(t) = E_0 Cos(\omega t)$, the equations of motion for the electron are:

$$v(\phi, \phi_0) = \frac{-eE_0}{m\omega}(Sin\phi - Sin\phi_0) \tag{2.17}$$

and

$$x(\phi, \phi_0) = \frac{eE_0}{m\omega^2}(Cos\phi - Cos\phi_0 - Sin\phi_0(\phi - \phi_0)), \tag{2.18}$$

where $\phi = \omega t$ and $\phi_0 = \omega t_0$ is the phase in the laser cycle when the atom is ionized, termed the release phase. From the equations of motion, we can solve for the phase, ϕ_f, when the electron returns to the position of the ion. This return phase as a function of the release phase is plotted in Fig. 2.21. It is then straightforward to solve for the electron's velocity, and therefore its kinetic energy, when it re-encounters the ion. Fig. 2.22 plots the kinetic energy as a function of the electron's release phase. From Fig. 2.22 it is evident that for the harmonics at the cutoff, there is only one classical trajectory; however, for the plateau harmonics, there are two different trajectories (short and long) with the same return kinetic energy. For the short trajectories, the electron is released at a phase $>$ 18 degrees, and re-encounters the ion in less than half an optical cycle. The duration of the long trajectories, however, is almost a full optical cycle and therefore the electron acquires more phase.

Combining equations 2.15 and 2.17 gives the following expression for the intrinsic phase of the harmonics due to the phase that the electron acquires in its trajectory as a function of the release phase, ϕ_0, and the return phase ϕ_f:

$$\phi_{intrinsic} = \frac{I_p}{\hbar\omega}(\phi_f - \phi_0) + \frac{2U_p}{\hbar\omega}\int_{\phi_0}^{\phi_f}(Sin\phi - Sin\phi_0)^2 d\phi, \tag{2.19}$$

where the definition of the ponderomotive energy, $U_p = e^2E^2/4m\omega^2$, is used. For the case of very high harmonic orders where the condition $U_p >> I_p$ is met, the first term in Eqn. 2.19 can be neglected and the electron kinetic energy is approximately equal to the emitted photon energy. Using this assumption, the intrinsic phase as a function of harmonic energy is calculated, plotted in Fig. 2.23. To find the harmonic phase relative to the fundamental, it is necessary to include the first term in Eqn. 2.14. The result for the harmonic phase relative to the fundamental is shown in Fig. 2.24.

For quasi-phase matching, it is important to know how the harmonic phase changes with laser intensity. Fig. 2.25 plots the result for the intensity dependence of the harmonic phase for two different harmonic orders, assuming an 800 nm driving laser and the condition $I_p = 0$. The long trajectories have a linear intensity dependence equal to $\sim$ -23 x 10^{-14} Radians$\cdot$cm^2/W. The

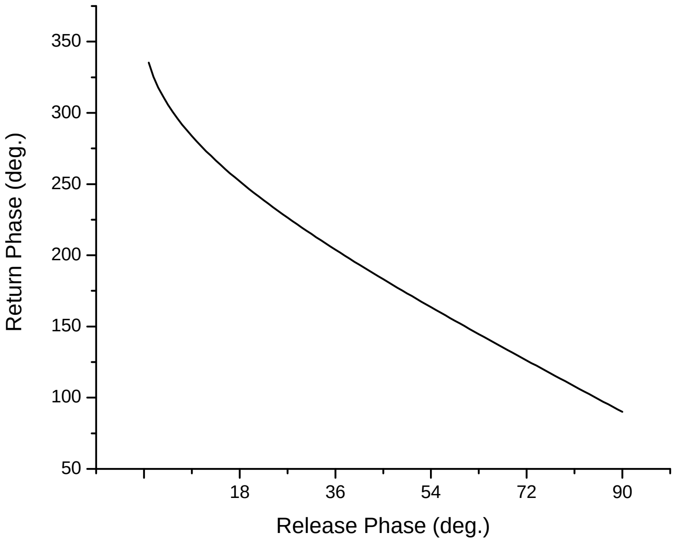

Figure 2.21: Return phase, ϕ_f, as a function of the release phase, ϕ_0, determined by the classical equations of motion.

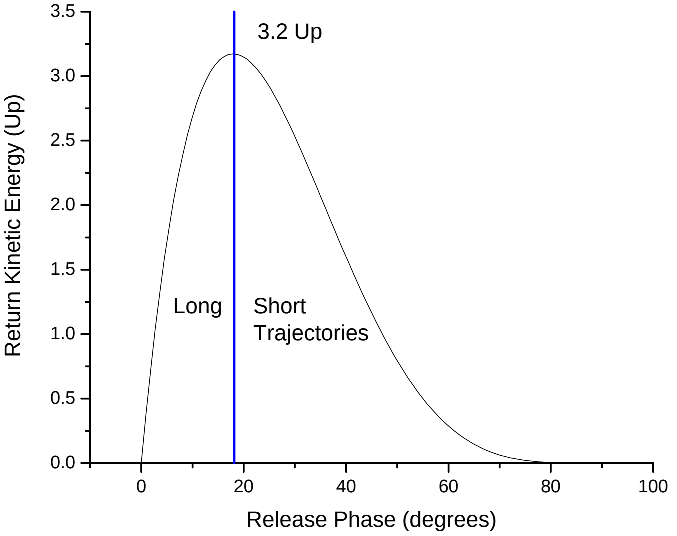

Figure 2.22: Electron return kinetic energy for trajectories with different release phases, ϕ_0. The long and short trajectories are indicated.

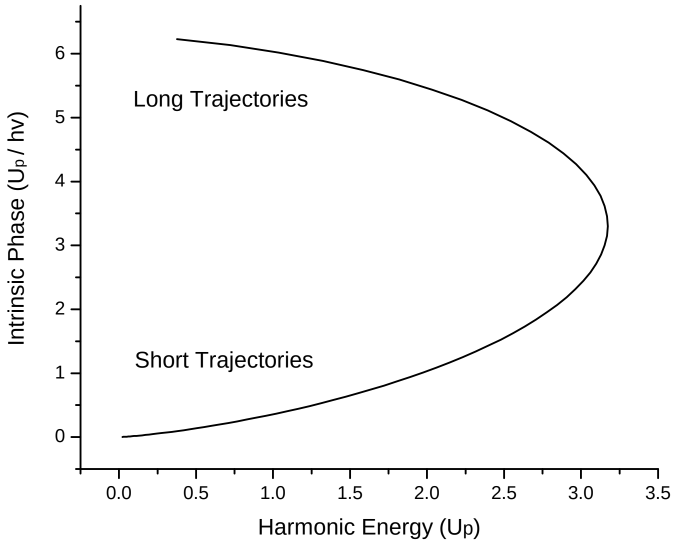

Figure 2.23: Intrinsic phase as a function of harmonic energy. The long trajectories acquire more phase than the short trajectories.

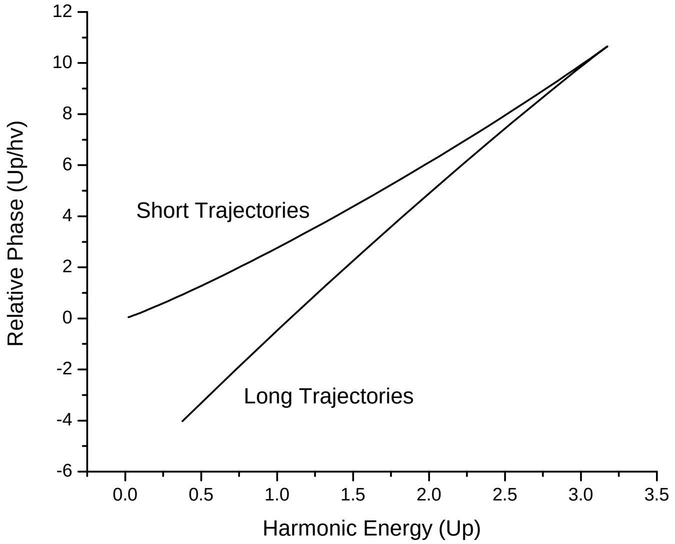

Figure 2.24: Plot of harmonic phase in reference to the fundamental as a function of harmonic energy. Note there is a linear dependence which is different for the long and short trajectories.

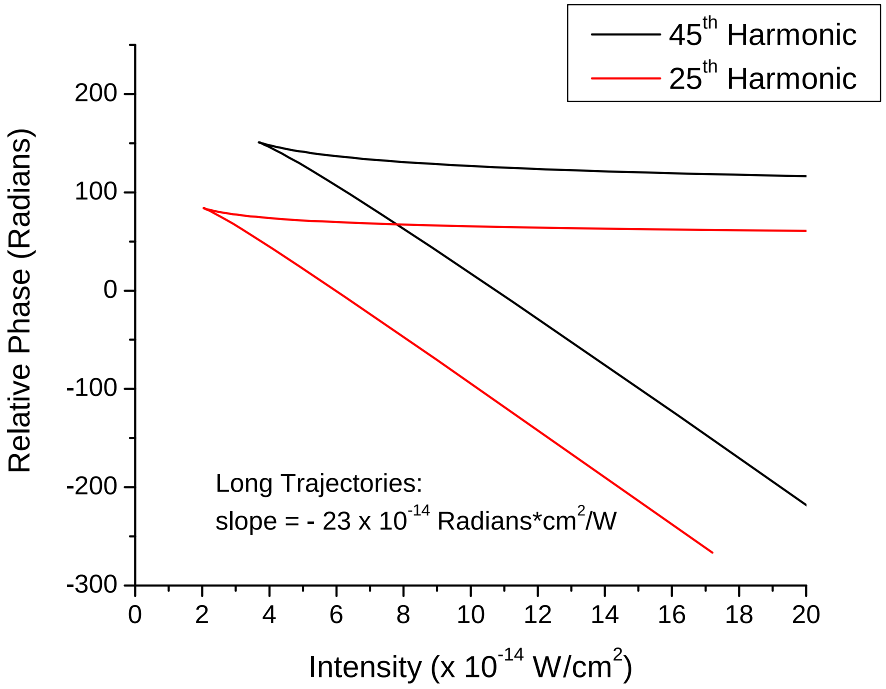

Figure 2.25: Plot of the intensity dependence of the harmonic phase for two different harmonic orders. The calculation was done for a fundamental wavelength of 800 nm.

short trajectories have a more complicated dependence on intensity which is not exactly linear and is significantly smaller than the long trajectories. For the condition $I_p = 0$, the intensity dependence of the phase is not a function of harmonic order. It is interesting to compare these results with previous work done using the method of stationary action. Lewenstein et al. calculated that for $I_p = 0$, the harmonic phase varies with intensity as -4.08 $U_p/\hbar\omega$ at the cutoff and as -6.28 $U_p/\hbar\omega$ in the plateau region (accounting only for the long trajectories).[47] Using the definition for the ponderomotive energy, these values correspond to: -15.7 x 10^{-14} cm^2/W and -24.2 x 10^{-14} cm^2/W for 800 nm light.

For the long trajectories, an intensity change of 1.4 x 10^{13} W/cm^2 would produce a phase shift of π, while the same phase shift for the short trajectories at the cutoff would require a change of 3.4 x 10^{13} W/cm^2. This corresponds to an intensity change of 1.4 and 3.4 % if using a driving laser intensity of 10^{15} W/cm^2. Therefore, the intensity-dependent harmonic phase does play a role in the quasi-phase matching of the emission of harmonics generated at the cutoff for intensities around 10^{15} W/cm^2 and above.

2.4 Generation of an Enhanced Attosecond Pulse through Phase Matching

An important aspect of phase matching and quasi-phase matching of high-order harmonic generation is the changing amount of ionization during the pulse which creates a narrow time window over which the phase matching condition is met. Only the harmonics generated in this time window are enhanced, making it possible to generate a single enhanced attosecond-duration pulse. To illustrate this, Fig. 2.26 shows a calculation using ADK theory of the phase mismatch as a function of time during the laser pulse. The dashed line in the figure shows when the phase matching condition is met for quasi-phase matching with a periodicity of 0.25 mm. Fig. 2.27 shows a simple calculation of the expected intensity of the 171^{st} harmonic as a function of time during the laser pulse from quasi-phase matching using Eqn. 2.9. Note that longer propagation lengths will both increase the signal and shorten the duration of the time window.

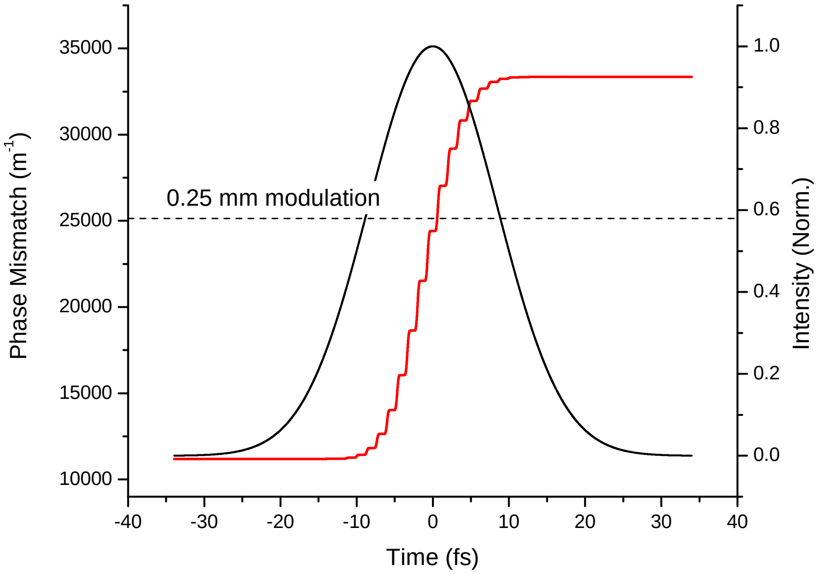

Figure 2.26: Calculation of the phase mismatch (Δk) for the 171^{st} harmonic in 3 Torr neon for a 20 fs duration pulse with a peak intensity of 10^{15} W/cm^2. The dashed line indicates when the QPM condition is met for a modulation period of 0.25 mm.

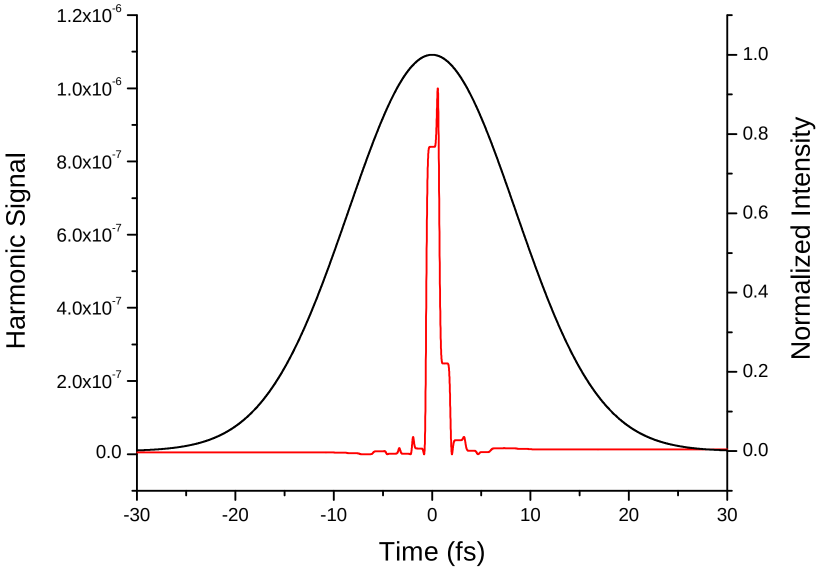

Figure 2.27: Calculation of the harmonic signal of the 171^{st} harmonic in 3 Torr neon for a 20 fs duration pulse with a peak intensity of 10^{15} W/cm^2 by quasi-phase matching with 0.25 mm periodicity. Here, the propagation length is 1 mm.

Enhancement of a single attosecond-duration pulse by quasi-phase matching was first predicted by Ivan Christov in Ref. [19]. Propagation of the laser in the hollow-core waveguide is modelled by numerical solution of the three-dimensional scalar wave equations. The harmonic emission is calculated from a quasi-classical approximation of the dipole moment. Fig. 2.28 shows the harmonic spectrum after propagation through a 1 cm long straight and modulated waveguide. Fig. 2.29 shows the temporal properties of the harmonic output for the straight and modulated waveguides. Because the coherence lengths for neighboring harmonics are similar, the modulated waveguide enhances several harmonics in the cutoff region. Temporally, the emission from these harmonics is phase matched over a single cycle of the driving laser, creating a single attosecond-duration pulse.

Experimentally, the effect of phase matching over a single cycle of the driving laser was observed by Durfee et al. in Ref.[26]. For phase matching in a straight waveguide, they calculated that tuning the pressure would allow phase matching at different half cycles of the pulse (i.e. different ionization levels). Figure 2.30.a shows their calculation of the pressure dependence of the flux of the 29^{th} harmonic for a 20 fs pulse in Ar gas. The different peaks correspond to optimal phase matching at different ionization "steps". Experimentally, they observed that in the pressure region corresponding to phase matching, the flux was rapidly oscillating, Fig. 2.30.b, attributed to the sensitivity of the amount of ionization on the carrier-envelope offset (CEO) of the pulse, illustrated in Fig. 2.31. However, in the lower pressure region where the process is not phase matched, the signal does not fluctuate since it is not sensitive to the CEO of the pulse.

The rapidly increasing ionization from the HHG process, together with a stable carrier-envelope offset, may make it possible to phase match only the emission from a particular single half cycle of the driving laser, giving a single, enhanced attosecond-duration pulse. Without phase matching, it is only possible to generate a single attosecond pulse by using an extremely short driving laser (i.e. 6 fs in duration). Generating such a short pulse at the fundamental involves complicated pulse compression techniques which greatly decrease the pulse energy and

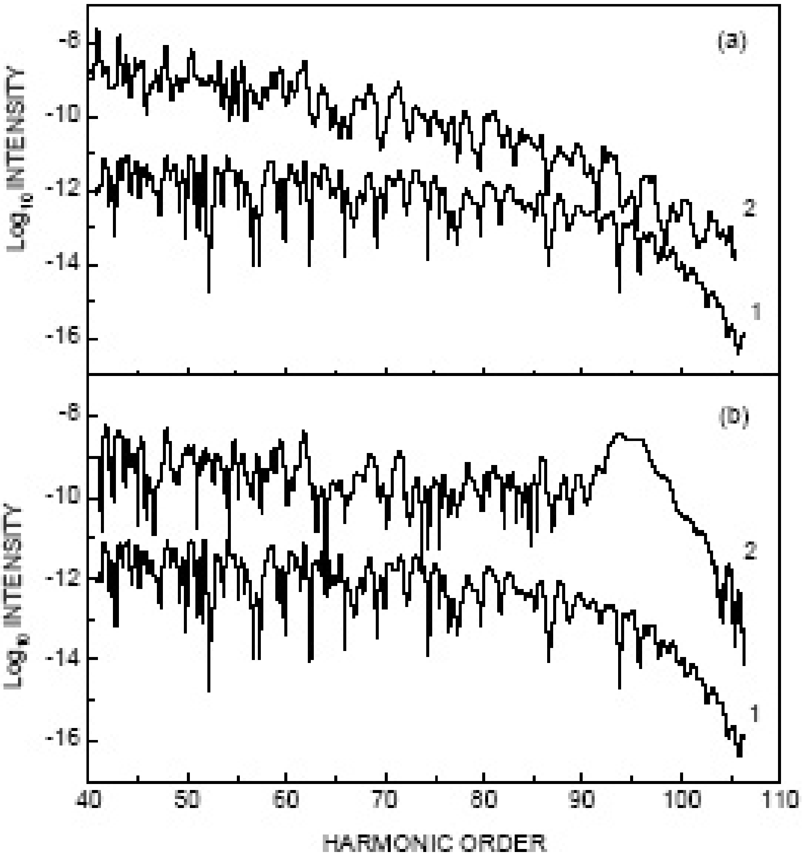

Figure 2.28: Calculation of the harmonic spectra for (a) a straight waveguide and (b) a 0.5 mm periodicity modulated waveguide for a 15 fs duration pulse with an intensity of 7 x 10^{14} W/cm^2 in 1 Torr Ar. The calculated single atom spectrum is also shown.

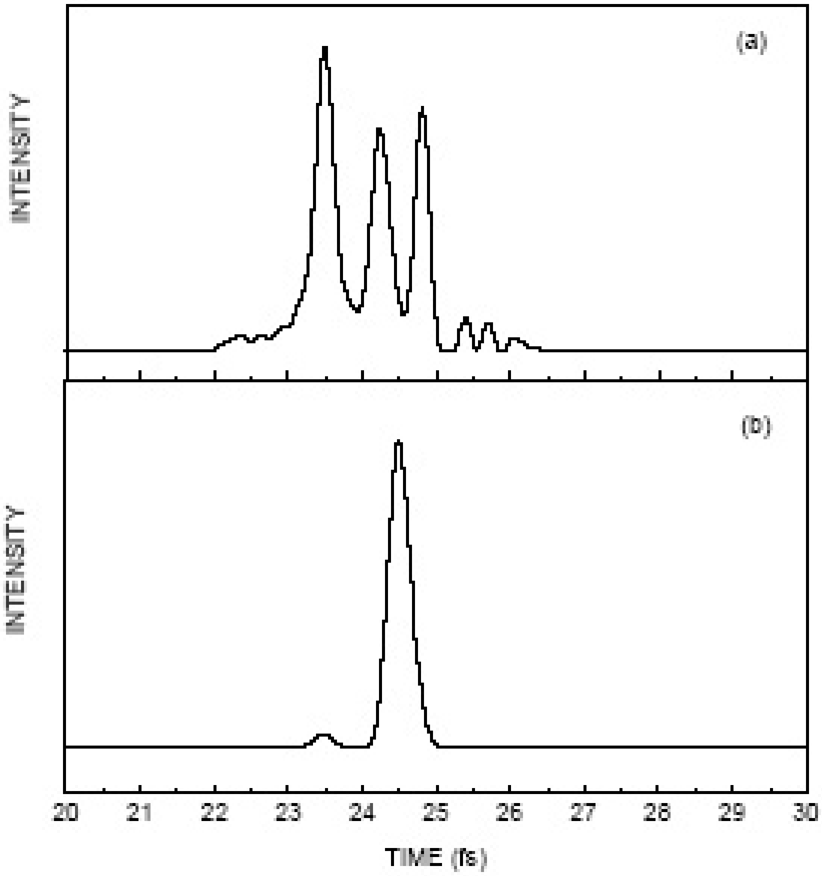

Figure 2.29: Calculation of the time dependence of the harmonic output for (a) the straight waveguide and (b) the 0.5 mm periodicity modulated waveguide.

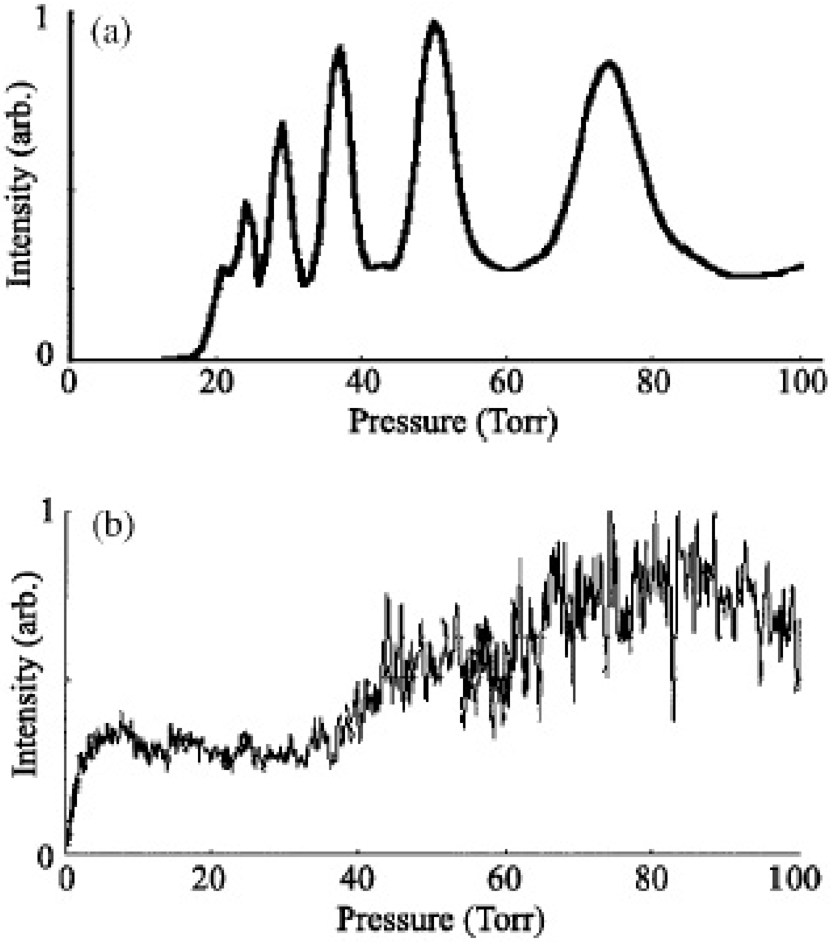

Figure 2.30: a. Calculation of the flux of the 29^{th} harmonic for a 20 fs laser pulse and peak intensity of 2.2 x 10^{14} W/cm^2 as a function of argon pressure using a 3 cm waveguide. b. Experimentally measured flux for the same conditions as part a. From [26].

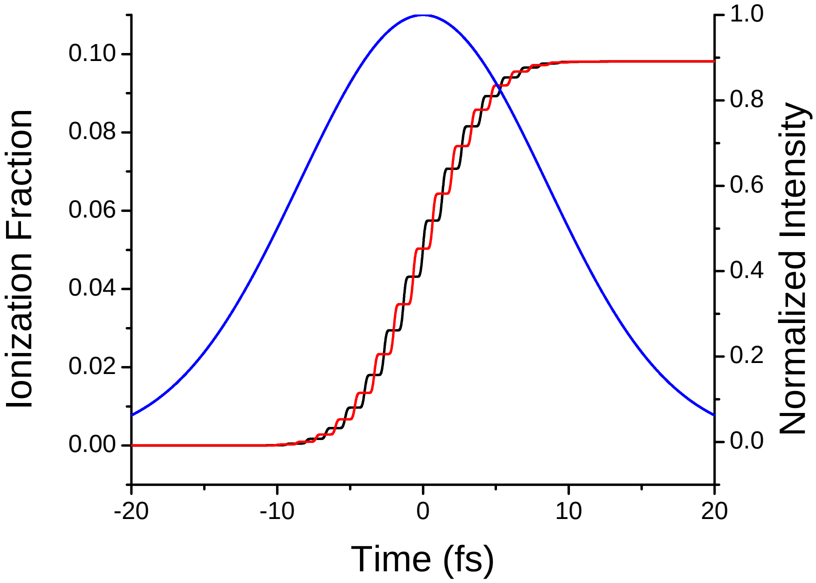

Figure 2.31: Calculation of the fractional ionization of argon using ADK ionization rates for a 20 fs pulse with peak intensity of 2.2 x 10^{14} W/cm^2 for a cosine (black) and sine (red) pulse.

stability (since they rely on nonlinear processes to broaden the spectrum). Phase matching in hollow waveguides thus presents a more elegant, stable, and efficient method for attosecond pulse generation.

Chapter 3

High Harmonic Generation from Ions

The highest photon energies obtained from high harmonic generation (HHG) have generally been limited not by the cutoff rule, but by the detrimental effects of ionization when using high laser intensities. The resulting plasma can defocus the laser beam,[59] limiting the peak intensity and therefore U_p. It also causes a significant phase velocity mismatch between the driving laser and the harmonic light, greatly reducing the harmonic signal. Ionization can be kept to a minimum by using shorter-duration laser pulses or atoms with a large ionization potential, thus allowing the atoms survive to high laser intensities before ionizing. The highest harmonics observed to date, at around 950 eV, have been generated using helium,[15, 70, 67] which has the largest ionization potential of the noble gases. However, helium also has an exceptionally small effective nonlinearity, which limits the harmonic flux. Larger, multi-electron atoms such as argon typically generate greater signals, but the highest observable harmonic orders have been comparatively lower. For example in Ar, photons of greater than 100 eV energy have never been observed using an 800 nm driving laser,[83, 80] even using very short 7 fs duration pulses[65] or large pulse energies. In other work, a longer-wavelength driving laser was used to increase the harmonic emission in Ar to ~ 150 eV.[68] Using longer wavelengths increases the value of U_p for the same laser intensity, however, this approach also reduces the efficiency of the process since the electron wavefunction is more delocalized, lowering the probability of recombination.

3.1 Previous Experiments on HHG from Ions

Harmonic emission from neutral atoms is limited by the saturation intensity, or the intensity at which $\sim 98\%$ of the atoms are ionized. However, emission from ions can in theory extend to very high energies, since the saturation intensity for each successive stage of ionization is progressively higher. Krause, Kulander, and Schaffer calculated that emission from neutrals and ions is of comparable strength with emission from ions extending to higher energies.[42] In previous experiments, Wahlstrom et al. observed harmonic emission from Ar ions up to ~ 100 eV using an 800 nm driving laser with 250 fs pulse width and 250 mJ of pulse energy focused to an intensity of $\sim 10^{15}$ W/cm^2. Their results are shown in figure 3.1. The emission attributed to ions is several orders of magnitude weaker in intensity than the emission from neutral atoms and is still short of the predicted $I_p + 3.2U_p$ rule.[79, 80]

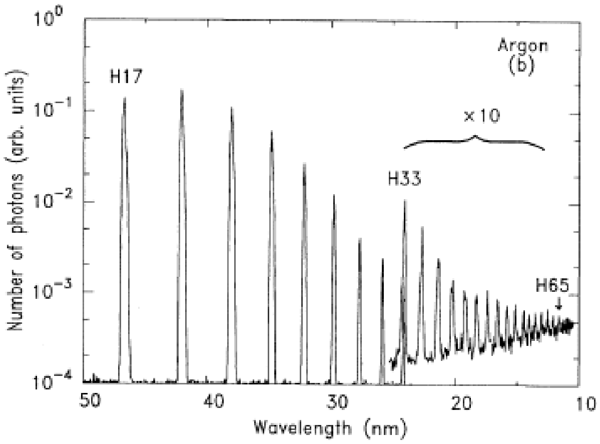

Figure 3.1: Harmonic emission from argon using a gas jet with 250 mJ pulse energy and a 250 fs pulse. From [80]

3.2 Experimental Results using Hollow-core Waveguides

In our experiment, high harmonics are generated by focusing intense laser light into a hollow-core waveguide filled with low pressure gas. The waveguide has several advantages over a gas jet. It counteracts the effect of plasma-induced defocusing, allowing high laser intensities to be achieved in a fully ionized gas medium. Also, using a modulated-diameter waveguide, the large phase mismatch associated with ionization can be partially compensated by quasi-phase matching. As a result, we observed harmonic generation from argon up to 250 eV, an extension of 100 eV over previous results using a gas jet setup for HHG. These results demonstrate that emission from ions can greatly increase the photon energies obtainable from HHG and that large ions such as Ar, with high nonlinear susceptibilities compared to He, can be used to generate harmonic emission at energies above 200 eV, in the soft x-ray region of the spectrum.

In our experiment, we use a 1 kHz Ti:sapphire laser system[8] producing 22 fs-duration pulses, with pulse energies of 3 mJ. The laser light is focused into 150 μm inner-diameter, 2.5 cm long, hollow-core waveguides filled with argon. The harmonic emission emerging from the waveguide passes through a zirconium or silver filter to block the fundamental light. Frequency-resolved-optical-gating (FROG) measurements of the laser pulse before and after the fiber filled with low-pressure Ar show some shortening of the pulse from the 22 fs input to 18 fs at the exit due to ionization effects to be discussed in Chapter 5. Care was taken to prevent contamination of the gas by evacuating the waveguide first to $\sim 10^{-2}$ Torr, and then flowing Ar continuously through it. Figure 3.2 shows the harmonic emission from a straight waveguide filled with 7 Torr of Ar at a peak laser intensity of $\sim$ 9 x 10^{14} Wcm^{-2}. Under these conditions, the harmonic emission extends up to 180 eV. The falloff in the spectrum toward low energies is a result of the transmission characteristics of the Zr filter used to reject the laser light. Here, we use a 0.4 μm thick Zr filter with 25 nm of Ag coated on one side. When a 0.25 mm-modulated waveguide was used under the same conditions, the highest photon energy observed was the same; however, the signal was 2-3 times stronger.

The laser intensity was determined from the experimentally measured pulse energy and pulsewidth, and is accurate to within 10%. This intensity was also compared with that required to generate the experimentally observed harmonic cutoff, which gives a lower limit for the intensity. Figure 3.3 shows the harmonic emission from Ar at a slightly higher laser intensity of 1.3 x 10^{15} Wcm^{-2} using a waveguide with a periodically modulated diameter.[56] We use a 0.45 μm thick Ag filter that is 5-15% transmissive from around 120 to 385 eV to reject the laser light. In Fig. 3.3, the emission from Ar at this higher intensity now extends up to 250 eV. Note that the increase in observable harmonic order scales linearly with intensity, as expected from the cutoff rule provided that saturation effects do not limit the emission. The signal is clearly emission from HHG since the signal disappears if circularly polarized driving pulses are used.

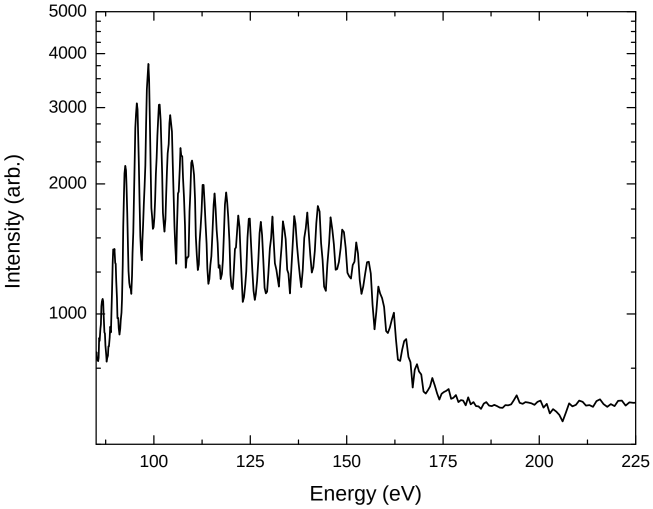

Figure 3.2: Harmonic emission from a straight 150 μm inner diameter, 2.5 cm long fiber filled with low-pressure Ar (7 Torr), driven by an 800 nm laser with an 18 fs pulse duration and a peak intensity of 9 x 10^{14} Wcm^{-2}. The spectrum was taken using the SC grating and an exposure time of 300 s.

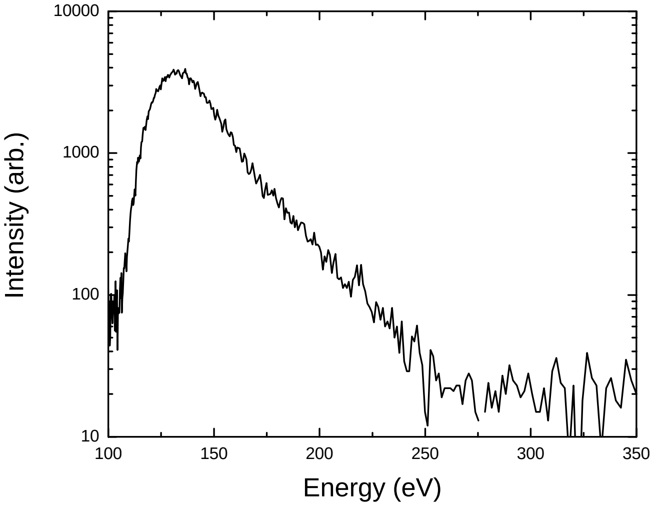

Figure 3.3: Harmonic emission at a higher peak laser intensity of 1.3 x 10^{15} Wcm^{-2}, using a 0.25 mm period modulated waveguide. The spectrum was taken using the SC grating with a 600 s exposure time.

3.3 Evidence for Harmonic Emission from Ions

The laser intensities required to generate the highest harmonics shown in Figs. 3.2 and 3.3 are above the saturation intensity for neutral Ar atoms of 7.5 x 10^{14} Wcm^{-2}, for an 18 fs laser pulse duration. Thus, we attribute the highest observed harmonics, in the energy range from $\sim$ 160 eV to 250 eV, to emission from Ar ions. To illustrate this, Fig. 3.4 shows the calculated population fractions of Ar, Ar+, and Ar++ as a function of time during the laser pulse at a peak laser intensity of 1.3 x 10^{15} Wcm^{-2}, and for a laser pulsewidth of 18 fs. These parameters correspond to the experimental conditions of Fig. 3.3. This calculation was done using the well-established Ammosov-Delone-Krainov (ADK) ionization rates, given in more detail in appendix A.[3] The left axis gives the population fractions for the various species. The right axis plots the HHG cutoff calculated from the cutoff rule for the laser intensity profile. In this calculation, $h\nu_{max} = I_p + 3.17U_p$, where I_p is the ionization potential Ar of 15.8 eV, and where the instantaneous laser intensity is used to calculate U_p. (Note that I_p for Ar+ is 27.6 eV, which would shift the harmonic energies slightly higher for the emission from ions). At a laser intensity of $\sim$ 7.7 x 10^{14} Wcm^{-2}, Ar is fully ionized, and the highest observable harmonics from the neutral atoms should therefore be approximately 160 eV. At the same laser intensities where the population of Ar neutrals is zero, the population of singly ionized Ar+ ions is significant. Figure 3.5 shows the ionization rates multiplied by population at a given time during the driving pulse for Ar and Ar+. Near the peak of the pulse, the rate for Ar+ dominates and therefore is the source of the HHG emission. Note that in this analysis, the assumed 18 fs pulse width is conservative; if the laser pulse is longer, full ionization of neutrals occurs at even lower laser intensities in the pulse and therefore strengthens the argument for emission from ions. The laser pulse cannot be shorter than 18 fs because of spectral bandwidth limits. Finally, the same arguments can be used for the lower intensity data corresponding to Fig. 3.2 - the higher harmonics must be emitted from ions, because Ar is fully ionized well before the peak of the pulse.

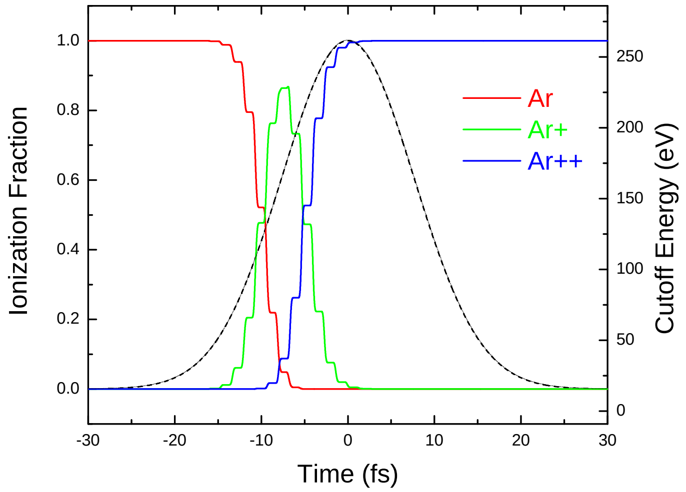

Figure 3.4: Calculated ionization levels in argon for an 18 fs laser pulse at a peak laser intensity of 1.3 x 10^{15} Wcm^{-2}, using ADK rates. Laser pulse (black dashed); Ar (red); Ar+ (green); Ar++ (blue). The right axis shows the predicted HHG cutoff energy for the laser intensity profile, calculated from the cutoff rule.

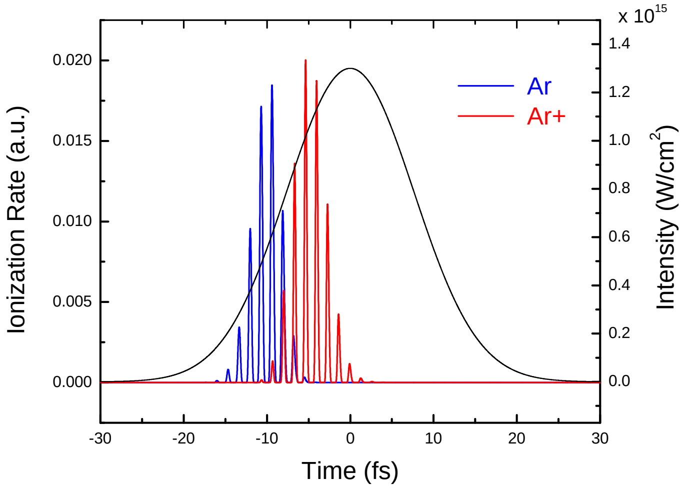

Figure 3.5: Calculated ionization rates of argon species for the same conditions as in Fig. 3.4.

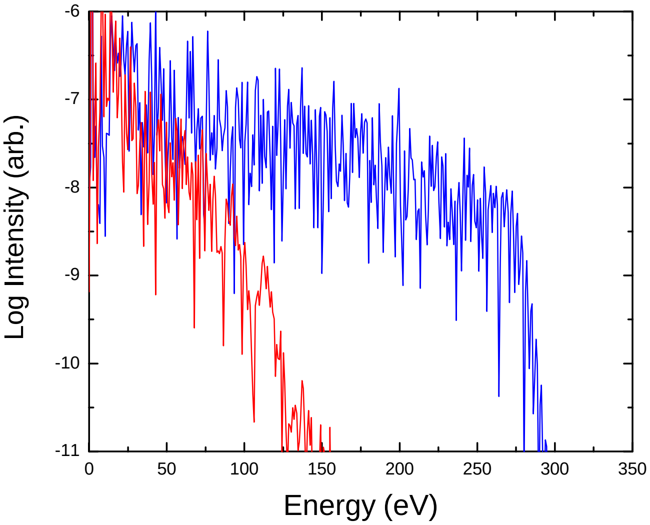

Figure 3.6: Calculated harmonic emission from neutral (red) and singly ionized Ar (blue) for an 18 fs laser pulse centered at 800 nm, at a laser intensity of 1.3 x 10^{15} Wcm^{-2}. The ion spectrum has not been corrected for the dynamically varying populations.

As further evidence for HHG from ions, we can compare the observed spectra with the predictions of a fully quantum single-active electron approximation model that uses a soft core potential to fit the ionization potential of the atom or ion under consideration.[37, 20] Only qualitative comparisons are possible since the theory does not account for propagation effects or the changing fraction of ionized species. Figure 3.6 shows predictions of the quantum model for the harmonic spectrum emitted by Ar and Ar+ for an 18 fs driving-laser pulse at a peak intensity of 1.3 x 10^{15} Wcm^{-2}. The model predicts strong emission from neutrals up to photon energies of 125 eV. For higher harmonics, the intensity drops rapidly by many orders of magnitude with increasing harmonic order due to the complete ionization of Ar neutrals. In contrast, emission from Ar+ is much stronger up to 260 eV. These theoretical predictions are in very good qualitative agreement with our experimental observations. We also note that the quantum calculations predict comparable emission intensities (i.e. effective nonlinear susceptibilities) for neutrals and ions. This is consistent with our observations, which do not show a large discontinuity in emission intensity with higher harmonic orders.

3.4 Validity of the ADK Model in the BSI Regime

One important question to address is whether the ADK model, which is valid in the tunnelling ionization regime, is applicable in the barrier suppression ionization (BSI) regime. Barrier suppression occurs when the electric field strength is comparable or greater than the strength of the binding potential of the atom, allowing the electron to escape directly from the potential well without tunnelling. This would lead to inaccuracies in the predictions of Figs. 3.4 and 3.5, although the quantum rate calculations and their predictions shown in Fig. 3.6 are valid in this regime. Barrier suppression of an atom occurs for a field strength of $E_{bs} = I_p^2/4$, or, in the case of Ar, an intensity of 2.5 x 10^{14} Wcm^{-2}.[41, 5] Previous theoretical work has shown that in this regime, ADK theory may overestimate the ionization rate and thus underestimate the cutoff harmonic order from neutrals.[66, 71] Figure 3.7 shows the static field ionization rates for H and He from a numerical solution of the time-dependent Schroedinger equation and from

ADK theory. Above the barrier supression field strength, ADK begins to overestimate the rate. However, when calculating the total ionization over the pulse, the error is less because only the peak of the pulse has an intensity in the BSI regime. In Figure 3.8, the total amount of ionization of H is calculated as a function of peak electric field amplitude and pulse duration. As expected, for a shorter duration pulse, the error in the total amount of ionization is greater since a higher proportion of the pulse is at the BSI intensity.

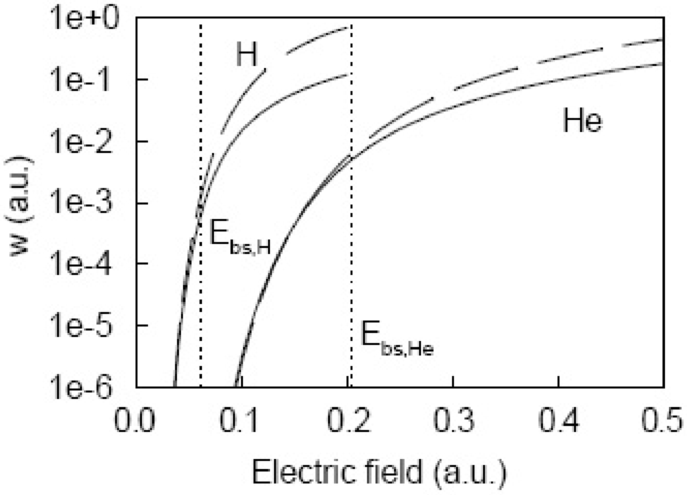

Figure 3.7: Static ionization rates of H and He versus electric field strength. Solid line: numerical calculations of TDSE. Dashed line: ADK theory. From [66].

Another source of error can result from the fact that the ADK theory describes a DC tunnelling rate. In the quasi-static approximation (QSA), these rates can be applied to oscillating electric fields if the tunnelling time is less than the oscillation period, or when the Keldysh parameter, $\gamma \leq 1/2$, where

$$\gamma = (\frac{I_p}{2U_p})^{1/2} = \sqrt{2mI_p}\omega_0/E. \tag{3.1}$$

However, A. Scrinzi et al. [66] point out that in the BSI regime, $\gamma_{bs} = 16\omega_0/(2I_p)^{3/2}$, which for 800 nm light and noble gas atoms (Kr, Ar, Ne, He) ranges between $\gamma \approx 0.5 - 2$, so that the quasi-static approximation may not be valid. By comparing numerical calculations with calculations using the QSA of the total amount of ionization produced from a pulse, they find

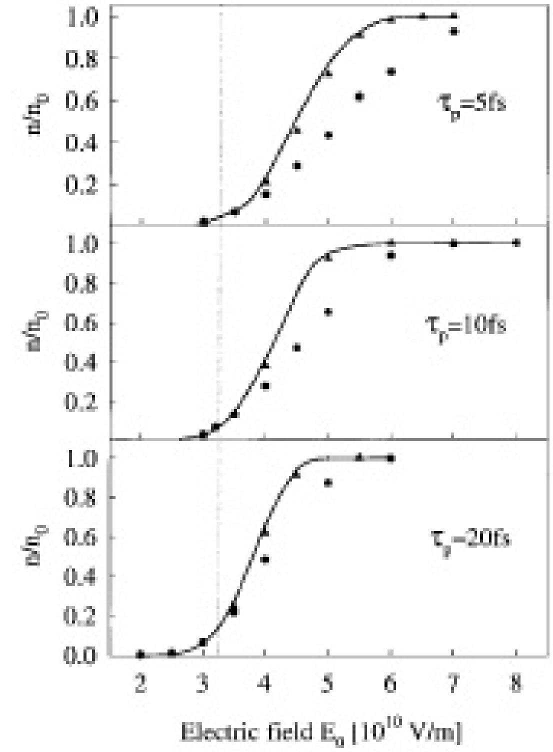

Figure 3.8: Fraction of ionized H in the BSI regime as a function of the peak electric field amplitude for pulses of 5, 10, and 20 fs in duration. Full line is ADK model, triangles show Krainov model, and circles show time-dependent Schroedinger equation. The dotted line is E_{bs} for H. From [71].

that the deviation is less than 5% when the Keldysh parameter is between $0.5 < \gamma < 2$ for 800 nm light. They conclude that the Keldysh condition which is calculated assuming tunnelling ionization is not the same as for the BSI regime.

In our experiments, we use an 18 fs duration pulse with a peak intensity of 1.3 x 10^{15} Wcm^{-2}. The peak electric field amplitude is $E_p = 2.3E_{bs}$ for argon; however, the peak field that the neutral argon atoms survive to will be somewhat less. From the calculations for He, the actual rate is about 80% what ADK theory predicts when the field is twice the barrier suppression field. Therefore the error in the ADK calculation of the total ionization fraction during the pulse should not be significant. For Ar+, the calculated ionization rate using the ADK model should be accurate, since we are below the barrier suppression intensity of the ion (2.4 x 10^{15} Wcm^{-2}) for our peak intensities. Previous work has shown very good agreement between experiment and theory using ADK ionization rates for ions.[81, 17] Therefore, it is valid to conclude that the significant extension of HHG we observe in Ar is due to emission from ions.

3.5 Plasma-induced Defocusing

We attribute our ability to observe these very high harmonic orders in argon primarily to the use of a waveguide for high harmonic generation.[50] The waveguide minimizes the effect of laser beam defocusing, resulting in high driving laser intensities even in the presence of a substantial plasma. Theoretical calculations[59] and experimental observation[2] show that plasma-induced defocusing effects limit the maximum intensity that can be achieved when a laser is focused into an ionizing gas. These effects become significant when the defocusing length, defined in Ref.[59] as $l_D = \lambda n_c/2n_e$, where n_e is the electron density and n_c is the critical density, is smaller than the confocal parameter. In effect, the spatially varying plasma creates a negative lens and the defocusing length is the length at which the phase advance at the center of the beam is $\pi/2$. Under the conditions in our experiment, 100% ionized gas at 7 Torr, the defocusing length is around 1 mm. This is an order of magnitude shorter than the laser beam confocal parameter of $\sim$ 1 cm, and indicates that without the waveguide, the ionizing gas would defocus the pulse before reaching its peak intensity. Experimentally, we observe that the transverse profile of the beam emerging from a 2.5 cm long waveguide is unaffected by the presence of the ionized gas for argon pressures up to 7 Torr, and that the energy decreases by 10-15%. This energy loss corresponds to a deposited energy of ~30 eV for each atom in the waveguide, and will lead to double-ionization of atoms in the center of the waveguide. We also observe a significant spectral broadening, blueshifting of around 20-50 nm, and a shorter pulse duration (from 22 fs to 18 fs) of the driving laser pulse when the gas is present, all of which are indicative of a strong laser-plasma interaction that would be enhanced with guiding. At the high laser intensities and ionization levels present in the waveguide, spectral broadening of the harmonic peaks can also occur, as seen in Fig. 3.3.

When the argon pressure is increased above 9 Torr, the output mode breaks up and harmonics are no longer observed. Therefore, there exists a limit to the amount of ionization-induced defocusing for which the waveguide can compensate. Experimentally, we observe that reducing the gas pressure in the waveguide will lead to an increase in the highest observed photon energy. Figure 3.9 shows HHG spectra for argon at 5 and 7 Torr in a straight waveguide. At the lower pressure, the flux at lower photon energies is reduced, but the higher photon energies are enhanced. Figure 3.10 shows a more dramatic result for harmonics from neon at the same intensity. There are several possible explanations for these results. It is possible that there is still some defocusing effect which increases with higher pressures, reducing the intensity. Also, at higher gas pressures, the laser energy at the output of the fiber is reduced, either from ionization or from other loss mechanisms in the waveguide. The reduction in laser energy and therefore intensity could also explain the decrease in harmonic energy.

The ability to generate harmonics in highly ionized media and from atomic ions holds great promise to advance the energy range and flux of soft x-ray sources from HHG. Previously, it was believed by many in the field that the limit to HHG energy was the saturation intensity. In this work, we demonstrate that the true limit is given by the cutoff rule. In Chapter 2, it was shown that the flux can be enhanced by using modulated waveguides even in 100 % ionization.

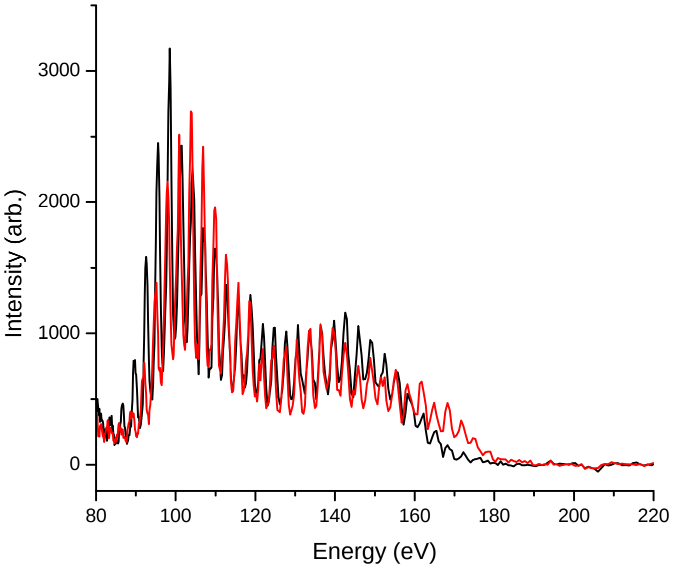

Figure 3.9: Measured harmonic spectra from a straight waveguide filled with argon at 5 Torr (red) and 7 Torr (black) for a pulse peak intensity of ∼ 9 x 10^{14} Wcm^{-2}. Both spectra taken with the SC grating and an exposure time of 300 s (using 0.4 μm thick Zr filters).

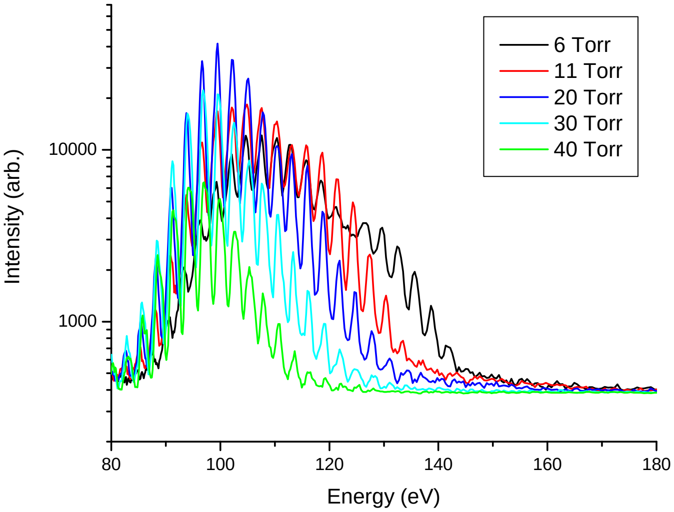

Figure 3.10: Harmonic spectra from a straight waveguide filled with Ne at different pressures for a peak laser intensity of ∼ 9 x 10^{14} Wcm^{-2}. All spectra taken with the SC grating and a 10 s exposure (using 0.4 μm thick Zr filters).

For the results shown in Fig. 3.3, the falloff in the emission at higher energies is likely due to the rapidly decreasing coherence length at higher levels of ionization, from ∼0.5 mm at 100 eV to ∼50 μm at 250 eV. Although a 0.25 mm modulated waveguide was used, the process was not optimally phase matched and further enhancement of the flux is expected by using shorter modulation periods and longer waveguide lengths.

Chapter 4

High Harmonic Generation Experimental Set-up

In this chapter, I discuss the experimental apparatus design and calibration used for the results of Chapters 2 and 3. The laser system was designed by Sterling Backus and was originally built by Sterling Backus and Randy Bartels. It is comprised of a 1 kHz two stage Ti:Sapphire amplifier system, shown schematically in Figure 4.1.[8] The output of a Ti:Sapphire oscillator is stretched to 200 ps using a grating stretcher, then passes through a zero length stretcher with a deformable mirror in the focal plane where the pulse is spectrally dispersed. The low energy pulse is then amplified in two stages to a final output pulse energy of 5 mJ, using 2 pump lasers on the 2nd stage. The amplified output is compressed in time with a grating compressor. The deformable mirror is used in conjunction with an Evolutionary Strategy algorithm to optimize the second harmonic signal, giving a final compressed pulse width of ∼22 fs +/- 2 fs. The loss from the grating compressor reduces the compressed signal to around 3 mJ.

The laser is focused with a 50 cm focal length mirror into a 150 μm inner-diameter hollow-core waveguide with a coupling efficiency of $\sim 60\%$.

Figure 4.2 shows the experimental setup for high harmonic generation. The laser is focused through a 250 μm-thick sapphire window and into the waveguide setup. The central, 2.5 cm fiber is held in a glass capillary with holes drilled in it to allow input of the gas, and there are two small fiber sections at each end which allow differential pumping to vacuum on either side. The harmonic signal and residual fundamental 800 nm light exit the waveguide into the rest of the vacuum chamber. A valve after the waveguide setup makes it possible to vent and change

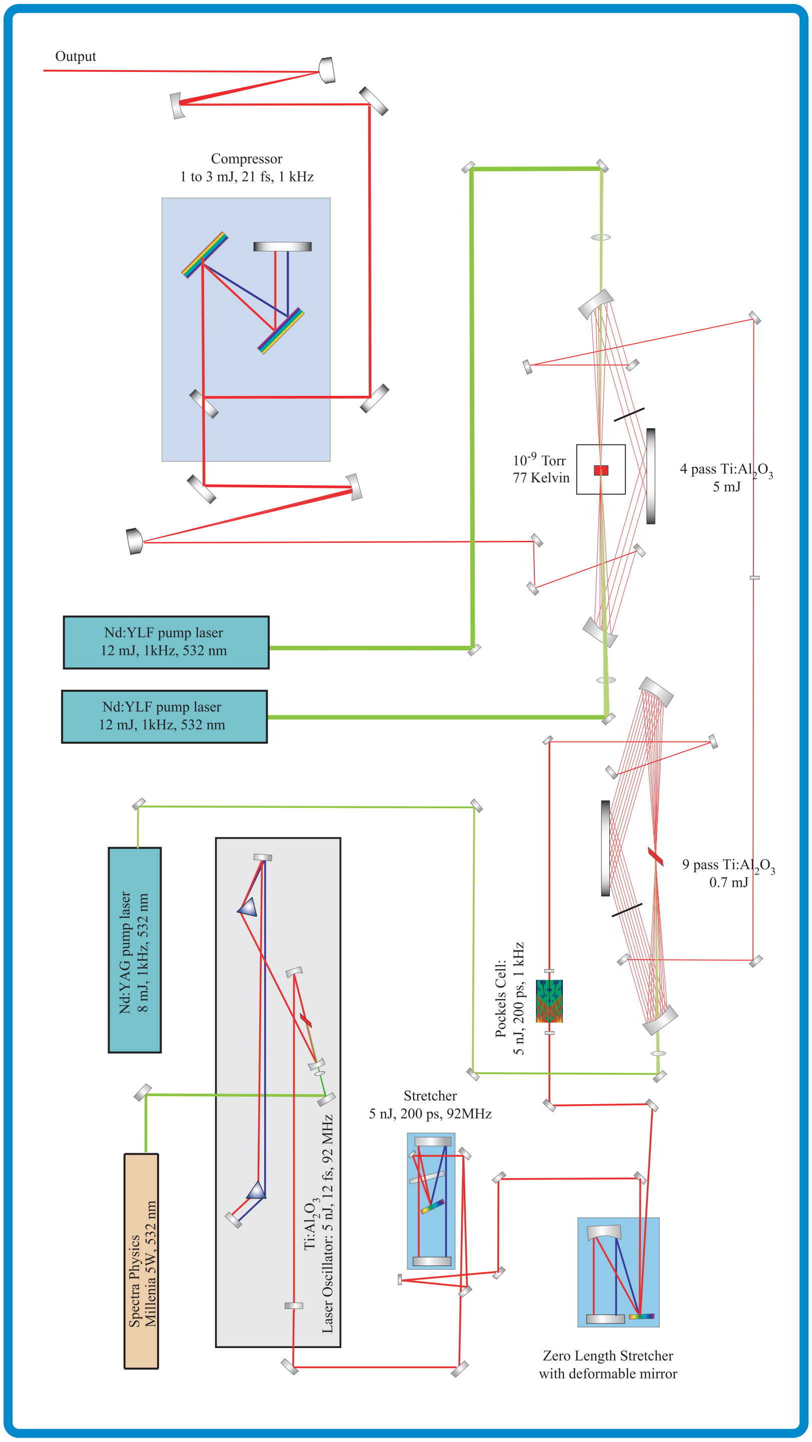

Figure 4.1: Schematic of Ti:Sapphire amplifier system used for high harmonic generation.

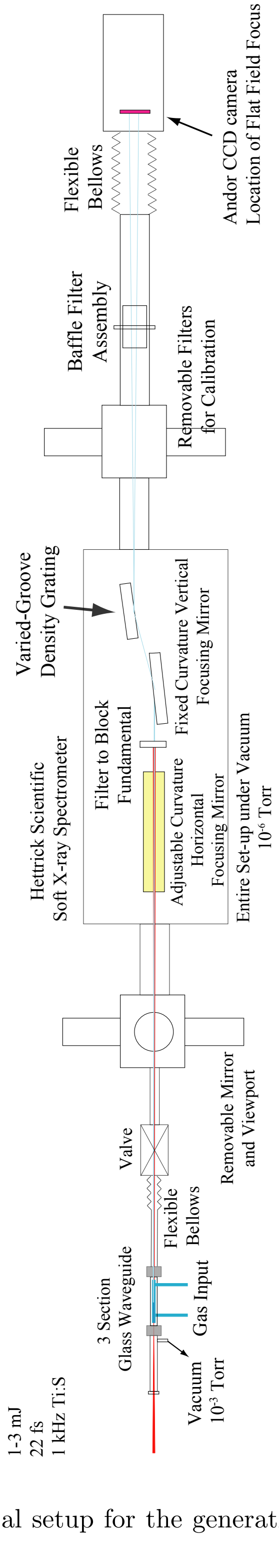

Figure 4.2: Schematic of experimental setup for the generation and measurement of high harmonics.

waveguides without venting the entire chamber. The harmonic light is focused and spectrally resolved with a grazing incidence soft X-ray spectrometer made by Hettrick Scientific, Inc. The spectrometer has vertical and horizontal focusing mirrors. The curvature of the horizontal mirror can be adjusted to remove any astigmatism at the focus on the CCD camera. The gratings have a varied groove density, allowing a flat field focus at the CCD.[35] The angle of the grating can be adjusted in vacuum to scan different wavelength ranges. A thin metal filter (Zr or Ag) is placed inside the spectrometer after the first curved mirror to block most of the fundamental light and pass the harmonic light. There is also a light-tight baffle with another thin metal filter after the spectrometer to eliminate any remaining fundamental light. A movable filter holder after the spectrometer allows insertion of different thin filters to calibrate the spectrum. The spectrum is measured using an Andor vacuum CCD camera.

4.1 Energy Calibration of High Harmonic Generation Spectra

Energy calibrations of the harmonic spectra were done using removable thin filters. The lower energy spectra were taken with grating SC which has 65 lines/mm. Calibrations were made with silicon and boron filters, which have sharp absorption edges at 99.9 eV and 188.35 eV respectively. Figure 4.3 shows the harmonic spectra taken with the two different filters. The higher energy spectra were taken with grating SB, which has 160 lines/mm, and calibrated using the boron and carbon edges at 188.35 eV and 284 eV, shown in figure 4.4. Both calibrations were done by a linear fit of the wavelength of the filter edges and the pixel numbers. However, this is only an approximation since the wavelength is not exactly linear with pixel spacing on the CCD camera. The grating equation describing the angle at which a given wavelength is dispersed is given by,

$$n\lambda = d(\cos\alpha - \cos\beta), \tag{4.1}$$

where n is the order, λ is the wavelength, d is the grating line spacing, and the angles α and β are the incident and reflected angles defined in figure 4.5. The angle β is related to the position on the CCD, x, by $x = r\tan\beta$, where r $\sim$ 80 cm is the distance between the center of the grating and the CCD array. The dispersion of the grating is then given by,

$$\frac{d\lambda}{dx} = \frac{d}{nr} \sin\beta \cos^2\beta. \tag{4.2}$$

Because the reflection angle β off the grating changes across the CCD array, the dispersion is not linear with x. Calibrations using the grating equation (Eqn. 4.1) and a two point linear fit are calculated to find out if the amount of error is significant. The Hettrick spectrometer is designed so that when zero order is centered at the output, the incident and reflected angle are both 2 degrees. As the grating angle is then adjusted so that the first order is centered on the CCD, $\alpha+\beta$=4 degrees still holds. It is necessary to know the wavelength at the center of the CCD to calculate α. The number of CCD pixels is 1024 along the dispersed axis, so that, in the case of the SC grating, the silicon edge is close to the center pixel, giving a value of $\alpha = 1.34$ degrees. Figure 4.6 plots wavelength and energy as a function of position x from the center of the CCD, using the grating equation and a two point linear fit. From these plots, it is evident that the linear calibration is off at the edges of the CCD array; however, for the wavelength region of interest in our experiments, the error is small. For the SB grating calibration, the

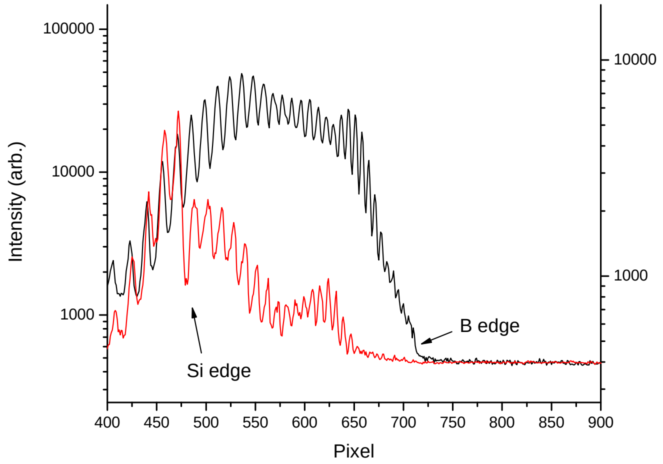

Figure 4.3: Harmonic spectra generated in neon using 0.2 μm-thick B (black) and 0.18 μm-thick Si (red) filters to calibrate the SC grating.

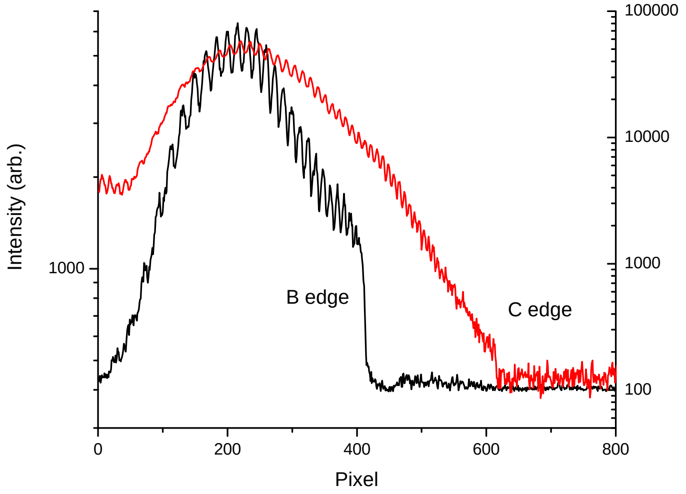

Figure 4.4: Harmonic spectra generated in neon using 0.2 μm-thick B (black) and C (red) filters to calibrate the SB grating.

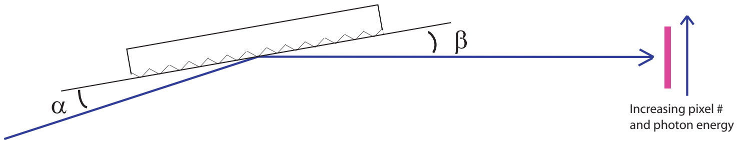

Figure 4.5: Schematic of grazing incidence grating and relevant angles.

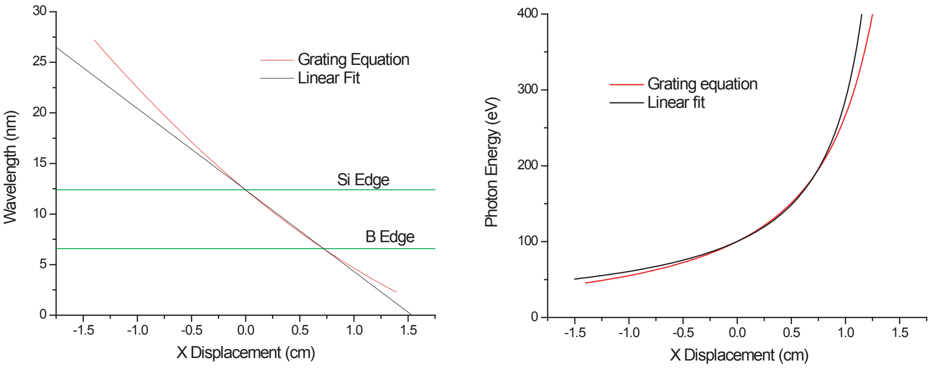

Figure 4.6: Wavelength and energy calibration of SC grating using the grating equation and a two point linear fit.

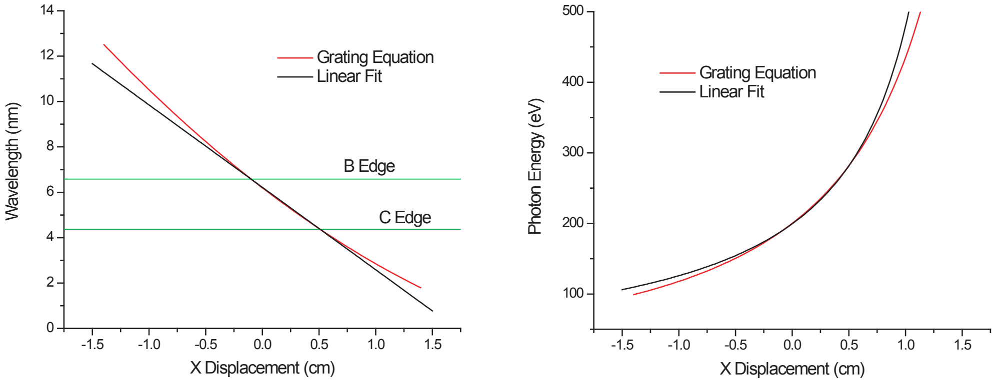

Figure 4.7: Wavelength and energy calibration of SB grating using the grating equation and a two point linear fit.

wavelength at the center is approximately 6.2 nm, so $\alpha = 1.19$ degrees. Figure 4.7 compares the wavelength and energy calibration using the grating equation and linear fit for the SB grating. Again, error in the linear fit is negligible for the energy range in our experiments.

4.2 Calculation of Photon Flux

An ultrafast soft X-ray source at the carbon edge is interesting for many applications such as biological microscopy or studying the dynamics of organic molecules. Many applications need a minimum amount of flux for reasonable data rates. To estimate the flux of our source, we consider the possible losses through the spectrometer and the detection. The harmonic light is reflected by two Au coated mirrors at an incident grazing angle of approximately 2 degrees. Figure 4.8 shows the reflectivity as a function of photon energy for one mirror. Surface roughness has a significant effect on the reflection efficiency at shorter wavelengths but in the best case, the reflectivity at 284 eV is 66%. The harmonic light is diffracted by the SB grating. The grating diffraction efficiency, measured at the Berkeley Advanced Light Source, is shown in Fig. 4.9 and is around 2% at 284 eV. The harmonic light passes through 0.4 μm of Ag to filter out the fundamental 800 nm light. The transmission of this thickness of Ag is 6% at 284 eV. Finally, the CCD detector has a quantum efficiency of roughly 40% at the carbon edge. The total efficiency is therefore at most 0.02%.

Figure 4.10 shows the baseline-subtracted harmonic spectra at the C edge. The highlighted data points are used to calculate the flux. There are 1108 counts in a 1% bandwidth at 283.3 eV for a 180 second exposure. When corrected for the efficiency of the spectrometer and filters, this gives 30,000 photons/s in a 1% bandwidth. This value is the absolute minimum since contamination of the filters and/or mirrors is likely and would reduce the measured signal. More precise calibration will be performed in the future using a soft X-ray mirror with a known reflectivity and bandwidth and detection either with a calibrated vacuum photodiode or CCD camera. It is useful to compare the flux at these extremely high orders with flux at lower harmonic orders. Previously, the flux of a broad range of harmonic orders centered at

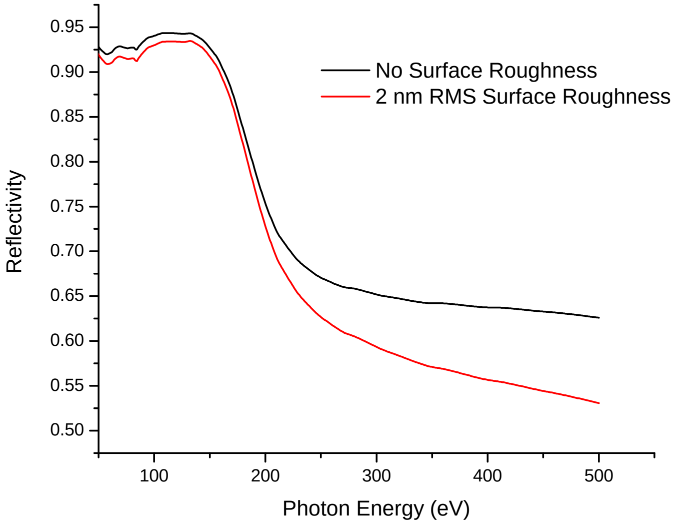

Figure 4.8: Reflectivity of a Au mirror at 2 degree grazing incidence angle for the ideal case, and for 2 nm RMS surface roughness.

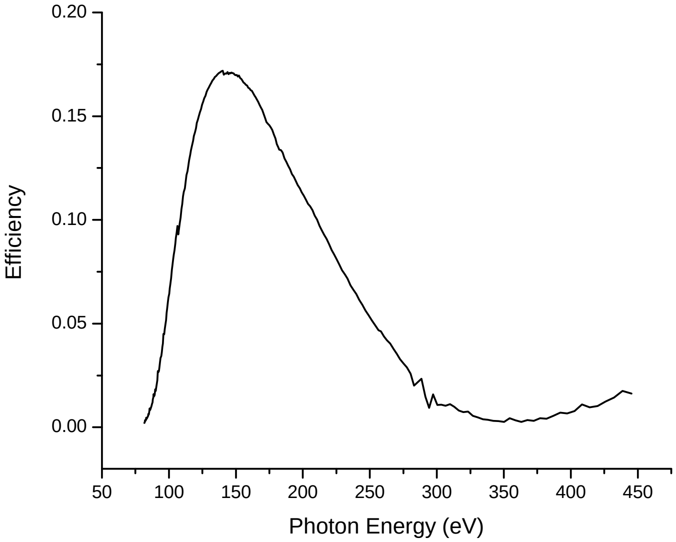

Figure 4.9: Measured efficiency of SB grating as a function of photon energy.

31 eV (harmonic orders 17-23) was measured using a vacuum photodiode.[10] The harmonics were generated with a 5 kHz repetition rate laser in argon using a 10 cm long hollow-core 150 μm inner-diameter waveguide. The measured flux was $\sim 2 \times 10^{12}$ photons/second. For further comparison, Fig. 4.11 shows the flux from the soft X-ray beamline at the Advanced Light Source at Berkeley. At the carbon edge, an estimated flux of 10^{13} photons/s in a 0.1% bandwidth is produced before the monochromator. Despite the higher photon flux of the Advanced Light Source, the pulse duration much greater than that of the soft x-ray light produced from HHG.

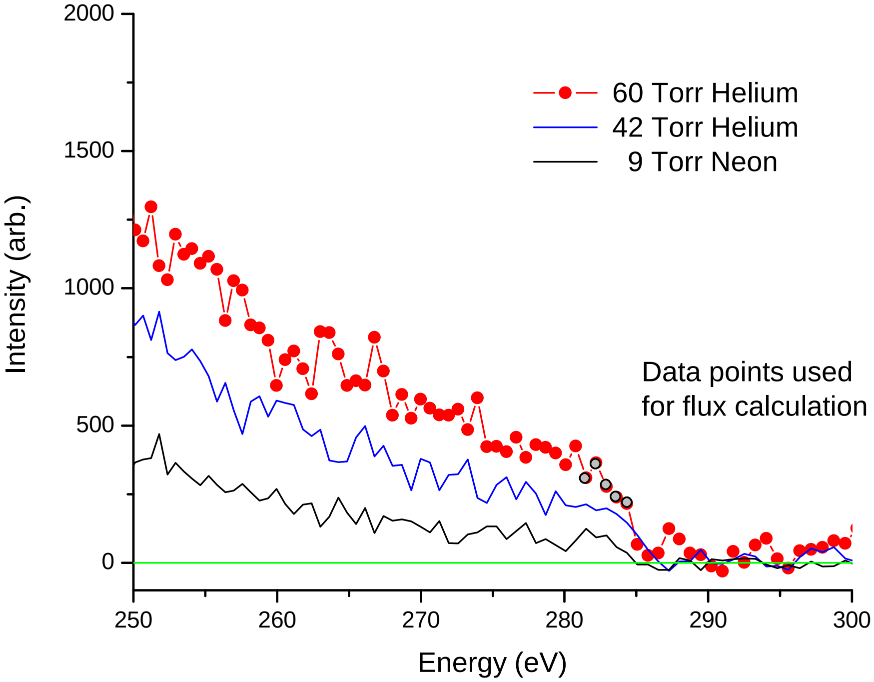

Figure 4.10: Harmonic spectra at the carbon edge showing the data points used to estimate the photon flux.

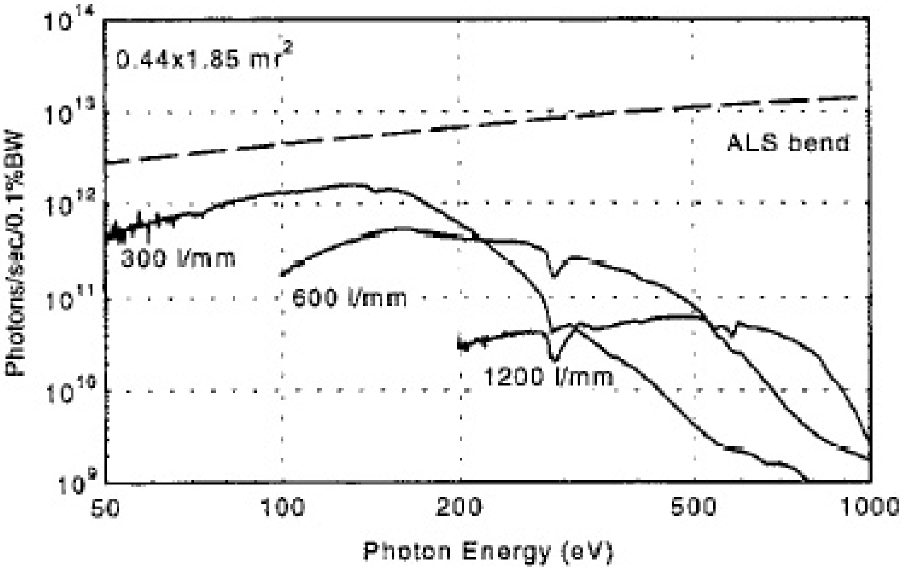

Figure 4.11: Measured flux from the ALS beamline 6.1 and estimated flux assuming 100% efficient optics (dashed line). From [76].

Chapter 5

Self-compression of Intense Femtosecond Pulses in Gas-filled Hollow-core Waveguides

One surprising experimental result that came out of my research on high harmonic generation was the observation of temporal compression of the 800 nm driving pulse after propagating in a hollow-core waveguide filled with low-pressure argon at ionizing intensities. Unlike other standard pulse compression techniques, no subsequent dispersion compensation was used. Typically, pulse compression is accomplished by broadening of the spectrum of the pulse through nonlinear self-phase modulation. This broadened pulse bandwidth can then be compressed to a shorter pulse by appropriate dispersion compensation. Self-phase modulation of the pulse can be done by propagation through an optical fiber[53, 73] or a gas-filled hollow waveguide[54] at non-ionizing intensities and dispersion compensation is provided by prisms, gratings, or chirped mirrors to create a negative group velocity dispersion. These schemes have been employed to compress pulses to under 4 fs pulse duration[82]; however, such techniques are lossy and can be quite complicated. Furthermore, all previous pulse compression schemes have been limited to sub-millijoule pulse energies due to the damage threshold of the fibers or ionization of the gas. The use of ionization to broaden the spectrum of a pulse for compression has been previously considered theoretically.[72] However, the compression also depended on negative group velocity dispersion compensation.

5.1 Experimental Results

In the experiment, light from a Ti:sapphire amplifier producing $\sim$ 30 fs near-transform limited pulses with 2.5 mJ pulse energies at 1 kHz was focused into a 2.5 cm long, 150 micron inner-diameter hollow waveguide filled with low pressure argon. The spot diameter of the laser mode at the entrance of the waveguide was $\sim$ 85 μm FWHM and the energy throughput of the waveguide was $\sim$ 60% with no gas. The focusing region before and after the waveguide was held under vacuum to prevent any additional nonlinear effects. The pulse was characterized before and after the waveguide using second-harmonic frequency-resolved-optical-gating (SHG-FROG).[74] All FROG measurements were deconvolved using commercial software from Femtosoft Technologies (FROG Version 3.03) to an error of $< 1\%$ for a 256x256 sampling grid. The spectral marginals for each measurement agree with the experimentally measured spectra to within 5%. After exiting the waveguide, the pulse passes through a 250 μm thick sapphire window and a 1 mm thick fused silica beam splitter in the FROG setup. The total dispersion of these elements corresponds to a group velocity dispersion of 61 fs^2 and a third-order dispersion of 40 fs^3 at a center wavelength of 760 nm, which would change the pulse duration at most by 3 fs, not enough to significantly affect the experimental results. Also, the material gives a positive group velocity dispersion, which would not explain pulse compression by the typical schemes. The pulse shape after the fiber without gas is the same as the input to within our measurement resolution.

The intensity in the waveguide, approximately 10^{15} W/cm^2, is high enough to completely doubly ionize the argon gas by the peak of the pulse (for a 30 fs duration pulse). This rapidly changing ionization during the pulse results in an index of refraction that decreases with time, causing a blue shift of the overall laser spectrum. The spectra at the exit of the waveguide with varying pressures of argon is shown in figure 5.1. Pressures as low as 1 Torr result in significant blue shift and spectral broadening and blue shifts of up to $\sim$ 50 nm are observed. Figure 5.2 shows the deconvolved FROG measurements of the temporal pulse shape after the waveguide

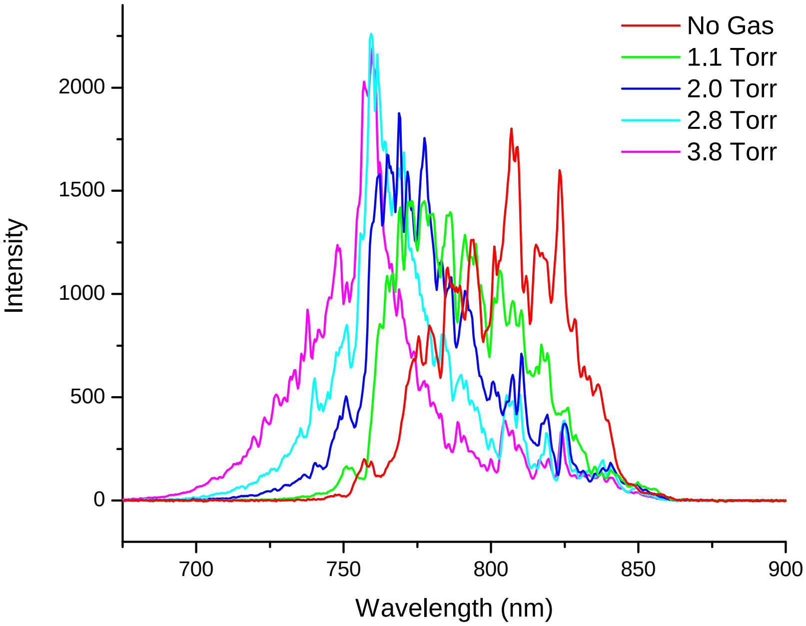

Figure 5.1: Spectra taken after the 2.5 cm long, 150 μm diameter waveguide with different Ar pressures.

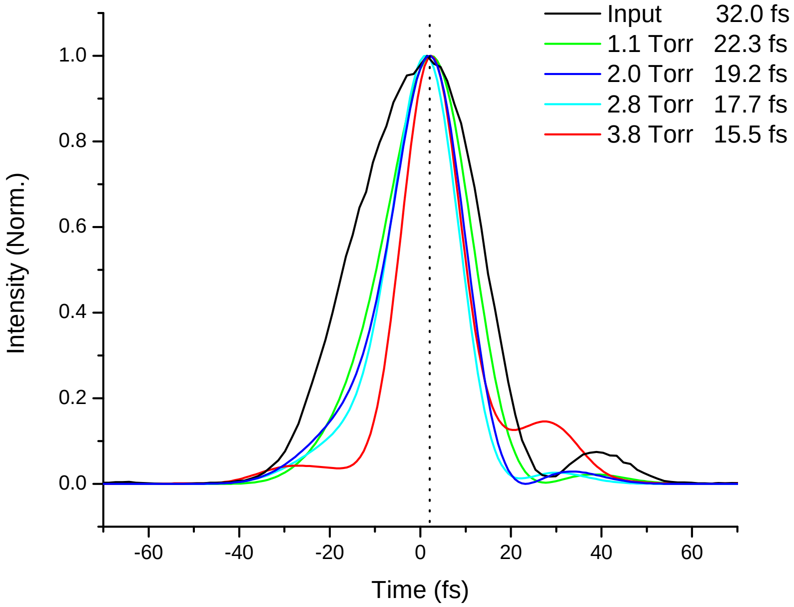

Figure 5.2: Deconvolved FROG measurements of the temporal pulse shape before and after the waveguide with different Ar pressures for an initial pulse of 32 fs. The pulse FWHM for the different measurements are indicated.

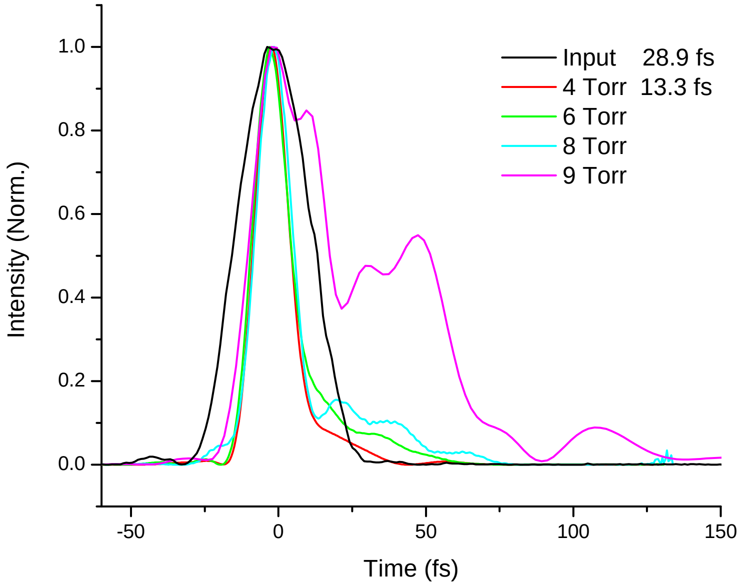

Figure 5.3: Deconvolved FROG measurements of the temporal pulse shape before and after the waveguide with different Ar pressures for an initial pulse of 29 fs. At 4 Torr, the final pulse duration is 13.3 fs FWHM. From [78].

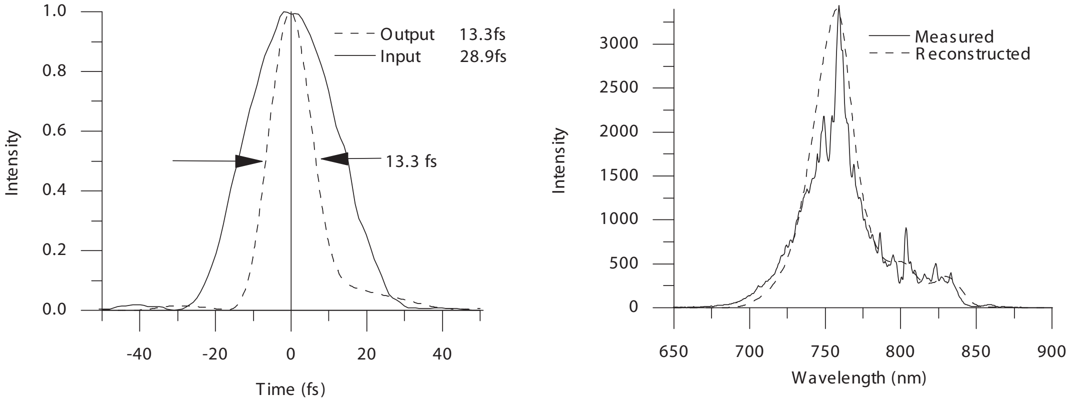

Figure 5.4: Comparison of the measured spectrum with the spectrum from FROG measurement deconvolution.

for different argon pressures. With only 1 Torr of argon, the initial pulse width of 32 fs has been drastically reduced. As the pressure is increased, the pulse width decreases to 15.5 fs at 4 Torr. Figure 5.3 shows the results for an input pulse of 29 fs duration. At 4 Torr, the final measured pulse duration is 13.3 fs. As the pressure is increased, the pulse duration remains relatively constant until 9 Torr, at which point the pulse begins to break up. The deconvolved spectrum from the FROG and the experimentally measured spectrum are shown in figure 5.4 for the 13.3 fs pulse. The excellent agreement between the two indicates that the measurement has high accuracy and is self-consistent. The spectral bandwidth can support an 11 fs transform-limited pulse. Both the input and compressed pulses are near-transform limited, within 20% of the time-bandwidth product. The power exiting the waveguide is reduced by ~ 5 % with 4 Torr of Ar compared with no gas in the waveguide, while at 8 Torr, the loss is 10%. Also, the spatial mode after the waveguide remains good at low gas pressures. Using a larger diameter, 230 μm waveguide, the pulse is only compressed to 24 fs from a 30 fs duration input. When the waveguide is replaced with a 1 cm diameter gas-filled cell, there is negligible compression of the pulse.

5.2 A New Mechanism for Pulse Compression

Conventional 1-D pulse propagation models[1, 13] such as those used to calculate self-phase modulation in optical fibers, microstructured fibers, or gas-filled hollow waveguides, fail to explain the experimental self-compression observed. The blue-shift and broadening of the spectrum can be explained by self-phase modulation from the changing plasma index; however, this will not alter the temporal envelope. The dispersion of the low-pressure gas, the plasma, or the waveguide is too small to affect the temporal shape as well. Higher-order nonlinear effects can cause self-steepening of the pulse which can reshape the trailing edge, but will not shorten the pulse in time.

Table 5.2 summarizes the potential 1-D pulse shaping mechanisms and the characteristic propagation length over which they become significant for our conditions.[13] The dispersion length is given by:

$$L_{dis} = \frac{T^2}{|\frac{d^2k}{d\omega^2}|}, \tag{5.1}$$

where T is the pulse duration (1/e intensity) and $k = \omega n/c$. For a 30 fs pulse FWHM, $T =$ 18 fs. The dispersion length is the length over which the pulse duration would approximately double due to group velocity dispersion (GVD). Self-phase modulation becomes important when the spectral broadening is on the order of the spectral width of the initial pulse. The amount of SPM broadening is given approximately by $d\phi(\omega)/dt$ or $\sim \Delta\phi_{NL}/T$ where $\Delta\phi_{NL} \sim n_2 I\omega L/c$. The bandwidth of the input pulse is approximately $1/T$. Therefore, SPM is significant when $\Delta\phi_{NL} \sim 1$ and the effective length is given by:

$$L_{SPM} = \frac{c}{\omega n_2 I}. \tag{5.2}$$

Another nonlinear mechanism is self-steepening of the pulse. The self-steepening process depends on the nonlinear group index which is defined as $n_2^{(g)} = n_2 + \omega\frac{dn_2}{d\omega}$. In our case, the assumption $n_2^{(g)} \approx n_2$ is valid. The effective length over which self steepening is significant is given by:

$$L_{SS} = \frac{cT}{n_2^{(g)} I}. \tag{5.3}$$

Lastly, the time-varying index due to ionization during the pulse also affects the pulse spectrum. The plasma index is given by:

$$n_p = \sqrt{1 - \frac{\omega_p^2}{\omega^2}} \simeq 1 - \frac{\omega_p^2}{2\omega^2}, \tag{5.4}$$

where ω_p is the plasma frequency given by: $\omega_p^2 = N_e e^2/m\epsilon_0$, e and m are the electron charge and mass, and N_e is the electron density. Because the electron density is increasing in time during the leading part of the pulse, the plasma index is also changing during the pulse. In this way, the plasma index acts like the nonlinear index, $n_2 I$, the difference being that it only decreases during the pulse, instead of increasing and decreasing over the duration of the pulse. Therefore, the spectrum predominately broadens to shorter wavelengths. The length over which the effective nonlinear index from the plasma will affect the spectrum from self-phase modulation is given by $L_{PlasmaSPM} = c/\omega n_p$ and the effective self-steepening length given by $L_{PlasmaSS} = cT/n_p$.

Mechanism	Length scale	Distance
Waveguide GVD	$L = \frac{T^2 a^2 \omega^3}{u_{11}^2 c}$	14 m
Gas GVD	$L = \frac{T^2 2\pi c^2}{\lambda^3 \frac{d^2 n}{d\lambda^2}}$	1.5 km
Plasma GVD	$L = \frac{T^2 c \omega^3}{\omega_p^2}$	1.4 m
Gas SPM	$L = \frac{c}{\omega n_2 I}$	10 cm
Gas self-steepening	$L = \frac{cT}{n_2^{(g)} I}$	4 m
Plasma SPM	$L = \frac{2\omega c}{\omega_p^2}$	2 mm
Plasma self-steepening	$L = \frac{2Tc\omega^2}{\omega_p^2}$	1 cm
Plasma defocusing	$L = \frac{1}{2} k \omega^2 = \frac{2\omega c}{\omega_p^2}$	1.5 mm

Table 5.1: Table of possible pulse shaping mechanisms that involve only 1-D propagation effects and the propagation length over which they become significant. The conditions used in the calculation are 4 Torr of Ar in a 150 μm diameter hollow waveguide. The gas terms were calculated for no ionization, and the plasma terms were calculated for 200 % ionization.

A 1-D propagation model was performed by Tempea et al.[72] for similar conditions: pulse intensities of 7 x 10^{14} to 1.5 x 10^{15} W/cm^2, 125 μm inner-diameter hollow waveguide, 20 fs input pulse, and argon pressure of $\sim$ 0.5 Torr. They found significant spectral broadening to shorter wavelengths for long propagation lengths (90 cm) with a positive chirp on the output pulse, but did not observe any temporal compression from their model.

Since 1-D nonlinear wave propagation cannot explain our experimental observations and because the waveguide is necessary to achieve pulse compression, a 3-D propagation model was employed. Propagation of the laser pulse in the waveguide was modelled by numerical solution of the 3-D scalar wave equation. This model was developed by Ivan Christov and is described in more detail in Ref. [18]. The model takes into account the dispersion from the transient plasma, power dissipation from ionization, and dispersion due to the neutral gas at each radial position in the waveguide as a function of time. The 3-D diffraction by the waveguide is included and automatically accounts for the waveguide dispersion. The waveguide loss was also measured experimentally and incorporated into the model.

The theoretically predicted pulse durations and spectra as a function of pressure are shown in Figs. 5.5 and 5.6. The model is in excellent agreement with experimental data, predicting that the pulse undergoes temporal reshaping that reduces the pulse width from 30 fs to approximately 13 fs with increasing pressure, and that the minimum pulse duration is obtained around 4 Torr. The leading edge of the pulse also steepens in time, accompanied by a longer trailing edge that develops a shoulder as the pressure is increased - again in very good agreement with experiment. The model also predicts less compression for larger diameter waveguides and little or none for the case of no waveguide, as is the case experimentally. Finally, the corresponding pulse spectra blue shift and increase in bandwidth due to the combined effects of rapidly changing plasma index and self-phase modulation are also in good agreement with experiment. At high pressures above 8 Torr, the pulse splits and the spectrum develops a large long-wavelength wing, also observed experimentally. The only adjusted parameter in the calculations to obtain agreement was the input diameter of the focused laser mode into the

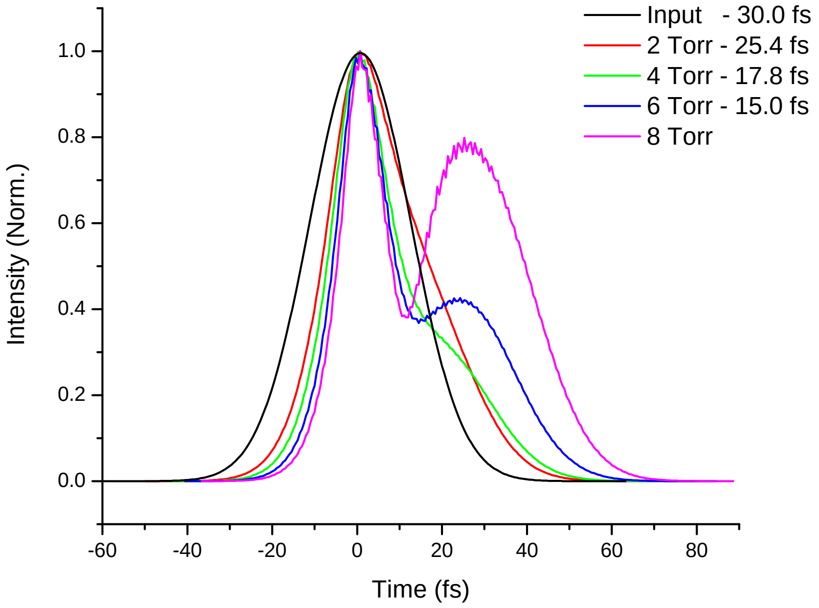

Figure 5.5: Theoretical calculation of temporal pulse shape after the waveguide with different Ar pressures for an initial pulse duration of 30 fs using the 3-D propagation model. The pulse FWHM are indicated.

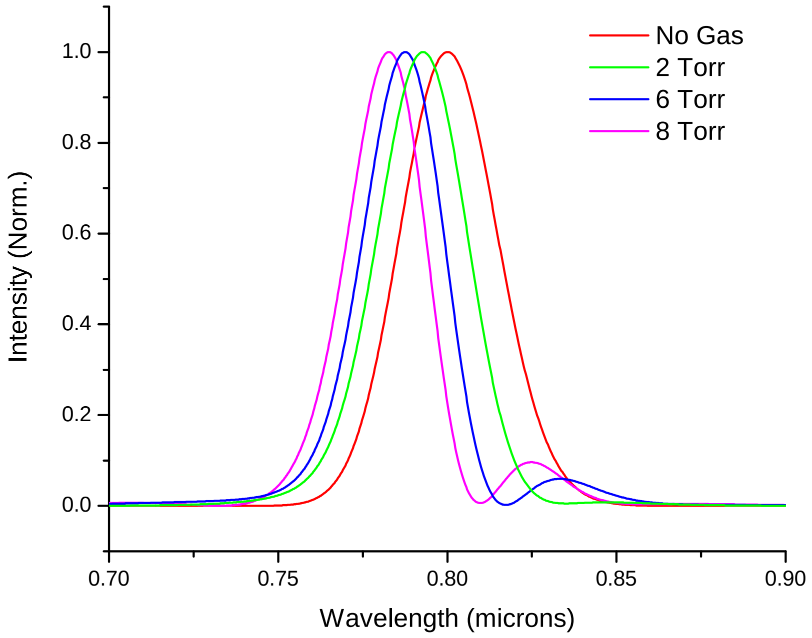

Figure 5.6: Theoretical calculation of the pulse spectrum before and after the waveguide with different Ar pressures.

waveguide.

The self-compression is a result of the combined effects of plasma-induced refraction and blue shifting, diffraction of the laser beam, phase modulation due to the rapidly-changing plasma index, and guiding by the hollow waveguide. The role of plasma defocusing combined with the waveguide refocusing governs the spatial propagation and is very important in the compression process. The model shows that as the pulse begins to ionize the gas, the trailing edge of the pulse refracts from the center of the waveguide due to plasma-induced defocusing. However, this portion of the beam is then reflected back into the guide by the waveguide walls. This leads to a temporally compressed pulse with a sharp leading edge and flat temporal phase. The reshaping also leads to a small periodic oscillation in the beam diameter and pulsewidth as the pulse propagates down the waveguide. This high-field pulse reshaping process has similarities with passive mode locking of lasers using saturable absorbers - the trailing edge of the pulse is slowly depleted periodically along the waveguide due to ionization-induced defocusing, where the role of a laser resonator is replaced by the waveguide. Both experimentally and theoretically, the pulse compression process is sensitive to the initial mode coupled into the waveguide. Also, theoretically, the laser beam must be focused to a tighter focal spot diameter than the ideal 100 μm for coupling into the lowest-order mode of 150 μm waveguide, in agreement with our experimental observations.

A new mechanism for pulse compression that operates at laser intensities above the ionization threshold has been demonstrated both theoretically and experimentally. This technique allows compression of pulses with millijoule energies and has the advantage of minimal distortion of the laser mode, low power loss, and no need for additional dispersion compensation. It is likely to scale to higher intensities and pulse energies, making it useful for high-field science and applications.

Chapter 6

Spectral and Temporal Characterization of High Harmonic Generation by Photoelectron Spectroscopy

In this chapter, I discuss the design and development of a simple in-line apparatus to measure the spectral and temporal characteristics of high harmonic generation. The apparatus can be used in front of an experiment without disrupting the HHG beam. The spectrum is measured by detecting photoelectrons emitted as a result of ionization of a noble gas by the extreme-ultraviolet (EUV) light. The photoelectrons are energy analyzed using a compact magnetic-bottle time-of-flight spectrometer. The spectrum can be reconstructed from the known ionization potential and absorption of the detection gas. The time duration of the EUV pulse is measured by cross-correlation with a portion of the driving laser pulse.

6.1 A Compact Magnetic Bottle Photoelectron Spectrometer

The magnetic bottle time-of-flight (TOF) apparatus is designed to collect and energy analyze photoelectrons emitted over initial trajectories within a 2π solid angle. The increased collection efficiency is necessary to measure the photoelectron spectrum from ionization of a gas by high harmonics where the signal level is typically 2-3 electrons per laser shot. The detection region has a strong magnetic field aligned along the TOF axis. The field is then reduced to a lower, constant value in the time-of-flight region. In this way, electrons generated in the detection region undergo cyclotron motion and follow the magnetic field lines to the detector. As they pass from the high field to the low field region, their velocities are parallelized so that

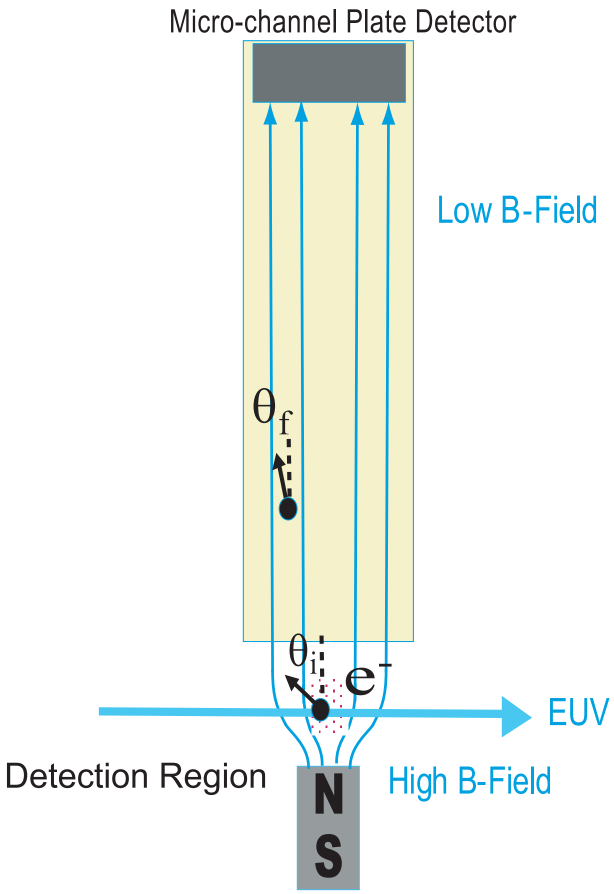

Figure 6.1: Diagram of magnetic bottle showing direction of field lines and electron trajectories.

even electrons initially travelling in a direction away from the flight tube end up with most of their velocity redirected along axis. A schematic of the apparatus indicating the magnetic field is given in Figure 6.1.

The theory of operation of the spectrometer is described in detail by P. Kruit and F. H. Read.[43] The initial angular momentum of the electron is given by

$$\ell = m^2 v^2 \sin^2 \theta_i / eB_i, \tag{6.1}$$

where m, v, and e are the mass, velocity, and charge of the electron, θ_i is the initial angle of the velocity with respect to the time-of-flight axis, and B_i is the initial, strong magnetic field. From conservation of angular momentum, the final velocity angle of the electron, θ_f, in the lower magnetic field, B_f, is given by the relation

$$\frac{\sin\theta_f}{\sin\theta_i} = (\frac{B_f}{B_i})^{1/2}. \tag{6.2}$$

If the difference between the initial and final fields is large enough, the final velocity direction will be along the TOF axis for a range of different initial angles. For example, if $B_f/B_i = 10^{-3}$, then for the maximum initial angle, $\theta_i = 90$ degrees, the final angle is given by, $\theta_f = \sin^{-1}(B_f/B_i)^{1/2} = 1.8$ degrees. It is important to have a large difference in the initial and final field so that electrons with the same initial velocity will have the same drift time in the TOF tube. Also, for the best energy resolution, it is important for the changing-field region to be as short as possible while remaining in the adiabatic limit. The adiabaticity parameter is defined by

$$\chi = \frac{2\pi m v}{eB_z^2} |\frac{dB_z}{dz}|, \tag{6.3}$$

which is the fractional change in the field that the electron experiences in one cyclotron orbit.

The design of the spectrometer is shown in Figure 6.2. The spectrometer consists of a stack of permanent magnets to generate the strong field in the detection region and a flight tube with a solenoid constructed around it to create a uniform lower field. A cone with a 2 mm diameter aperture is located before the entrance to the time-of-flight tube to allow differential

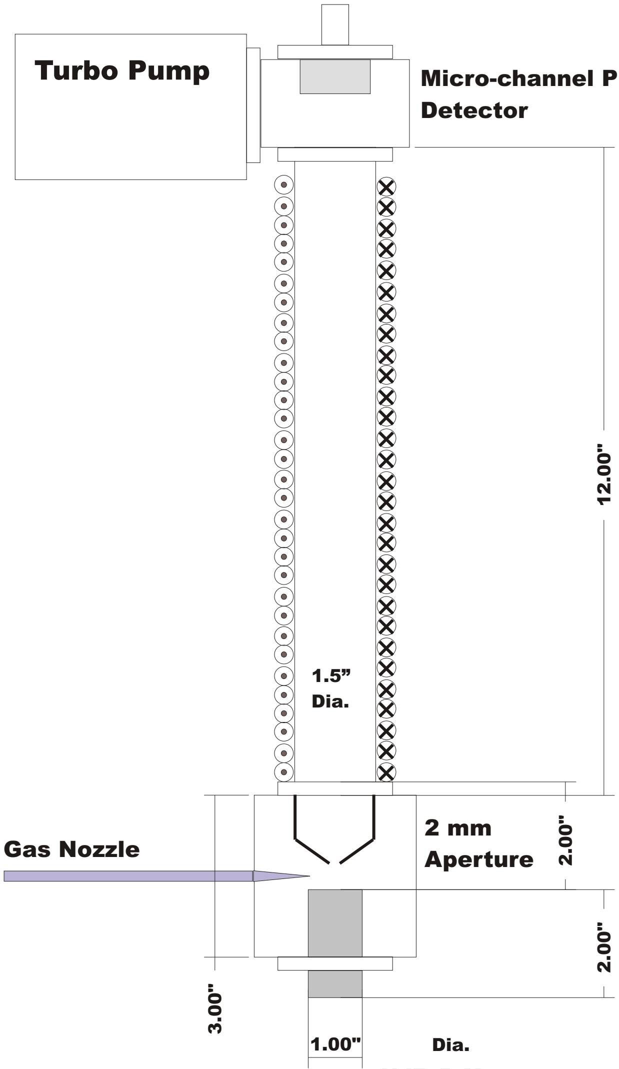

Figure 6.2: Schematic of compact magnetic bottle time-of-flight spectrometer. Dimensions are indicated.

pumping and to limit the detection region. At the top of the TOF is a micro-channel plate (MCP) detector and a 60 L/s turbo pump which evacuates the TOF region to a pressure of 10^{-6} Torr. A 3 cm long, 150 μm inner-diameter hollow-core glass fiber is used as a gas nozzle to continuously leak gas into the detection region. Another 60 L/s turbo pump is attached adjacent to the detection chamber so that the pressure in the detection region does not reach above $\sim 10^{-4}$ Torr with the nozzle on. All of the surfaces in the detection region and TOF tube are coated with conductive carbon powder to eliminate any charge buildup effects. Also, care was taken to ensure that all parts were constructed with aluminum or non-magnetic stainless steel. The MCP detector design is given in Appendix C. The current signal from the detector is amplified by a 1 GHz Amplifier and Timing Discriminator (EG&G Ortec Model 9327) and then recorded by a timing board on a PC (ACAM Time Measuring Device Model AM-F1, manufactured by Acam-messelectronic gmbh Karlsruhe, Germany). The start signal is taken from an SRS Delay Generator which also provides the trigger for the Pockels cell of the amplifier. The true start time is obtained by direct detection of scattered photons from the driving laser, producing a current signal from the MCP detector.

To aid in the design of the spectrometer, the total magnetic field was modelled. The magnetic field of the permanent magnets are calculated using the equation for the magnetic scalar potential,[36]

$$\Phi_M(\mathbf{x}) = \frac{1}{4\pi}\oint_S \frac{\mathbf{n}' \cdot \mathbf{M}(\mathbf{x}')da'}{|\mathbf{x}-\mathbf{x}'|}. \tag{6.4}$$

The surface integral is evaluated over the top and bottom faces of the magnet. The value of the magnetization, **M**, was found by fitting the experimentally measured value of the field on axis at several distances from the magnet face, shown in figure 6.3. The magnetic field of the solenoid was calculated using the equation for the magnetic field of a current loop, given in reference [45], p.112. The solenoid field is then the sum of all the loop fields. The solenoid parameters are loop radius of 2.05 cm, current of 1 A, and 9 loops/cm with a total length of 30 cm. The solenoid starts 5 cm above the top face of the permanent magnet. The code used for the calculation is given in Appendix B. Figure 6.4 shows the total magnetic field on axis due to

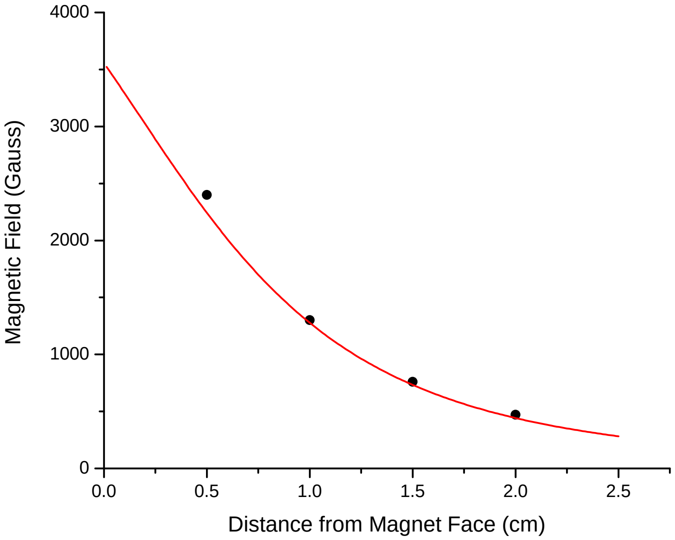

Figure 6.3: Measured values of the magnetic field on axis above a 1 inch dia., 0.5 inch thick, NdFeB magnet (black dots). Theoretical prediction of magnetic field for a magnet with a magnetization of 8000 A/m (red line).

both the permanent magnet and the solenoid. The decrease at around 32 cm is due to fringing at the end of the solenoid.

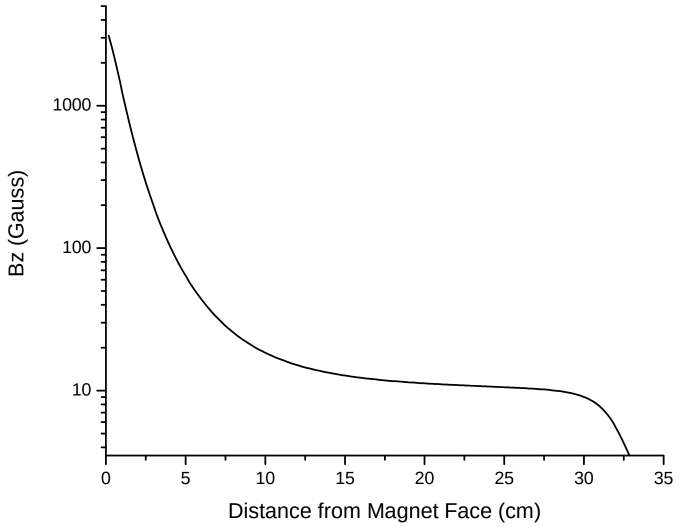

Figure 6.4: Calculated z component of the magnetic field from the permanent magnet and solenoid on axis.

Figure 6.5 plots the adiabatic parameter, calculated using Eqn. 6.3, as a function of length on axis for 1 eV electrons. For higher energy electrons, the parameter scales as $\sqrt{E}$. The adiabatic parameter is still less than one, even for electrons with energies as high as 30 eV. For comparison, Figure 6.6 shows the magnetic field on axis and the adiabatic parameter for the magnetic bottle spectrometer design by Kruit and Read. In their design, the changing-field region is shorter, which can give an improved energy resolution. This is achieved by a more complicated water-cooled electromagnet to generate the strong field. Other magnetic bottle designs use specially designed pole pieces with permanent magnets to achieve similar field profiles.[75]

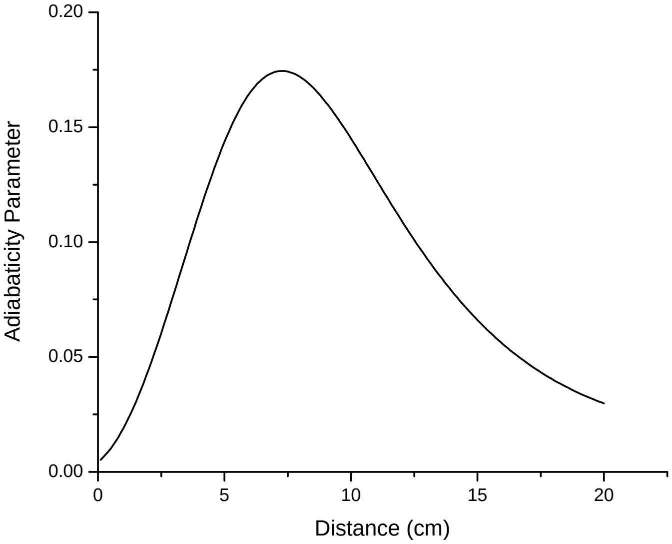

Figure 6.5: Calculated adiabatic parameter on axis, for 1 eV electrons.

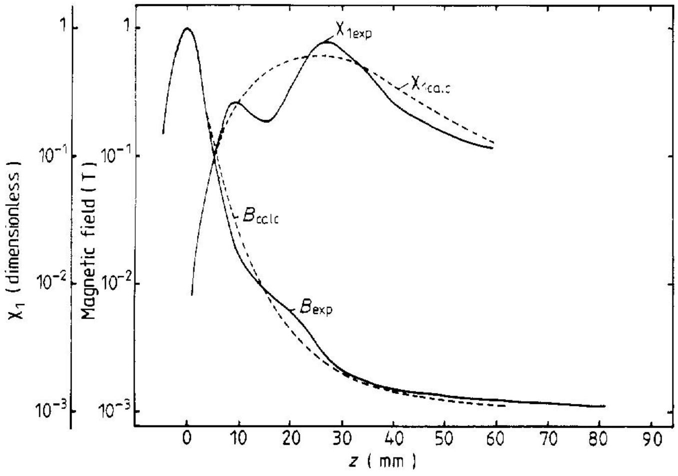

Figure 6.6: Calculated (dashed) and measured (solid) magnetic field and adiabatic parameter for 1 eV electrons on axis. From [43].

6.2 Experimental Results

Despite its simple design, the compact magnetic bottle spectrometer has good resolution over a broad range of electron energies. Figure 6.7 shows a typical spectrum from ionization of Ar and Ne gas by high harmonic EUV emission. The high harmonics are generated in a 2.5 cm-long, 150 μm inner-diameter hollow waveguide filled with Ar. The driving laser pulse energy is $\sim$ 0.7 mJ and pulse duration is 22 fs. A typical spectrum can be acquired in 60 seconds with a data rate of 2000-3000 counts/s. The photon energy is calculated by taking the photoelectron energy and adding the ionization potential of the detection gas. The difference in the spectra using Ar and Ne as the detection gas is due to the difference in their absorption spectra, shown in Figure 6.8. Therefore, to get an idea of the actual photon spectrum, the photoelectron spectrum must also be corrected for the energy dependent absorption. From figure 6.7, it is apparent that the magnetic bottle is able to resolve harmonic peaks over a broad energy region. However, there is a background for the lower energy photoelectrons ranging from 0 to $\sim$8 eV.

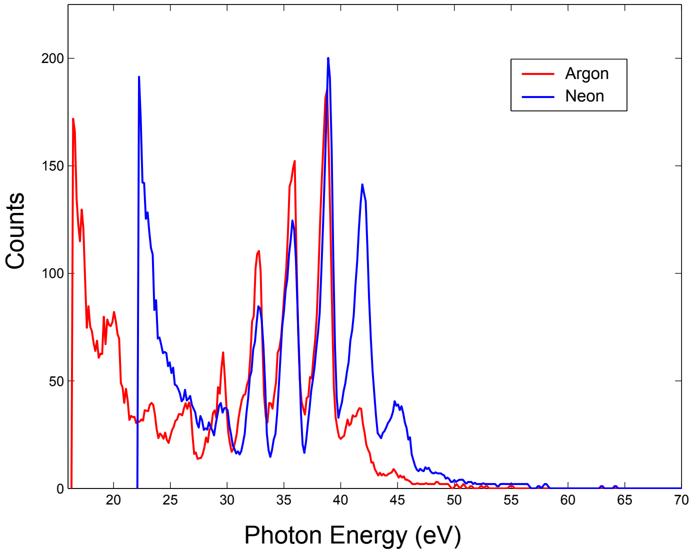

Figure 6.7: High harmonic spectrum measured by the magnetic-bottle photoelectron spectrometer using different detection gases.

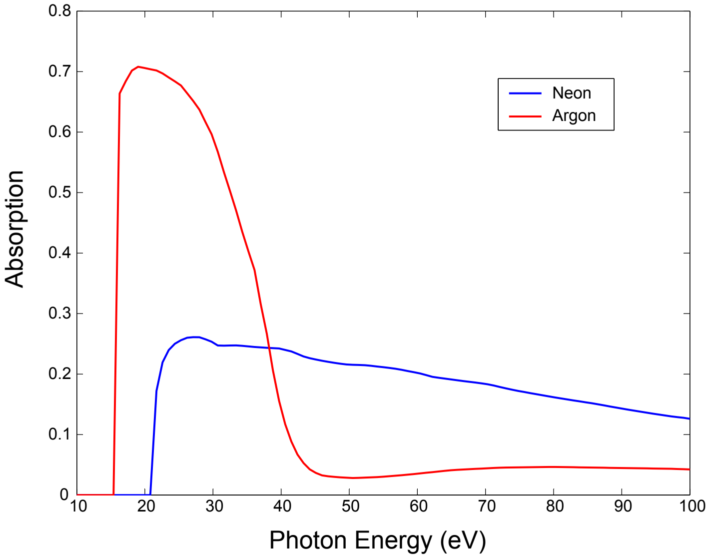

Figure 6.8: Absorption at different photon energies for argon and neon gas. From CXRO website.

At higher photon energies, the magnetic bottle spectrometer also performs well. Figure 6.9 shows high harmonic generation from a hollow-core waveguide filled with Ne at higher driving laser intensities (∼ 1 mJ and 22 fs) measured by detecting photoelectrons from Ne gas. The photon energy extends up to ∼ 100 eV. In addition, the photon spectrum was measured at the same time by a Hettrick EUV spectrometer, which uses a grating and CCD camera. Figure 6.10 compares the spectra taken with the two different spectrometers. The resolution of the Hettrick spectrometer should be almost constant over the region of the spectrum. The magnetic bottle resolution appears to decrease at lower photoelectron energies. Because the spectral width of the harmonics is unknown, it is difficult to give an exact value for the resolution.

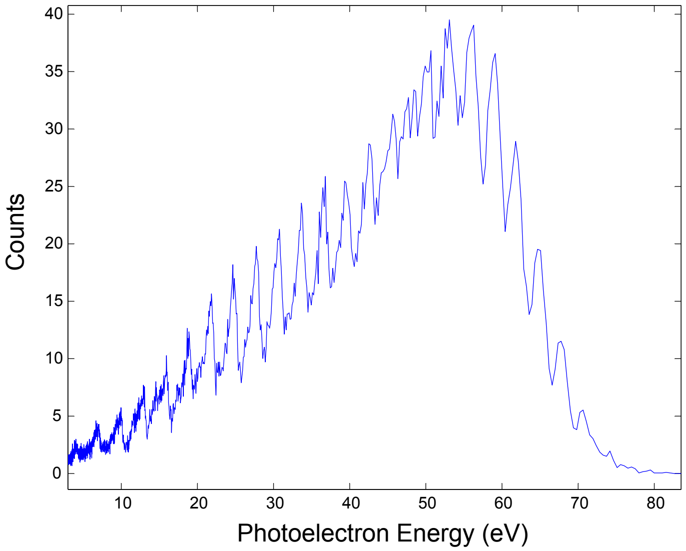

Figure 6.9: Photoelectron spectrum of HHG from Ne extending to ∼ 100 eV photon energies.

With harmonic photon energies up to 100 eV, it is possible to look at inner-shell ionization processes in xenon. The inner 4d-shell of xenon has two energy levels with ionization potentials of 67.5 and 69.5 eV. When the inner shell is ionized, Auger processes, where the excited ion rearranges to a lower energy state by ejecting a second electron, are observed. A diagram of the Auger process in xenon is shown in Figure 6.11. It is also possible to observe Auger electrons

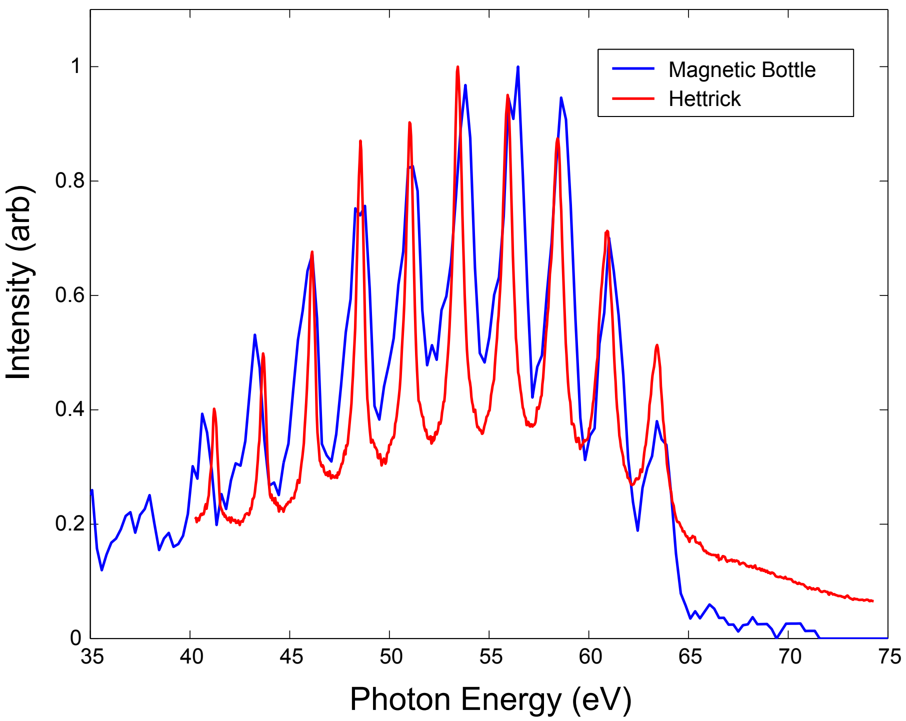

Figure 6.10: Comparison of photon spectra measured using the magnetic bottle photoelectron spectrometer and the Hettrick spectrometer.

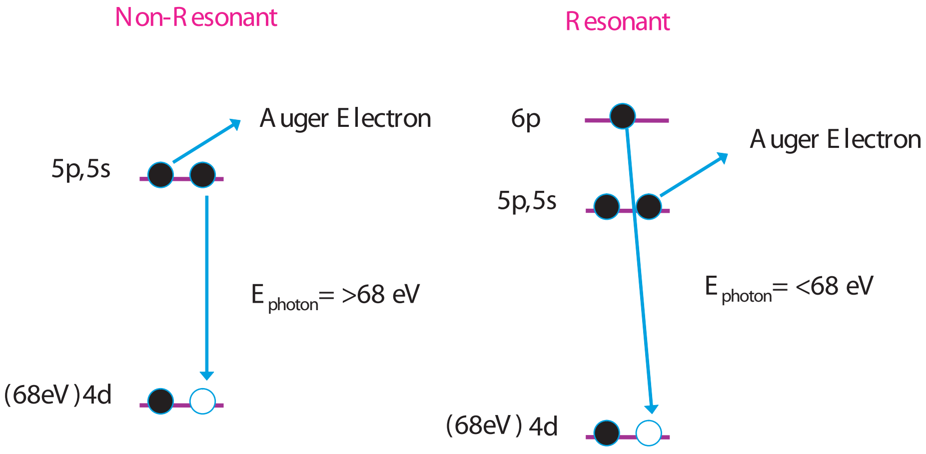

Figure 6.11: Diagram of resonant and non-resonant Auger processes in xenon.

using photon energies lower than 67.5 eV through a resonant Auger process where the xenon atom is first excited to a Rydberg state and then undergoes Auger decay. The lifetime of these processes is very short. Experimentally, Auger processes in atoms are measured by the energy bandwidth, since lifetime broadening is the only broadening mechanism. Auger decay in Xe has been measured to be ~ 8 fs (extremely fast!).[38] Using a cross-correlation technique described in the next section, it is possible to experimentally measure this process in the time domain, and was done in the case of krypton in reference [24]. While this is not interesting in the case of atoms, it may be a useful tool for measuring Auger lifetimes in molecules.

Figure 6.12 shows the experimental photoelectron spectrum from ionization of xenon clearly showing the Auger electrons. When an Al filter is used to block all the harmonics with photon energies above 65 eV, most of the Auger electrons disappear. Even with the Al filter, some Auger electrons are produced from resonant Auger processes. Since the photoelectron spectrum of xenon was taken while ionizing with a broad spectrum of harmonics, the Auger electron peak overlaps with electrons produced from direct ionization of the valence and inner shells. However, from the absorption spectrum of xenon, Figure 6.13, it is apparent that certain photon energies are preferentially absorbed so that the photoelectron spectrum does have recognizable features attributed to different ionization processes. The harmonic structure is not well resolved since xenon has multiple energy levels in its valence and inner shells. In the case of the valence shell, the energy levels are separated by 1.3 eV while the inner shell levels are separated by 2 eV. Each harmonic peak creates two photoelectron peaks for both ionization processes, adding additional structure to the spectrum.

To achieve a background free spectrum of the Auger electrons, a narrow-bandwidth soft x-ray multilayer mirror was used. The multilayer was made by Yanwei Liu at Berkeley. The reflectivity of the mirror is given in Figure 6.14. The mirror has a radius of curvature of 50 cm. It was placed 25 cm after the detection region, and the reflected light was focused back onto the detector. The detector was slightly offset so that the EUV light before the mirror passes to the side of the detection region and does not generate any signal. The time zero of the reflected beam

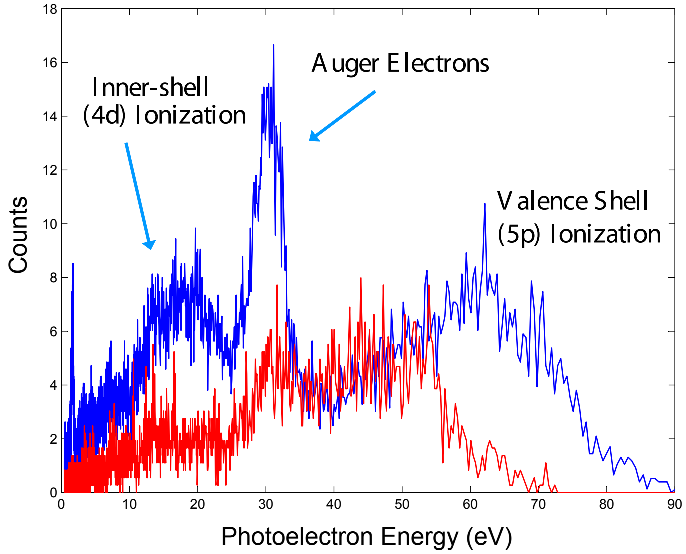

Figure 6.12: Photoelectron spectrum of xenon using all harmonics (blue) and harmonics passing through an Al filter blocking energies > 65 eV (red).

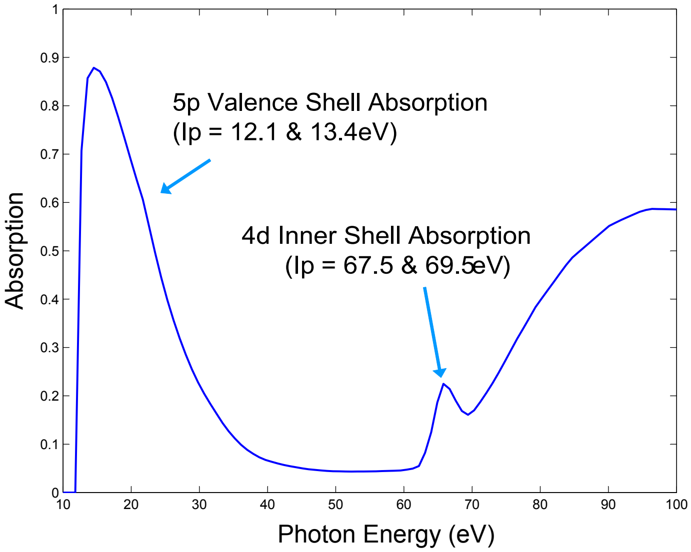

Figure 6.13: Absorption of xenon gas as a function of photon energy. Data from the Center for X-ray Optics, Berkeley Lab (www-cxro.lbl.gov).

is delayed by an additional 1.67 ns (50 cm/c). Figure 6.15 shows the harmonic spectrum before and after the multilayer mirror using He gas to generate harmonics and Ne as the detection gas. The peak photon energy is a bit lower than the measurement done in Figure 6.14 because the incident angle is closer to 89 degrees. The mirror does a good job of selecting out harmonics in a narrow bandwidth around 90 eV. Using this selection of harmonic energies, the photoelectron spectrum of xenon was measured; see Fig. 6.16. In this spectrum, the photoelectrons generated by ionization of the valence shell, inner shell, and from Auger processes do not overlap and can be isolated. This makes it possible to do measurements of the lifetime of Auger decay in Xe using cross-correlation techniques which will be discussed in the next section.

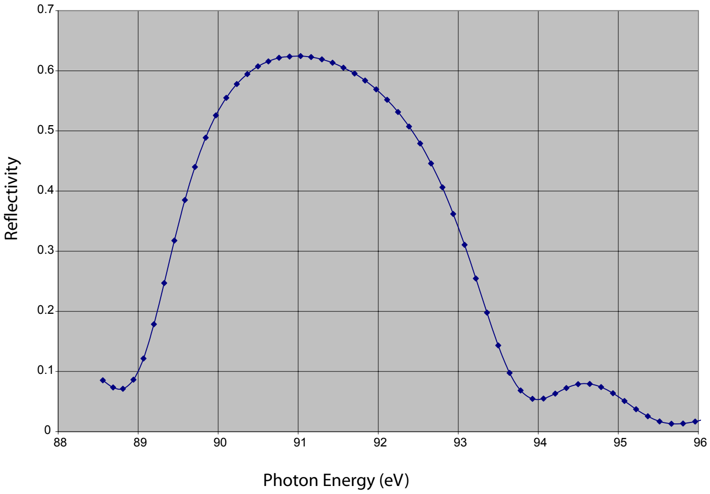

Figure 6.14: Reflectivity as a function of photon energy for the Si/Mo multilayer mirror, measured at an 85 degree incident angle.

6.3 Cross-correlation Measurements

Recently, there has be a great deal of interest in using the light from high harmonic generation for very short time measurements. High harmonic generation is emitted in a series of attosecond bursts every half cycle of the driving field. Using HHG and an IR probe pulse, it is possible to make cross correlation measurements of the HHG emission itself,[34, 57] or of

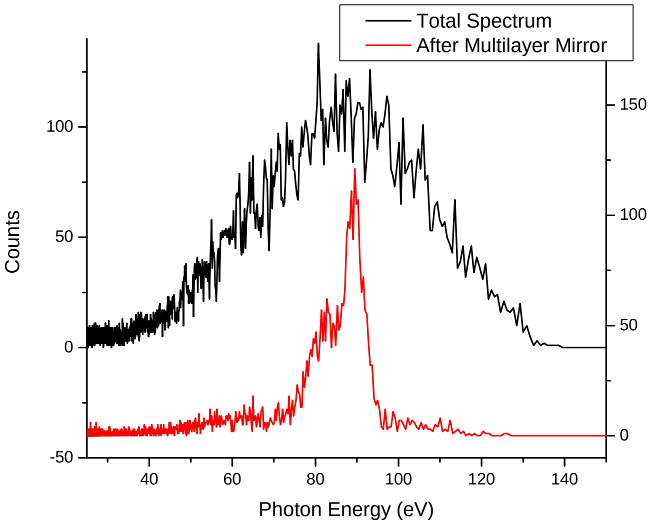

Figure 6.15: Spectra of high harmonics generated using He gas and detected with Ne gas before (black) and after (red) the narrow-band multilayer mirror.

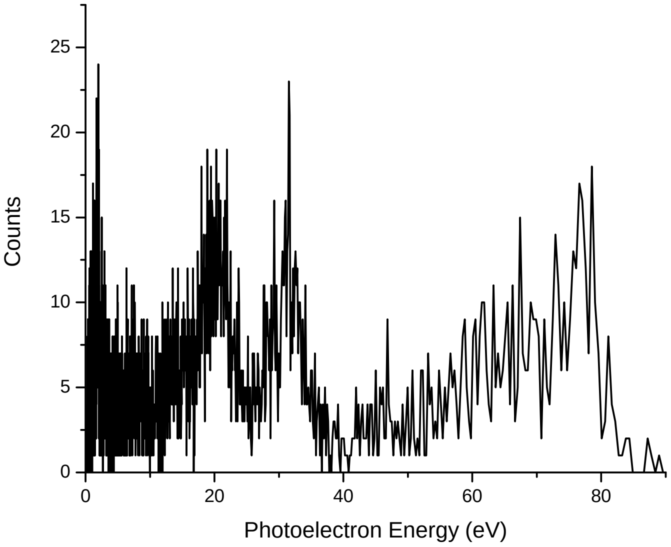

Figure 6.16: Photoelectron spectrum of Xe using a narrow bandwidth of harmonics selected by the multilayer mirror.

fast electronic processes[24]. All of these cross correlation measurements are based on what is sometimes termed laser-assisted ionization, whereby the momenta of photoelectrons or Auger electrons emitted from an ionization process are modified in the presence of a weak non-resonant field. Experimental measurements using this technique were first done by Schins et al. and Glover et al. in 1996.[64, 32] In laser assisted ionization, ionization of an atom by an EUV photon is accompanied by the absorption or emission of IR photons, giving sideband peaks to the photoelectron spectrum. If a weak probe field is used, the intensity of the first sideband is proportional to the intensity of the EUV pump pulse and the intensity of the IR probe pulse according to lowest order perturbation theory. The sideband intensity as a function of probe delay gives the intensity cross-correlation of the two pulses.[64]

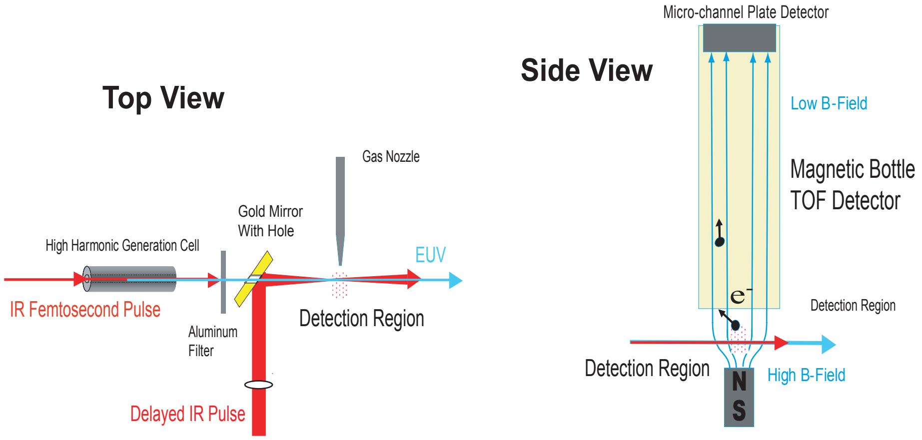

Figure 6.17: Schematic of experimental setup for measuring the pulse duration of high harmonic generation.

For the measurement, 10% of the 800 nm light is split off from that used to drive high harmonic generation. This probe light is delayed and then recombined co-linearly with the high harmonic beam in the interaction region. The experimental setup is shown in figure 6.17. When both the EUV and IR probe pulses are present, the resulting photoelectron spectrum contains sidebands as a result of laser-assisted ionization. These sidebands have energies equal to a

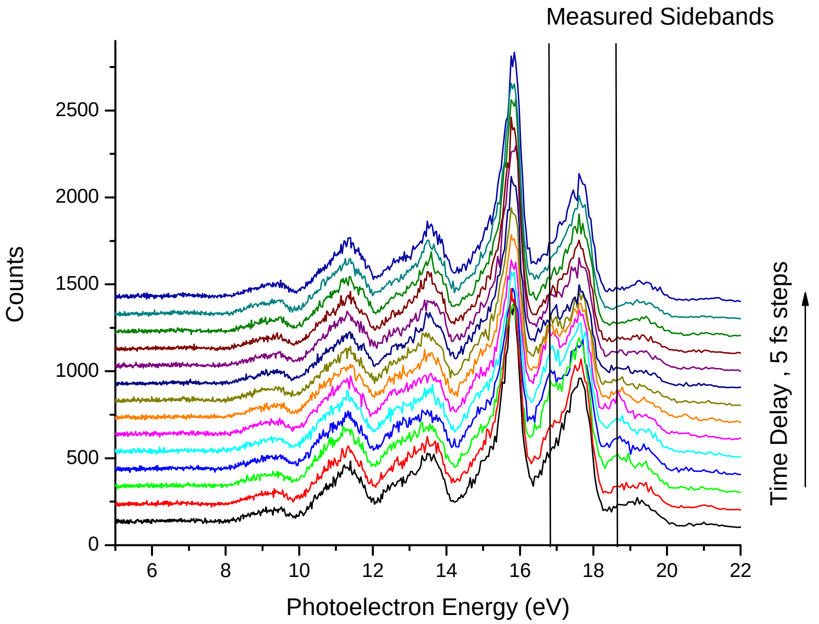

Figure 6.18: Photoelectron spectra at different probe delays. The sidebands that are analyzed are indicated.

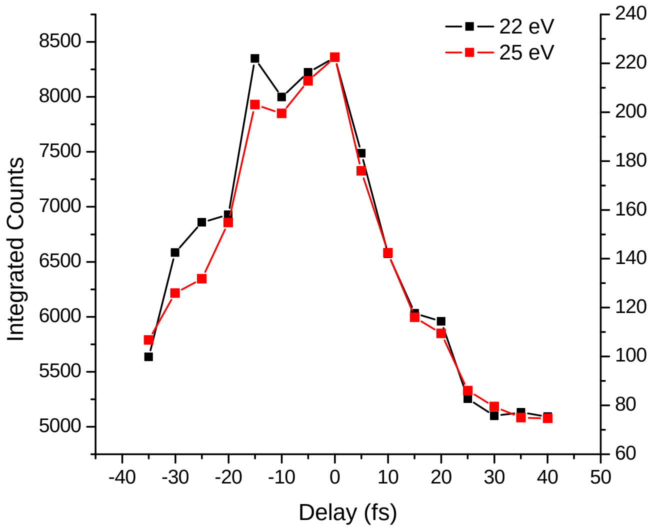

Figure 6.19: Integrated counts for the sidebands at 22 and 25 eV as a function of probe delay.

harmonic plus or minus one photon of the fundamental (800 nm). The cross-correlation signal is obtained by integrating the counts in the sidebands as a function of probe delay. Figure 6.18 shows photoelectron spectra as a function of probe time delay. The harmonics are generated in Ar gas and detected with Ne. Figure 6.19 shows the integrated counts for two of the sidebands as a function of probe delay. The cross correlation signal is 28 fs (+/- 2 fs) FWHM when fit to a Gaussian. This measurement is consistent with the duration of the probe pulse indicating that the HHG emission is significantly shorter than the fundamental pulse. One of the major difficulties of this technique is that the exact intensity profile of the probe pulse must be known to measure the high harmonic emission. Recently, it has been demonstrated that the carrier oscillations of the probe pulse can be used for time measurement, giving a much improved temporal resolution and making it possible to measure a single attosecond pulse.[34]

Chapter 7

Conclusion

In conclusion, this work applies nonlinear optical techniques to significantly higher photon energies than before, enhancing the conversion efficiency and opening up the possibility of generating multi-keV photon energies from high harmonic generation. The ideas in this work have the potential to greatly increase the number of applications possible using HHG in many areas of chemistry and biology by making it a practical, efficient, table-top light source. The enhancements demonstrated in this work are still far from the theoretical limits. Future work on quasi-phase matching over longer fiber lengths and using shorter modulations should improve the photon flux from HHG even further. Quasi-phase matching techniques may also provide a means of generating an enhanced attosecond duration pulse of high harmonic light. Currently, high harmonic generation is the only method for generating light pulses of durations in the attosecond regime (1 attosecond = 10^{-18} seconds). Already, initial experiments have been performed using light from HHG to measure electronic processes on attosecond time scales. Therefore, the advances demonstrated in this work have the potential to influence both technology and fundamental science.

Bibliography

[1] G. P. Agrawal. Nonlinear Fiber Optics. Academic Press, San Diego, 3rd edition, 2001.

[2] C. Altucci, T. Starczwski, E. Mevel, C. Wahlstrom, B. Carre, and A. L'Huillier. Journal of the Optical Society of America B, 13:148, 1996.

[3] M.V. Ammosov, N.B. Delone, and V.P. Krainov. Tunnel ionization of complex atoms and of atomic ions in an alternating electromagnetic field. Soviet Physics JETP, 64(6):1191, 1986.

[4] J.A. Armstrong, N. Bloembergen, J. Ducuing, and P.S. Pershan. Interactions between light waves in a nonlinear dielectric. Physical Review A, 127:1918, 1962.

[5] S. Augst, D.D. Meyerhofer, D. Strickland, and S.L. Chin. Laser ionization of noble gases by coulomb-barrier suppression. JOSA B, 8(4):858–867, 1991.

[6] S. Augst, D. Strickland, D.D. Meyerhofer, S.L. Chin, and J.H. Eberly. Tunneling ionization of noble gases in a high-intensity laser field. Physical Review Letters, 63(20):2212–2215, 1989.

[7] S. Backus, R. Bartels, S. Thompson, R. Dollinger, H. C. Kapteyn, and M. M. Murnane. High-efficiency, single-stage 7-khz high-average-power ultrafast laser system. Optics Letters, 26(7):465–467, 2001.

[8] S. Backus, C. Durfee, M.M. Murnane, and H.C. Kapteyn. High power ultrafast lasers. Review of Scientific Instruments, 69(3):1207–1223, 1998.

[9] P. Balcou, P. Salieres, A. L'Huillier, and M. Lewenstein. Generalized phase-matching conditions for high harmonics: The role of field-gradient forces. Physical Review A, 55(4):3204–3210, 1997.

[10] R. A. Bartels, A. Paul, H. Green, H. C. Kapteyn, M. M. Murnane, S. Backus, I. P. Christov, Y. W. Liu, D. Attwood, and C. Jacobsen. Generation of spatially coherent light at extreme ultraviolet wavelengths. Science, 297(5580):376–378, 2002.

[11] M. Bauer, C. Lei, K. Read, R. Tobey, J. Gland, M. M. Murnane, and H. C. Kapteyn. Direct observation of surface chemistry using ultrafast soft-x- ray pulses. Physical Review Letters, 87(2):025501, 2001.

[12] J. D. Bierlein, D. B. Laubacher, J. B. Brown, and C. J. van der Poel. Balanced phase matching in segmented ktiopo$_4$ waveguides. Applied Physics Letters, 56(18):1725–1727, 1990.

[13] R. W. Boyd. Nonlinear Optics. Academic Press, San Diego, 2nd edition, 2003.

[14] T. Brabec and F. Krausz. Intense few-cycle laser fields: Frontiers of nonlinear optics. Reviews of Modern Physics, 72(2):545–591, 2000.

[15] Z. H. Chang, A. Rundquist, H. W. Wang, M. M. Murnane, and H. C. Kapteyn. Generation of coherent soft x-rays at 2.7 nm using high harmonics. Physical Review Letters, 79(16):2967–2970, 1997.

[16] Z. H. Chang, A. Rundquist, H. W. Wang, M. M. Murnane, and H. C. Kapteyn. Temporal phase control of soft-x-ray harmonic emission. Physical Review A, 58(1):R30–R33, 1998.

[17] E.A. Chowdhury, C.P.J. Barty, and B.C. Walker. Nonrelativistic ionization of the l-shell states in argon by a relativistic 10^{19} w/cm^{-2} laser field. Physical Review A, 63:042712, 2001.

[18] I. P. Christov. Control of high harmonic and attosecond pulse generation in aperiodic modulated waveguides. Journal of the Optical Society of America B, 18(12):1877–1881, 2001.

[19] I. P. Christov, H. C. Kapteyn, and M. M. Murnane. Quasi-phase matching of high-harmonics and attosecond pulses in modulated waveguides. Optics Express, 7(11):362–367, 2000.

[20] I.P. Christov, M.M. Murnane, and H.C. Kapteyn. Generation and propagation of attosecond x-ray pulses in gaseous media. Physical Review A, 57(4):R2285, 1998.

[21] E. Constant, D. Garzella, P. Breger, E. Mevel, C. Dorrer, C. Le Blanc, F. Salin, and P. Agostini. Optimizing high harmonic generation in absorbing gases: Model and experiment. Physical Review Letters, 82(8):1668–1671, 1999.

[22] P. B. Corkum. Plasma perspective on strong field multiphoton ionization. Physical Review Letters, 71(13):1994–1997, 1993.

[23] D. Descamps, C. Lynga, J. Norin, A. L'Huillier, C. G. Wahlstrom, J. F. Hergott, H. Merdji, P. Salieres, M. Bellini, and T. W. Hansch. Extreme ultraviolet interferometry measurements with high-order harmonics. Optics Letters, 25(2):135–137, 2000.

[24] M. Drescher, M. Hentschel, R. Kienberger, M. Uiberacker, V. Yakovlev, A. Scrinizi, T. Westerwalbesloh, U. Kleineberg, U. Heinzmann, and F. Krausz. Time-resolved atomic inner-shell spectroscopy. Nature, 419(6909):803–807, 2002.

[25] C. G. Durfee, A. Rundquist, S. Backus, Z. Chang, C. Herne, H. C. Kapteyn, and M. M. Murnane. Guided-wave phase-matching of ultrashort-pulse light. Journal of Nonlinear Optical Physics & Materials, 8(2):211–234, 1999.

[26] C. G. Durfee, A. R. Rundquist, S. Backus, C. Herne, M. M. Murnane, and H. C. Kapteyn. Phase matching of high-order harmonics in hollow waveguides. Physical Review Letters, 83(11):2187–2190, 1999.

[27] M. M. Fejer, G. A. Magel, D. H. Jundt, and R. L. Byer. Quasi-phase-matched 2nd harmonic-generation - tuning and tolerances. IEEE Journal of Quantum Electronics, 28(11):2631–2654, 1992.

[28] M. Ferray, A. L'Huillier, X. F. Li, L. A. Lompr, G. Mainfray, and C. Manus. Multiple-harmonic conversion of 1064 nm radiation in rare gasses. Journal of Physics B, 21:L31, 1987.

[29] M. B. Gaarde, F. Salin, Ph. Balcou, K. J. Schafer, K. C. Kulander, and A. L'Huillier. Spatiotemporal separation of high harmonic radiation into two quantum path components. Physical Review A, 59(2):1367–1373, 1999.

[30] E. A. Gibson, A. Paul, N. Wagner, R. Tobey, S. Backus, I. P. Christov, M. M. Murnane, and H. C. Kapteyn. High-order harmonic generation up to 250 ev from highly ionized argon. Physical Review Letters, 92(3):033001, 2004.

[31] E. A. Gibson, A. Paul, N. Wagner, R. Tobey, D. Gaudiosi, S. Backus, I. P. Christov, A. Aquila, E. M. Gullikson, D. T. Attwood, M. M. Murnane, and H. C. Kapteyn. Coherent soft x-ray generation in the water window with quasi-phase matching. Science, 302(5642):95–98, 2003.

[32] T. E. Glover, R. W. Schoenlein, A. H. Chin, and C. V. Shank. Observation of laser assisted photoelectric effect and femtosecond high order harmonic radiation. Physical Review Letters, 76(14):2468–2471, 1996.

[33] R. Haight and D. R. Peale. Tunable photoemission with harmonics from subpicosecond lasers. Review of Scientific Instruments, 65(6):1853–1857, 1994.

[34] M. Hentschel, R. Kienberger, Ch. Spielmann, G. A. Reider, N. Milosevic, T. Brabec, P. Corkum, U. Heinzmann, M. Drescher, and F. Krausz. Attosecond metrology. Nature, 414(6863):509–513, 2001.

[35] Michael C. Hettrick. In-focus monochromator: Theory and experiment of a new grazing incidence mounting. Applied Optics, 29:4531–4535, 1990.

[36] John David Jackson. Classical Electrodynamics, 3^{rd} Edition. John Wiley & Sons, Inc., New York, 1999.

[37] J. Javanainen, J.H. Eberly, and Q. Su. Numerical simulations of multiphoton ionization and above-threshold electron spectra. Physical Review A, 38:3430, 1988.

[38] M. Jurvansuu, A. Kivimaki, and S. Aksela. Inherent lifetime widths of ar $2p^{-1}$, kr $3d^{-1}$, xe $3d^{-1}$, and xe $4d^{-1}$ states. Physical Review A, 64:012502–7, 2001.

[39] H. C. Kapteyn, L. B. D. Silva, and R. W. Falcone. Short-wavelength lasers. Proceedings of the IEEE, 80(3):342, 1992.

[40] R. Kienberger, E. Goulielmakis, M. Uiberacker, A. Baltuska, V. Yakovlev, F. Bammer, A. Scrinzi, T. Westerwalbesloh, U. Kleineberg, U. Heinzmann, M. Drescher, and F. Krausz. Atomic transient recorder. Nature, 427(6977):817–821, 2004.

[41] V.P. Krainov. Ionization rates and energy and angular distributions at the barrier-suppression ionization of complex atoms and atomic ions. Journal of the Optical Society of America B, 14(2):425, 1997.

[42] J. L. Krause, K. J. Schafer, and K. C. Kulander. High-order harmonic generation from atoms and ions in the high intensity regime. Physical Review Letters, 68(24):3535, 1992.

[43] P. Kruit and F. H. Read. Magnetic field paralleliser for 2π electron-spectrometer and electron-image magnifier. Journal of Physics E - Scientific Instruments, 16(4):313–324, 1983.

[44] K. C. Kulander, K. J. Schafer, and J. L. Krause. Dynamics of short-pulse excitation, ionization and harmonic conversion. In Super-intense laser-atom physics, 316, pages 95–110. NATO Advanced Science Institutes, 1993.

[45] L. D. Landau, E. M. Lifshitz, and L. P. Pitaevskii. Electrodynamics of Continuous Media, 2^{nd} Edition. Reed Educational and Professional Publishing Ltd, Oxford, 1984.

[46] M. Lewenstein, Ph. Balcou, M. Y. Ivanov, and P.B. Corkum. Theory of high-harmonic generation of low-frequency laser fields. Physical Review A, 49(3):2117–2132, 1993.

[47] M. Lewenstein, P. Salieres, and A. L'Huillier. Phase of the atomic polarization in high-order harmonic generation. Physical Review A, 52(6):4747–4754, 1995.

[48] A. L'Huillier, M. Lewenstein, P. Salieres, P. Balcou, M. Y. Ivanov, J. Larsson, and C. G. Wahlstrom. High-order harmonic-generation cutoff. Physical Review A, 48(5):R3433–R3436, 1993.

[49] A. R. Libertun, X. Zhang, A. Paul, E. Gagnon, T. Popmintchev, S. Backus, M. M. Murnane, H. C. Kapteyn, and I. P. Christov. Design of fully spatially coherent extreme-ultraviolet light sources. Applied Physics Letters, 84(19):3903–3905, 2004.

[50] E.A.J. Marcatili and R.A. Schmeltzer. Hollow metallic and dielectric waveguides for long distance optical transmission and lasers. Bell System Technical Journal, 43:1783, 1964.

[51] A. McPherson, G. Gibson, H. Jara, U. Johann, T. S. Luk, I. A. McIntyre, K. Boyer, and C. K. Rhodes. Studies of multiphoton production of vacuum-ultraviolet radiation in the rare gasses. Journal of the Optical Society of America B, 4:595–601, 1987.

[52] J. H. Moore, C. C. Davis, and M. A. Coplan. Building scientific apparatus : a practical guide to design and construction, 2nd edition. Addison-Wesley, Redwood City, CA, 1989.

[53] B. Nikolaus and D. Grishkowsky. 12x pulse compression using optical fibers. Applied Physics Letters, 42(1):1–2, 1983.

[54] M. Nisoli, S. De Silvestri, and O. Svelto. Generation of high energy 10 fs pulses by a new pulse compression technique. Applied Physics Letters, 68(20):2793–2795, 1996.

[55] L. Nugent-Glandorf, M. Scheer, D. A. Samuels, A. M. Mulhisen, E. R. Grant, X. M. Yang, V. M. Bierbaum, and S. R. Leone. Ultrafast time-resolved soft x-ray photoelectron spectroscopy of dissociating br-2. Physical Review Letters, 87(19):193002, 2001.

[56] A. Paul, R. A. Bartels, R. Tobey, H. Green, S. Weiman, I. P. Christov, M. M. Murnane, H. C. Kapteyn, and S. Backus. Quasi-phase-matched generation of coherent extreme-ultraviolet light. Nature, 421(6918):51–54, 2003.

[57] P. M. Paul, E. S. Toma, P. Breger, G. Mullot, F. Auge, Ph. Balcou, H. G. Muller, and P. Agostini. Observation of a train of attosecond pulses from high harmonic generation. Science, 292(5522):1689–1692, 2001.

[58] J. Peatross, M. V. Fedorov, and K. C. Kulander. Intensity-dependent phase-matching effects in harmonic generation. Journal of the Optical Society of America B, 12(5):863–870, 1995.

[59] S.C. Rae. Ionization-induced defocusing of intense laser pulses in high-pressure gases. Optics Communications, 97:25–28, 1993.

[60] J. J. Rocca, C. H. Moreno, M. C. Marconi, and K. Kanizay. Soft-x-ray laser interferometry of a plasma with a tabletop laser and a lloyd's mirror. Optics Letters, 24:420–422, 1999.

[61] A. Rundquist. Phase-matched generation of coherent, ultrafast x-rays using high harmonics. Ph.d., Washington State University, 1998.

[62] A. Rundquist, C.G. Durfee III, S. Backus, C. Herne, Z. Chang, M.M. Murnane, and H.C. Kapteyn. Phase-matched generation of coherent soft x-rays. Science, 280(5368):1412–1415, 1998.

[63] P. Salieres, T. Ditmire, M. Perry, A. L'Huillier, and M. Lewenstein. Angular distributions of high-order harmonics generated by a femtosecond laser. Journal of Physics B, 29(20):4771–4786, 1996.

[64] J. M. Schins, P. Breger, P. Agostini, R. C. Constantinescu, H. G. Muller, A. Bouhal, G. Grillon, A. Antonetti, and A. Mysyrowicz. Cross-correlation measurements of femtosecond extreme-ultraviolet high-order harmonics. Journal of the Optical Society of America B, 13(1):197–200, 1996.

[65] M. Schnrer, Z. Cheng, M. Hentschel, G. Tempea, P. Klmn, T. Brabec, and F. Krausz. Absorption-limited generation of coherent ultrashort soft-x-ray pulses. Physical Review Letters, 83(4):722–725, 1999.

[66] A. Scrinzi, M. Geissler, and T. Brabec. Ionization above the coulomb barrier. Physical Review Letters, 83(4):706–709, 1999.

[67] E. Seres, J. Seres, F. Krausz, and C. Spielmann. Generation of coherent soft-x-ray radiation extending far beyond the titanium l edge. Physical Review Letters, 92(16):163002, 2004.

[68] B. Shan and Z. H. Chang. Dramatic extension of the high-order harmonic cutoff by using a long-wavelength driving field. Physical Review A, 65(1):1804, 2002.

[69] P.L. Shkolnikov, A. Lago, and A.E. Kaplan. Optimal quasi-phase-matching for high-order harmonic generation in gases and plasmas. Physical Review A, 50(6):R4461, 1994.

[70] C. Spielmann, N. H. Burnett, S. Sartania, R. Koppitsch, M. Schnrer, C. Kan, M. Lenzner, P. Wobrauschek, and F. Krausz. Generation of coherent x-rays in the water window using 5-femtosecond laser pulses. Science, 278:661–664, 1997.

[71] C. Spielmann, N. H. Burnett, S. Sartania, R. Koppitsch, M. Schnrer, C. Kan, M. Lenzner, P. Wobrauschek, and F. Krausz. Near-kev coherent x-ray generation with sub-10-fs lasers. IEEE Journal of Selected Topics in Quantum Electronics, 4:249–265, 1998.

[72] G. Tempea and T. Brabec. Nonlinear source for the generation of high-energy few-cycle optical pulses. Optics Letters, 23(16):1286–1288, 1998.

[73] W. J. Tomlinson, R. H. Stolen, and C. V. Shank. Compression of optical pulses chirped by self-phase modulation in fibers. Journal of the Optical Society of America B, 1(2):139, 1984.

[74] R. Trebino. Frequency-resolved optical gating: the measurement of ultrashort laser pulses. Kluwer Academic, Boston, 2000.

[75] T. Tsuboi, E. Y. Xu, Y. K. Bae, and K. T. Gillen. Magnetic bottle electron spectrometer using permanent magnets. Review of Scientific Instruments, 59(8):1357–1362, 1988.

[76] J. H. Underwood and E. M. Gullikson. High-resolution, high-flux, user friendly vls beamline at the als for the 501300 ev energy region. Journal of Electron Spectroscopy and Related Phenomena, 92:265–272, 1998.

[77] S. L. Voronov, I. Kohl, J. B. Madsen, J. Simmons, N. Terry, J. Titensor, Q. Wang, and J. Peatross. Control of laser high-harmonic generation with counterpropagating light. Physical Review Letters, 8713(13):3902, 2001.

[78] N. L. Wagner, E. A. Gibson, T. Popmintchev, I. P. Christov, M. M. Murnane, and H. C. Kapteyn. Self-compression of ultrashort pulses through ionization-induced spatio-temporal reshaping. Physical Review Letters, to be published 2004.

[79] C.G. Wahlstrom, S. Borgstrom, J. Larsson, and S.G. Pettersson. High-order harmonic generation in laser-produced ions using a near-infrared laser. Physical Review A, 51:585, 1995.

[80] C.G. Wahlstrom, J. Larsson, A. Persson, T. Starczewski, S. Svanberg, P. Salires, Ph. Balcou, and A. L'Huillier. High-order harmonic generation in rare gases with an intense short-pulse laser. Phys. Rev. A, 48:4709–4720, 1993.

[81] B. Walker, B. Sheehy, L.F. DiMauro, P. Agostini, K.J. Schafer, and K.C. Kulander. Precision measurement of strong field double ionization of helium. Physical Review Letters, 73(9):1227–1230, 1994.

[82] K. Yamane, Z. Zhang, K. Oka, R. Morita, M. Yamashita, and A. Suguro. Optical pulse compression to 3.4fs in the monocycle region by feedback phase compensation. Optics Letters, 28(22):2258–2260, 2003.

[83] J. Zhou, J. Peatross, M.M. Murnane, H.C. Kapteyn, and I.P. Christov. Enhanced high harmonic generation using 25 femtosecond laser pulses. Physical Review Letters, 76(5):752–755, 1996.

Appendix A

ADK ionization rate calculation

The numerical calculations of the ionization rate use the expression in Ref. [71] for the Ammosov-Delone-Krainov (ADK) theory including the Keldysh theory after Coulomb correction. The tunnel ionization rate is given by

$$\omega(t) = \omega_p |C_{n*}|^2 (\frac{4\omega_p}{\omega_t})^{2n*-1} \exp(-\frac{4\omega_p}{3\omega_t}) \tag{A.1}$$

with

$$\begin{aligned}
\omega_p &= \frac{I_P}{\hbar} \\
\omega_t &= \frac{eE_l(t)}{(2mI_p)^{1/2}} \\
n* &= Z(\frac{I_{ph}}{I_p})^{1/2} \\
|C_{n*}|^2 &= 2^{2n*}[n * \Gamma(n * +1)\Gamma(n*)]^{-1}
\end{aligned}$$

where I_p is the ionization potential of the gas species, I_{ph} is the ionization potential of the hydrogen atom, $E_l(t)$ is the electric field of the laser, and m is the mass of the electron.

From this rate, it is straightforward to calculate the ionization fraction as a function of time during the laser pulse given by:

$$\eta(t) = 1 - \exp[-\int_{-\infty}^{t} dt' \omega(t')]. \tag{A.2}$$

Matlab Code

```
Eion = 0.58065; % Ionization Potential for Argon in a.u.
Eion2=27.6/27.21; % 2nd Ionization Potential for Argon in a.u.
%Eion = 21.5646/27.21; % Ionization Potential for Neon in a.u.
%Eion2=40.1/27.21; % 2nd Ionization Potential for Neon in a.u.

QN = 1./sqrt(2*Eion);
QN2 = 2./sqrt(2*Eion2);
Ain = 5.0E14; % Peak intensity in W/cm2
Ain = sqrt(Ain/3.51E16); % Electric field amplitude

Tpul = 30.; % Pulse FWHM in fs
Tpul = Tpul*1E-15*4.1322E16;
Tf = Tpul*0.84932;
wo = 0.05695;
TT = 2.*pi/wo;
Nx = 10000; % Number of time steps
HT = 4.*Tf/Nx;
for i=1:Nx
    T = i*HT;
    E(i)=Ain*exp(-(T-2.0*Tf)^2/Tf^2)*cos(wo*(T-2*Tf));
    Int(i)=(Ain*exp(-(T-2.0*Tf)^2/Tf^2))^2;
end

N(1)=1.;
N1(i)=0.;
N2(1)=0.;
T(1)=0.;
Rint=0.;
for i=1:Nx-1
    T(i+1) = i*HT;
    F = abs(E(i))+1.E-30;
    C2=2^(2*QN)/(QN*gamma(QN+1)*gamma(QN));
    C22=2^(2*QN2)/(QN2*gamma(QN2+1)*gamma(QN2));
    Rate1(i)=Eion*C2*(4.0*Eion*sqrt(2.0*Eion)/F)^(2.0*QN-1.0)*...
        exp(-4.0*Eion*sqrt(2.0*Eion)/(3.0*F));
    Rate2(i)=Eion2*C22*(4.0*Eion2*sqrt(2.0*Eion2)/F)^(2.0*QN2-1.0)*...
        exp(-4.0*Eion2*sqrt(2.0*Eion2)/(3.0*F));
    Rint=Rint+Rate1(i)*HT;
    N(i+1)=exp(-Rint);  % Number of Neutrals
    N1(i+1)=1.-N(i)-N2(i);  % Number of Single Ions
    N2(i+1)= N2(i)+Rate2(i)*N1(i)*HT;   % Number of Double Ions
    Rate1(i)=Rate1(i)*N(i);
    Rate2(i)=Rate2(i)*N1(i);
end

Neutral=1-N;
Ion1=N1;
Ion2=N2;
T=(T-2*Tf)/TT*2.67;  % Convert to fs
```

Appendix B

Magnetic Field Calculations

The calculation of the magnetic field of the magnetic-bottle spectrometer in Mathematica is given on the following pages.

■ Magnetic Field for Permanent Magnet with Magnetization, M, Using the Magnetic Scalar Potential

$$\mathtt{Phi1[r\_,\ \theta\_,\ z\_,\ r1\_,\ \theta1\_,\ b\_]} = \frac{M}{4*\pi}\left(\frac{1}{\sqrt{\mathtt{r1^\wedge 2+r^\wedge 2-2\,r\,r1\,Cos[\theta-\theta1]+(z)^\wedge 2}}}-\frac{1}{\sqrt{\mathtt{r1^\wedge 2+r^\wedge 2-2\,r\,r1\,Cos[\theta-\theta1]+(z+b)^\wedge 2}}}\right);$$

```
Phi2[r_, θ_, z_, r1_, b_] = Simplify[Integrate[Phi1[r, θ, z, r1, θ1, b], {θ1, 0, 2 Pi}]];

Phi[r_, θ_, z_, R_, b_] := NIntegrate[r1 * Phi2[r, θ, z, r1, b], {r1, 0, R}];

Δ = .0001 (*cm*);

HR[r_, θ_, z_, R_, b_] := -1 * (Phi[r + Δ / 2, θ, z, R, b] - Phi[r - Δ / 2, θ, z, R, b]) / Δ

HZ[r_, θ_, z_, R_, b_] := -1 * (Phi[r, θ, z + Δ / 2, R, b] - Phi[r, θ, z - Δ / 2, R, b]) / Δ

BR[r_, θ_, z_, R_, b_] := mu * HR[r, θ, z, R, b];

BZ[r_, θ_, z_, R_, b_] := mu * HZ[r, θ, z, R, b];

mu = 4 Pi * 10^-1 (*Gauss cm/Amp*);
b = 5.08 (*cm- 2 in thickness*);
R = 1.27 (*cm - 1 in diameter*);
M = 8000 (*magnetization*);
```

■ Magnetic field of a loop with current J and radius a at any pt. (r,z). (equations from Landau and Lifshitz)

```
BLoopR[r_, z_, z1_, a_, J_] = J * (mu / (2 Pi)) * ((z - z1) / r) / Sqrt[(a + r) ^2 + (z - z1) ^2] *
    (-EllipticK[ 4 a r / ((a + r) ^2 + (z - z1) ^2)] + (a^2 + r^2 + (z - z1) ^2) *
       EllipticE[ 4 a r / ((a + r) ^2 + (z - z1) ^2)] / ((a - r) ^2 + (z - z1) ^2)) ;

BLoopZ[r_, z_, z1_, a_, J_] =  J * (mu / (2 * Pi)) / Sqrt[(a + r) ^2 + (z - z1) ^2]
    (EllipticK[ 4 a r / ((a + r) ^2 + (z - z1) ^2)] + (a^2 - r^2 - (z - z1) ^2) *
       EllipticE[ 4 a r / ((a + r) ^2 + (z - z1) ^2)] / ((a - r) ^2 + (z - z1) ^2));

a = 2.05 (*radius of coil in cm*);
J = .9(*current in coil in Amps*);
x1 = 5 (*distance of solenoid from origin in cm*);
L = 30 (*length of solenoid in cm*);
x2 = L + x1;
mu = 4 Pi * 10^-1(*Gauss cm/Amp*);

BSolenoidZ[r_, z_, a_, J_] = Sum[BLoopZ[r, z, i / 9, a, J], {i, 18, 288}];

BSolenoidR[r_, z_, a_, J_] = Sum[BLoopR[r, z, i / 9, a, J], {i, 18, 288}];

BtotR[r_, z_] := BSolenoidR[r, z, a, J] + BR[r, 0, z, R, b];
```

```
BtotZ[r_, z_] := BSolenoidZ[r, z, a, J] + BZ[r, 0, z, R, b];
```

■ Calculation of the adiabatic parameter

```
Δ = .0001 (*cm*);
m = .511 10^6 (* mass of e in eV *);
En = 1 (* Energy of e in eV *);
c = 3 10^10 (*cm/s*);
v = Sqrt[2 En / m] * c;
me = 9.11 10^-31 (*kg*);
e = 1.6 10^-19 (*coul*);
K = 2 10^4 * Pi me v / e;
```

```
χ1[r_, z_] := -K * (BtotZ[r, z + Δ / 2] - BtotZ[r, z - Δ / 2]) / (Δ BtotZ[r, z]^2)
```

Appendix C

Micro-Channel Plate Detector

Electron detection for the magnetic bottle spectrometer was accomplished with a custom designed micro-channel plate detector. The detector consists of two plates biased at ~ 1 kV each. The plates are made up of many micron-size diameter channels. Any electron that impacts the front of the detector kicks off secondary electrons. These electrons are then accelerated towards the anode, while building up signal with each additional impact to the channel walls, allowing $\sim$ 60 times signal gain. The micro-channel plate detector was designed to be compact enough to fit on a NW40 flange. Figure $C.1$ shows the basic design. The two plates are separated by a stainless steel spacer. The front and outer part of the detector is grounded while the anode is held at a high voltage. Vespel is used as the insulator. The anode is connected to a feedthrough which supplies the high voltage and transmits the fast current signal from the micro-channel plates. Separation of the fast signal is accomplished with a Bias Tee (Picosecond Pulse Labs, Model 5531). The feedthrough was purchased from Ceramaseal, Inc. (model 1084-01-W), designed for 50 Ohm impedance. To prevent any signal reflection which could cause multiple counts for one electron, the detector was designed to have 50 Ohm impedance from the feedthrough to the anode. The impedance of a coaxial waveguide is given by the expression,

$$Z_0 = \frac{276}{\sqrt{\epsilon}} \ln \frac{b}{a} \tag{C.1}$$

where ϵ is the permittivity of the insulator between the conductors, a is the inner conductor radius, and b is the radius to the inner edge of the outer conductor. For Vespel, b/a=4.81 for 50

Ohm impedance.[52] Figure $C.2$ shows the detailed dimensions of all the parts of the detector.

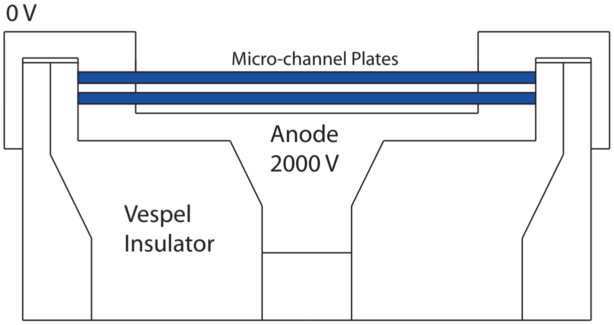

Figure C.1: MCP detector design. The micro-channel plates are in dark blue. The anode is biased at 2 kV and is insulated from the grounded stainless steel housing.

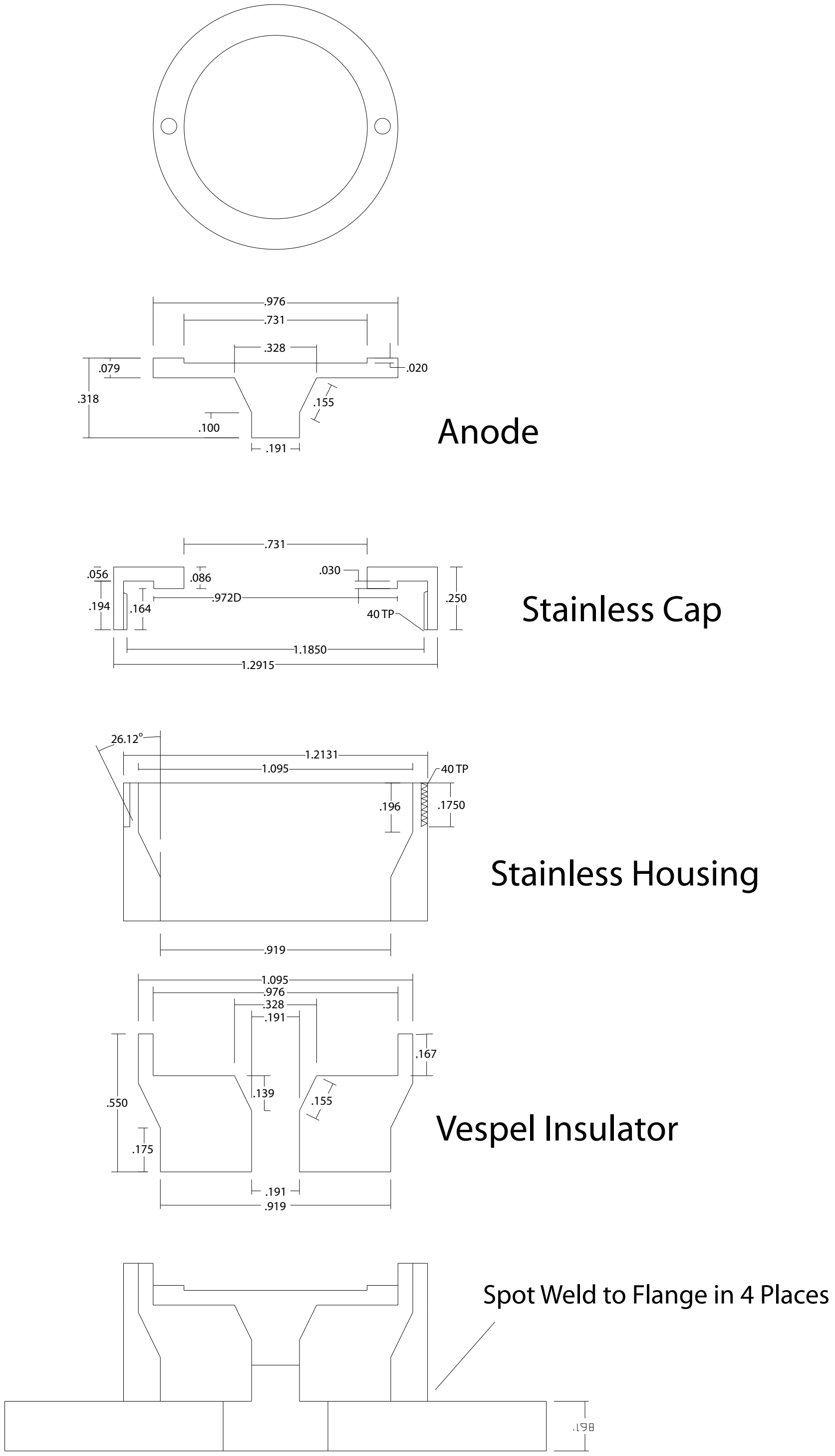

Figure C.2: Detailed schematic of the MCP detector giving dimensions for each part. All dimensions are in inches.